University of Zurich

Characterization of Novel VUV-Silicon Photomultipliers and their Application in Xenon-Based Dual-Phase TPCs

Master Thesis

Physics Institute

Author:
Chris Marentini

Supervisor:
Prof. Dr. Laura Baudis
Dr. Alexander Kish
M.Sc. Julien Wulf

March 16, 2018

Abstract

This master thesis is performed within the DARWIN project, which will be a next-generation direct dark matter experiment using a multi-ton xenon TPC. The DARWIN experiment will be the ultimate upgrade to the current XENON1T detector at the Gran Sasso National Laboratory (LNGS) in Italy. The main purpose in both experiments is the direct detection of weakly interacting massive particles (WIMP) via nuclear recoils in liquid noble gases. The interaction of a WIMP with the multi-ton liquid xenon target, will excite and ionize the target xenon atom and produce prompt scintillation light, while a delayed proportional scintillation light is produced due to the extraction of the ionization electrons into the gas-phase of the TPC. The XENON1T detector is currently using state of the art vacuum-based photomultiplier tube (PMTs) arrays to detect both scintillation light signals. Due to significant improvements in silicon-based photo-sensors in recent years, especially silicon photomultipliers (SiPM) are able to directly compete with vacuum-based PMTs and are considered as a potential replacement. This master thesis is therefore devoted to investigate the potential use of novel VUV-SiPMs for the planned DARWIN experiment.

In the first chapter of this thesis a brief introduction to the concept and modern detection mechanisms of Dark Matter are presented. Further, a short introductory chapter 2 on the physics of silicon photomultipliers follows. The essence of this thesis, presented in chapter 3, is firstly the full temperature-dependent characterisation of three novel SiPMs from Hamamatsu, which are sensitive in the vacuum-ultraviolet range of the electromagnetic spectrum. In a first characterisation run in gaseous nitrogen, one segment of the VUV3 12×12 mm^2 Hamamatsu-S13371 SiPM was tested, whereas in a second run two 3×3 mm^2 SiPM prototypes of the VUV4 generation were characterised in gaseous argon.
The second part of this thesis, presented in chapter 4, is dedicated to a newly designed SiPM top array for a potential implementation in the Xurich-II detector at the University of Zurich. The Xurich-II is a small xenon-based TPC constructed for sophisticated R&D purposes. The top array, containing four 12×12 mm^2 Hamamatsu-S13371 SiPMs, was incorporated in a GEANT4 framework for a light collection efficiency simulation.

Contents

CHAPTER 1

Introduction

This introductory chapter discusses briefly the concept of Dark Matter in section 1.1 and focuses in section 1.2 on the main astronomical observations that lead to the assumption of the existence of Dark Matter. While section 1.3 gives a short introduction of modern detection mechanisms, section 1.4.3 is fully dedicated on the Dark Matter detection with a xenon-based dual-phase Time Projection Chamber (TPC). In the last section 1.4 a brief overview of the newly anticipated DARWIN experiment is covered.

1.1 Dark Matter

Several astronomical observations of galaxy clusters, galactic rotation curves, bullet cluster or gravitational lensing to date lead to the astonishing assumption that most of the mass in the universe is not visible. The question of the origin of this invisible matter - also called Dark Matter - is one of the biggest problems of modern physics and is an essential part of the fields of cosmology and particle physics. Further evidence supported from nucleosynthesis and the cosmic microwave background (CMB), suggest that dark matter consists of non-baryonic particles [1]. Since dark matter forms large-scale structures in the universe, it had to be non-relativistic ("cold") at the time of decoupling.

Unlike normal matter, dark matter does not interact via the electromagnet force and thus does not absorb, reflect or emit any light and is only revealed by its gravitational interaction. This makes it an extremely difficult task to observe it with conventional scientific detection methods. The cross section of dark matter interaction with ordinary matter is very small. The Standard Model (SM) of particle physics in its current formulation is not able to explain the dark matter observed in our universe. Thus a hypothetical stable dark matter candidate at the weak scale - also called weakly interacting massive paricles (WIMPs) - is postulated. This weakly interacting massive particles (WIMPs) are subject of many Beyond the Standard Model (BSM) theories. The most promising theory is a supersymmetric extension of the standard model, which predicts a new dark matter particle candidate, which coincides with the properties of the hypothetical WIMP dark matter particle. This coincidence is also known as the WIMP-miracle. The most promising WIMP candidate is the neutralino, which emerges in the framework of supersymetric (SUSY) theories. The detection of a weakly interacting massive particle is therefore the main focus in experimental particle physics.

1.2 Observational Evidence of Dark Matter

Coma Cluster: The first claim about the existence of dark matter (DM) is dated back to 1933, when a Swiss astrophysics named Fritz Zwicky was studying the Coma cluster [2, 3]. Clusters of galaxies are one of the biggest bound structures in the universe and may contain hundreds up to many thousands of individual galaxies. All the individual galaxies are bound together in a compact region of space by its gravitational pull. Since galaxies are rotating with such high speed, the gravity generated by the observable mass of the objects they contain, should have torn themselves apart long time ago. This additional mass called „dark matter“ is assumed to be an extended and diffuse halo surrounding galaxies and thus generating the extra gravity for galaxies to stay intact. In clusters the gravitational mass can be derived by measuring the orbital motion of each constituent galaxy. By applying the cosmic viral theorem, which relates the observed velocity dispersion v^2 to the observed radius R of the cluster, Zwicky was able to measure the gravitation mass within the cluster. The viral theorem is given by

$$\frac{M_{\text{tot}} \cdot v^2}{2} = \frac{G \cdot M_{\text{tot}}^2}{4 \cdot R_{\text{tot}}} \quad , \tag{1.1}$$

where M_{tot} is the total mass of a system, v the dispersion velocity, R_{tot} the radius of the system and G the gravitational constant. By comparing the measured gravitational mass with the amount of luminous matter, which is indicated by the luminosity of the galaxies, a deficit of luminous matter was observed. This observation indicates the presence of large quantities ($>$90%) of invisible mass, which is only revealed by its gravitational interaction.

Galactic Rotation Curves: A further evidence of the dark matter provide the flat galactic rotation curves of spiral galaxies [4] such as our own Milky Way or the NGC6503 spiral galaxy shown in Figure (1.1). The visible stars and gas making up our galaxy extend out to a distance of about $\approx 10\,\text{kpc}$. Since our solar system is located approximately $\approx 8.5\,\text{kpc}$ from the center of the galaxy, one can state that we are situated rather at the outer bound of our own galaxy. By determining the rotational curve, the rotational velocity $v_c(r)$ of stars and gas as a function of the galactic center radius r, one can infer to the total mass $M_<(r)$ of the galaxy within the radius r. According to the Keplerian relation

$$v_c(r)^2 = \frac{\text{GM}_{\text{obs}}}{r} \quad , \tag{1.2}$$

one would expect the rotation curves at radii larger than the extent of the stellar disk ($\approx 10\,\text{kpc}$) to decline, but instead a constant velocity v_c is observed. Thus a flat rotation curve is observed, which implies a different proportionality of the enclosed mass $M_>(r) \propto r$ for $r >> 10\,\text{kpc}$. Thus the galaxy must contain far more matter than contributed by stars and gas. In particular there should be more mass beyond the apparent edge of the spiral galaxy, which means that dark matter is far more extended than the luminous matter [5].

Gravitational Lensing: An additional evidence of dark matter on this large scale comes from gravitational lensing [7]. Nearby galaxy clusters act as a lens for light originating from more distant galaxies with a high surface brightness. According to Einsteins general relativity massive objects influence the curvature of space-time and thus light emitted from a distant source is bended by the gravitational field of these massive objects. Hence, the light of a far distant galaxy will bend by the gravitational field of a nearby galaxy cluster, which results in multiple images of the background galaxy. Measuring the light deflection angle caused by the presence

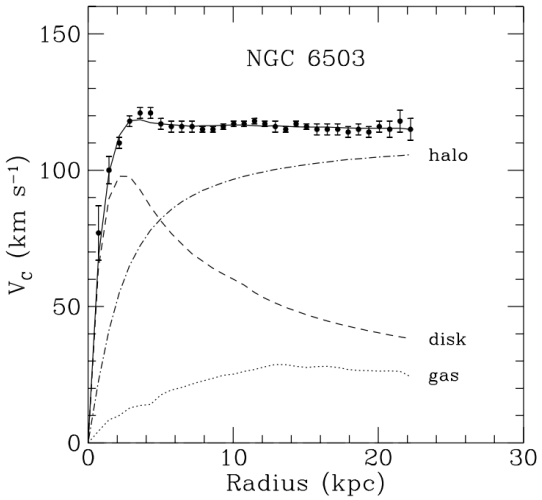

Figure 1.1: Galactic rotation curve of NGC6503 spiral galaxy. The graph shows the rotation velocity v_c as a function of the galocentric radius r. The theoretical contribution from luminous matter (disk line) and gas don't agree with the measured data points. The dashed-dotted line shows the dark matter halo contribution. The sum of all three contributions fit the data, showing that the galaxy is not only made out of visible matter. Taken from [6].

of nearby galaxy clusters, one can determine its mass. Comparing the measured mass of the galaxy cluster by the gravitational lensing effect with the calculated luminous mass, shows a discrepancy. The mass-to-light ratio measured with this method is consistent with the velocity dispersion measurements. Figure(1.2 - left) shows the massive galaxy clusters - Abell 1689 - taken by the NASA Hubble Space Telescope Advanced Camera for Surveys, which shows the effect of gravitational lensing [8].

Galaxy Clusters: A further unambiguous evidence of the existence of dark matter comes from the observation of galaxy cluster collisions. The Bullet Cluster seen in figure 1.2 is a good example for such a collision. While dark and visible matter usually overlap in specific regions of a cluster, it has been shown that during a cluster collision the two components separate. X-Ray observations of the Bullet Cluster show that most part of the luminous matter is concentrated in the center of the collision. Due to the electromagnetic interaction between baryonic matter, the colliding gas clouds heat up and slow down during the expansion, creating an intracluster plasma. The method of gravitation lensing on the other hand shows that most of the gravitational mass is observed on the outer region of the merging clusters. The baryonic mass distribution and the mass distribution provided by the gravitational lensing show therefore a spacial offset. Thus, stars and dark matter from both clusters pass through each other with negligible resistance [5, 9].

Figure 1.2: (left) Image of the massive galaxy clusters Abell 1689 taken by the NASA Hubble Space Telescope. The yellow-white objects are relatively nearby galaxy clusters, which act as a gravitational lens for background galaxies located billions of light years farther away than the Abell 1689 clusters. The blue arcs represent the distorted images from background galaxies due to gravitational lensing. The amount of normal and dark matter and the relative alignment of the background galaxies determine the amount of light distortion. A perfectly aligned galaxy behind a cluster would be seen as an "Einstein ring". Numerous ring sections or arcs can be observed in the image corresponding to individual galaxies. (right) An image of the Bullet Cluster from the Chandra X-Ray Observatory. Regions coloured in red show the distribution of hot gas taken from X-ray measurements. The blue region on the contrary shows the mass distribution inferred from gravitational lensing. Taken from [10, 11].

1.3 Detection Mechanisms of Dark Matter

There are basically three different approaches of detecting dark matter particles - especially WIMPs - in order to gain new insights in their properties. The first method is based on **direct detection**, which exploits the interaction of a dark matter particles with a Standard Model (SM) particle. The dark matter particle scatters with an atomic nucleus in a detector, where the atomic nucleus recoils. The recoil energy of the nucleus is then measured. The second method is referred to **indirect detection**, because it exploits the self-interaction of dark matter particles. The third detection method is based on **particle accelerators**, where dark matter particles are thought to be produced by the interaction of two SM particles. These three different detection methods bring various advantages and disadvantages with them and are used by different collaborations in the search of dark matter.

1.3.1 Indirect Detection

The indirect detection method is based on the self-annihilation process or decay of dark matter particles in outer space. If the dark matter density in a specific region of space is considerably high, the probability increases for two dark matter particles to annihilate and produce detectable gamma-rays or other SM particles such as neutrinos, positrons or protons:

$$\chi + \bar{\chi} \rightarrow q\bar{q}, W^+W^-, Z^0Z^0, ... \rightarrow \bar{p}, \bar{D}, e^+, \gamma \& \nu' s \tag{1.3}$$

with antiprotons $\bar{p}$, antideuterium $\bar{D}$, positrons e^+, photons γ and neutrinos ν [12].

Specific the regions, where a high dark matter density is accumulated by inelastic collisions, are for instance galactic center (GC), the Milky Way halo, the inner core of a sun, dwarf galaxies as well as galaxy clusters. The annihilation of dark matter particles would provide several indirect signatures, which can be detected either by earth-bound or satellite-based detectors by looking for spectrum distortions in various detection channels. The following detection channels of the annihilation of two dark matter particles χ into SM particles are of particular interest:

γ **Channel:** WIMP annihilation can produce high energetic photons over the production of quarks and gauge bosons, which subsequently fragment and decay into secondary photons from the two-photon decay of neutral pions π_0 ($\pi_0 \to \gamma\gamma$).

$$\chi\bar{\chi} \to q\bar{q}, W^+W^-, ... \to \gamma + X \tag{1.4}$$

The annihilation of two dark matter particles over this channel would yield a continuous spectrum, whereas a direct annihilation $\chi + \bar{\chi} \to \gamma\gamma$ would manifest itself in a discrete signal signature. This signal is essentially impossible to be explained by other means than dark matter. The direct annihilation channel is referred as the golden channel and is subject for several satellite and earth-bound experiments. Photons in the energy range of $\sim 100\,\mathrm{MeV}$ and several 100 GeV are detected by pair conversion telescopes like the Fermi Large Area Telescope (Fermi-LAT)[13]. This telescope uses conversion foils to induce pair production ($\gamma \to e^- + e^+$). The path of the electron/positron pair are tracked and the deposited energy measured in a final calorimeter. Photons with energy above 100 GeV are detected by earth-bound Imaging Air Cherenkov Telescopes such as H.E.S.S. [14], MAGIC [15] or VERITAS [16]. The planned next-generation Cherenkov telescope CTA [17] will improve the sensitivity by a factor of 10 from previous experiments and is able to detect high energetic photons from 10GeV up to 40TeV [18]. Although satellite experiments feature a large field of view of a few sr (steradian), they are limited by their effective area of a few square meters. In comparison, earth-bound telescopes can cover several 10000 square meters [19].

Neutrino Channel: The neutrino channel is a promising approach to probe for WIMP annihilation signals from sources like galactic centers, dwarf galaxies and galaxy clusters. Since neutrinos are almost massless and thus have a weak interaction cross section with ordinary matter, they can be traced back to their sources. Due to their weak interaction cross section and the abundant neutrino background from interactions of cosmic rays with the atmosphere, neutrinos from WIMP annihilations are hard to detect and demand gigantic earth-bound detectors - such as IceCube [20] or ANTARES [21]. The neutrino channel is a promising channel, since neutrinos can trace the gravitational capture of dark matter in celestrial bodies such as our sun, which yields a very clean signature [19]. WIMPs are captured and accumulated in the interior of the sun by scattering and would produce high energetic neutrinos from WIMP annihilation. Since the main composition of the sun is hydrogen, the neutrino searches from the sun are very sensitive to the spin-independent part of the WIMP-nucleon cross-section. This part is usually only accessible by direct detection methods [22, 23].

Charged Cosmic Ray Channel: The cosmic ray channel is an additional approach to search for remnants of dark matter annihilation. The resulting pairs of primary Standard model particles like $b\,\bar{b}$, $\mu^+\,\mu^-$, $\tau^+\,\tau^-$, $W^+\,W^-$ from the WIMP annihilation will decay and give higher fluxes of energetic cosmic rays containing e^-, e^+ and $\bar{p}$ through showering and hadronization [24]. The produced charged particles (e^-, e^+ and $\bar{p}$) from the Milky Way halo will propagate in the turbulent galactic magnetic fields, which makes it difficult to trace them back to the original

source. Experiments like PAMELA [25] look for an excess in the positron flux within the cosmic ray channel [26].

1.3.2 Direct Detection

For a typical WIMP mass m_χ of $100\,GeV/c^2$ the expected WIMP flux on earth is sufficiently large, such that a fraction may scatter off nuclei in an earth-bound detector. The WIMP flux ϕ_χ is in the the order of

$$\phi_\chi = \frac{\rho_\chi}{m_\chi} \cdot \langle v \rangle = 6.6 \times 10^4\,\mathrm{cm}^{-2}\mathrm{s}^{-1} \quad , \tag{1.5}$$

with the standard local WIMP density $\rho_\chi = 0.3\,\mathrm{GeVcm}^{-3}$ and the relative to the target mean WIMP velocity $\langle v \rangle \approx 220\,\mathrm{km\,s}^{-1}$ [27]. The numbers are highly model-dependent and are here only used to give a rough estimation. With the considered WIMP mass in the range of GeV-TeV, an electronic scattering of a WIMP is not expected, thus an interaction with an atomic nucleus is preferred. With the assumption of the interaction cross section of a WIMP in the order of $\sigma \approx 10^{-38}\,\mathrm{cm}^2$ on a nucleus with an atomic mass A = 100, one can calculate the expected interaction rate R:

$$R = \frac{N_A}{A} \cdot \phi_\chi \cdot \sigma = \frac{\rho_\chi}{m_\chi} \cdot \langle v \rangle \cdot \frac{1}{m_n} \cdot \frac{\sigma}{m_\chi} \sim 0.13 \text{ events kg}^{-1} \quad , \tag{1.6}$$

with N_A the number of target nuclei. The interaction cross section for WIMP scattering is very low, which results therefore in a considerably low interaction rate R. In order to detect a possible WIMP particle directly in an earth-bound detector, the detector needs to be build in such a way to maximize the potential interaction rate while minimizing the background contributions. These are specific requirements, which constrain the used detector material as well as the detection method. The detector material needs to contain target atoms with a high atomic mass to increase the interaction rate and feature a low natural radioactivity in order to minimize the intrinsic background contribution of the target material. Further, external background contribution from cosmic rays need to be minimized, which is the reason why earth-bound detectors are placed into underground facilities. Increasing the detector volume not only increases the desired interaction rate, but also allows self-shielding of the target material and reduces background contributions. Noble liquids like liquid argon and especially liquid xenon are excellent scintillation and ionization materials for dark matter direct detection detectors.

In general there are three different techniques of direct detection, which use different approaches to measure the recoil energy of a potential WIMP scattering: **ionization**, **scintillation** or **phonon** based experiments. Experiments like CRESST [28], EDELWEISS [29] or SuperCDMS [30] are based on the bolometric technique, which use crystal detectors to measure the recoil energy via temperature fluctuations within the crystal. Compared to other detection techniques, the bolometric one is not able to distinguish nuclear recoils from β/γ interactions. A further technique to detect dark matter particles is by exploiting the ionization of incident particles in a target material. Due to the low energy threshold and the energy resolution of germanium crystals, they are commonly used in current ionization detectors such as GERDA [31] or MAJORANA [32]. Although these experiments were originally constructed to search for neutrinoless double-beta decays ($0\nu\beta\beta$) their technology is a suitable tool for low-mass WIMP searches. A further approach is to measure the scintiallation light produced by scattering of a WIMP particle with a target nucleus. The XMASS [33] detector at the Kamioka Observatory of the Institute for Cosmic Ray Research at the University of Japan or the DEAP&CLEAN [34, 35] detectors are good examples of single-phase detectors, which focus on using only liquid noble gases as a scintillation material. The XMASS detector uses liquid xenon as a target material, whereas the DEAP/CLEAN detectors exploit the unique properties of liquid argon and neon as a scintillator. The target material are surrounded by photosensors in order to record the emitted scintillation light.
By combining different detection principles a better identification of the interaction type is possible and helps to suppress background contributions enormously. In example, experiments such as

EDELWEISS [29] or CDMS [36] not only measures the ionization in the germanium crystal, but also the phonons. With this approach they achieve an improved electronic recoil discrimination. On the contrary, argon-based dual-phase detectors such as ArDM [37], and xenon-based detectors such as LUX [38], PANDAX [39], XENON100 [40], XENON1T [41] or next-generation xenon-based detectors such as LZ [42] or XENONnT [43], use both the ionization and scintillation detection principles, which improves the the background discrimination with a high efficiency and allows an excellent event position reconstruction (x-y-z position) [44].

1.4 DARWIN - The Ultimate Dark Matter Detector

The DARWIN [45] experiment will be the ultimate successor of liquid xenon-based dual-phase TPCs and will be probing new accessible parameter space for WIMPs in a 50 t LXe target. The TPC will be able to probe particles with masses just above $5\,\mathrm{GeV}/c^2$ and aims to improve the sensitivity by a factor of 10 for spin-independent WIMP-nucleon interactions from previous WIMP search projects. Thus, the detector will be able to probe WIMP-nucleon cross sections of a few $\times 10^{-49}\mathrm{cm}^2$ for a WIMP mass of $\sim 50\,\mathrm{GeV}/c^2$. The DARWIN experiment is therefore designed to probe the entire parameter region for all WIMP masses, but is also limited by the ultimate neutrino background, which will start to dominate the recoil spectrum at low cross sections [46, 45].

1.4.1 Physical properties of Xenon

Liquid noble elements like liquid xenon or liquid argon, are widely used as liquid scintillation materials and are due their good scintillation and ionization properties successfully used in many detectors, especially in state of the art radiation detectors. Since liquid xenon has the highest scintillation and ionization yield of all noble elements (except radon, which is not yet studied so far for radiation detection), it is suitable for several astroparticle experiments such as double-beta decay, solar neutrino and WIMP dark matter detection. These kind of radiation detectors exploit the properties of liquid xenon successfully. The main properties of xenon are the following:

- **High density and atomic weight:** In comparison to organic materials, liquid xenon has a higher density($\rho \approx 3$ g/cm^3) and atomic weight (Z=54, $\bar{A}$=131.29), which makes it an efficient γ-radiation absorber. Due to a high atomic mass A, xenon has short radiation length of only a few centimeters. Thus incident gamma-rays only interact in the outer layer of the detector, shielding the inner volume from gamma contributions.
- **Response time** The fast response time of liquid xenon to radiation makes liquid xenon a suitable candidate for timing applications like in a time projection chamber (TPC).
- **Transparency** The liquid xenon is transparent to the scintillation light in the VUV region of the electromagnetic spectrum.
- **Isotopes:** Liquid xenon contains almost 50 % of non-zero spin isotopes such as ^{129}Xe and ^{131}Xe, which provide additional sensitivity to spin-dependent WIMP interactions [47].
- **Scintillation Wavelength λ:** The scintillation light of xenon is in the VUV region and its scintillation spectrum is peaked at $\lambda = 178\,\mathrm{nm}$ with a spectrum width of 14 nm [48].

When particles interact with a xenon atom they will loose energy and may be stopped or even scattered. Depending on the energy loss in the active xenon medium and type of the incident particle, different type of interactions will occur. Particles such as α particles, relativistic electrons, γ rays and neutrons interact differently with the xenon medium. By studying the different interaction mechanisms of the various incident particles with xenon, one can exploit these characteristic signals for particle identification and for further background studies for WIMP dark matter searches.

Charged Particles When a charged particle like an α or β particle interacts with a xenon atom, it will interact with the orbital electrons of the target atom via the Coulomb force. An orbital electron of a xenon atom can therefore either be lifted to an excited higher energy level shell, which leaves the previous xenon atom in an excited state, or can be completely removed from the atom - ionizing the xenon atom. Energetic alpha particles are able to encounter many xenon atoms while traversing through the xenon medium, therefore ionizing or exciting many xenon atom during the process. Since the energy loss of the alpha particle occurs in all directions simultaneously and the relative mass of an α particle to an orbital electron is large, the charged alpha particle is not affected by a single interaction, hence leaving its path within a straight line. This is different for relativistic electrons, since their mass is in the same order of magnitude. Relativistic electrons therefore experience a tortuous travel path through the active xenon medium. α- and $\beta-$ contributions from the radioactive decay (mainly from ^{238}U, ^{235}U and ^{232}Th chains as well as ^{40}K and ^{60}Co) from detector contaminations are negligible, since they do not penetrate into the fiducial target region [49].

Photons Photons interact with the xenon atom over three distinct mechanisms - *photoelectric absorption*, *Compton scattering* and *pair-production*. While interacting with an atom via photoelectric absorption, the photon is fully absorbed by the atom ejecting the electron out of the bound shell - leaving a positively charged xenon ion. In contrast, during Compton scattering the photon is deflected, transferring part of its energy to the orbital electron - leaving the xenon atom in an excited energy state. The third interaction of photons is over the pair production mechanism. When the energy of the photon exceeds the rest mass energy of two electrons, an electron-positron pair can be created [49].

Incident gamma-rays only interact in the outer layer of the detector, shielding the inner volume from gamma contributions. Since the target volume is shielded by several meters of water, the gamma contributions from outside of the cryostat is negligible. But radioactive contamination from the cryostat and detector materials is still a viable gamma source. Radioactive contaminations from the ^{238}U, ^{235}U and ^{232}Th chains as well as ^{40}K and ^{60}Co are the main γ- background contributors and can be minimized by target fiducialization and discrimination with the charge-to-light (S2/S1) ratio [50].

Neutrons Depending on the energy of neutrons one differs between slow ($\sim$ 1 - 10 eV) and fast neutrons ($\sim$ 1 MeV). During the inelastic scattering of the neutron, the recoil xenon nucleus is elevated to an excited state. By emitting a photon during the de-excitation, the nucleus returns to its normal energy state. Neutrons are considered as the major background contribution in dark matter detectors and thus demand a precise knowledge about their origins. Neutron induced nuclear recoils show a similar signal signature as the expected WIMP interaction and has therefore a huge impact on the WIMP sensitivity. The main neutron background contribution comes from spontaneous fission of heavy isotopes like ^{238}U and ^{232}Th in the detector components adjacent to the liquid xenon. Neutrons generated by cosmic ray muons are an additional background source and can be suppressed by including a muon-veto system and a large active water shield around the detector [45, 46].

Xenon-intrinsic backgrounds Since xenon is extracted from air it naturally contains other chemical inert noble gases. Dark matter detectors based on liquid xenon are thus confronted with background contributions from either xenon or other noble gas isotopes. ^{136}Xe is a long-lived isotope and a $2\nu\beta\beta$ emitter [51]. By purifying xenon with an appropriate purification system, xenon isotopes can be removed to substantially low concentration, but leave other noble gas isotopes still solved in xenon. The radioactivity contributions from other noble gas isotopes

like ^{39}Ar, ^{85}Kr and ^{222}Rn provide a natural source for electronic recoil background events. ^{39}Ar is not abundant in xenon and therefore does not contribute to the background. These additional contribution from other noble gases cannot be removed by chemical methods, and mix uniformly in xenon. A serious background comes from ^{85}Kr (life time of $T_{1/2} = 10.76$ years), which is an anthropogenic radioactive isotope and thus a β-emitter. Krypton can be separated to an acceptable level from xenon by cryogenic distillation. On the contrary ^{222}Rn, which is part of the ^{238}U decay chain, is constantly emitted into the xenon by the surrounding detector material, which contain radium ^{226}Ra. ^{222}Rn has a short half life time of $T_{1/2} = 3.8$d and is an α-particle emitter [45].

Neutrinos Neutrinos make up the ultimate background limit for dual-phase liquid xenon TPCs and are produced by different mechanisms. Low energetic neutrinos emitted by the sun from the pp-fusion process or the ^{7}Be reaction are the most relevant source of the electronic recoil background. They are considerably high abundant. The average background rate in the energy region (1,12) keV is $8.9 \cdot 10^{-6}$ $(\mathrm{kg} \cdot \mathrm{day} \cdot \mathrm{keV})^{-1}$ [52] and their contribution is impossible to be reduced by fidulization. The low energy solar neutrinos produce a flat electronic recoil spectrum and can only be separated from a WIMP induced nuclear recoil event by the S2/S1 ratio with a certain efficiency. Neutrinos are also able to coherently scatter with a xenon nucleus, which produces an identical signature like the expected WIMP-nucleus scattering event. Theses neutrinos originate mainly from ^{8}B process in the sun and produce a steep NR background contribution for low nuclear recoil energies. For higher nuclear recoil energies the coherent neutrino-nucleus scattering (CNNS) background comes from atmospheric neutrinos [45] and from the diffuse supernova neutrino background (DSNB) [50].

1.4.2 Scintillation Light of Liquid Xenon

Scintillation light provides a useful tool for particle detection in liquid xenon and can be used as a trigger and to infer the deposited recoil energy. By optimizing the detector geometry and developing a proper signal readout, the scintillation light can be used even further for particle identification. The main two mechanisms leading to the distinct scintillation light in the vacuum-ultraviolet (VUV) range of the electromagnetic spectrum are *excitation* (equation 1.7) and *ionization* (equation 1.8). The scintillation light of liquid xenon is peaked at 178 nm.

The two different mechanisms, which lead to the emission of ultraviolet scintillation light in liquid xenon, are shown in the equations (1.7) and (1.8). They are either induced by low-energy nuclear recoils from elastic scattering of neutrons and WIMPs on the xenon atoms or electron recoils from elastic scattering on the shell electrons from the interactions of β- and γ-rays. During the excitation process, described in equation (1.7), an incident particle E interacts with the xenon atom and excites the xenon atom (Xe^*). The excited xenon atom then recombines with a neutral xenon atom to form excimer states Xe_2^*, which subsequently decay radiatively by producing two neutral xenon atoms and a scintillation photon in the vacuum-ultraviolet region of the electromagnetic spectrum.

$$\begin{aligned} E + Xe &\rightarrow Xe^* \\ Xe^* + 2Xe &\rightarrow Xe_2^* + Xe \\ Xe_2^* &\rightarrow 2Xe + h\nu \end{aligned} \tag{1.7}$$

$$
\begin{aligned}
E + Xe &\rightarrow Xe^{+} + e^{-} \\
Xe^{+} + Xe &\rightarrow Xe_2^{+} \\
Xe_2^{+} + e^{-} &\rightarrow Xe + Xe^{**} \\
Xe^{**} &\rightarrow Xe^{*} + heat \\
Xe^{*} + 2Xe &\rightarrow Xe_2^{*} + Xe \\
Xe_2^{*} &\rightarrow 2Xe + h\nu
\end{aligned}
\tag{1.8}
$$

When an incident particle E with sufficient energy enters the liquid xenon target, it can also ionize the xenon atom (Xe^{+}). The ionized xenon created during the ionization process attracts a neutral xenon atom in order to form a xenon molecular ion (Xe_2^{+}). The positively charged xenon molecular ion recombines with a free electron, which dissociates the ion into an xenon atom (Xe) and a xenon atom in a highly excited state (Xe^{**}). The highly excited xenon atom releases heat into the surrounding xenon medium, which leaves the original highly excited xenon atom (Xe^{**}) not fully de-excited (Xe^{*}). The excited xenon dimer (Xe_2^{*}) finally decays radiatively by producing two neutral xenon atoms and a scintillation photon in the UV region of the electromagnetic spectrum. The excited xenon atom Xe^{*} can be excited either to a single or triplet state dimer Xe_2^{*}. Depending on the corresponding decay of the singlet or triplet state, the schintillation light has two different decay time constants (4 ns and 21 ns) [53, 54, 55].

1.4.3 Dual-Phase Xenon based Time Projection Chamber (XeTPC)

The XENON1T experiment or the planned DARWIN experiment (2026) are good examples for direct dark matter detection, which aim to detect WIMPs with a xenon-based dual-phase xenon projection chamber (XeTPC). The elastic scattering of WIMPs with masses of (6-1000) GeV/c^2 would produce nuclear recoils in the range of (1-100) keV. The detector system has two distinct photomultiplier arrays, which are placed at the bottom in the the liquid and at the top in the gaseous xenon. An event within the active volume of the TPC scatters on a xenon atom, which excites and ionizes the target xenon atom. The excited xenon atoms and produces prompt scintillation photons, which can be simultaneously detected by the PMT arrays on the bottom and top. These prompt scintillation photons (see equation 1.8) induce a signal known as S1 signal. Since these scintillation photons are reflected at the liquid-gas interface, the bottom PMT array includes the majority of the prompt S1 signals. The ionization electrons drift due to an external electric field through the pure liquid xenon and are transported to the gaseous xenon region at the top of the TPC. At the liquid-gas interface the electrons are extracted to the gaseous xenon region, where they experience a secondary acceleration due to an appropriate electric field. Due to the secondary acceleration the electrons emit proportional scintillation photons, which can be detected by the top PMT array. These proportional scintillation photons induce a delayed signal (S2) in the top array. Since the electron diffusion in liquid xenon is very small, the prompt scintillation signal S1 can be used for the x-y positioning of the primary event. The drift time of the ionization electrons and thus the induced delayed S2 signal can be used for the z-positioning of the primary events. Thus the ability of a 3D event reconstructing of a TPC serves as a basis for background events rejection, by applying specific cuts on the fiducial volume. The ratio of the two signals (S2/S1) are different for nuclear recoils, such as neutron and WIMP interactions, and electronic recoil events, such as β and γ-rays. The signal ratio therefore provides the basis for background discrimination and particle identification [56].

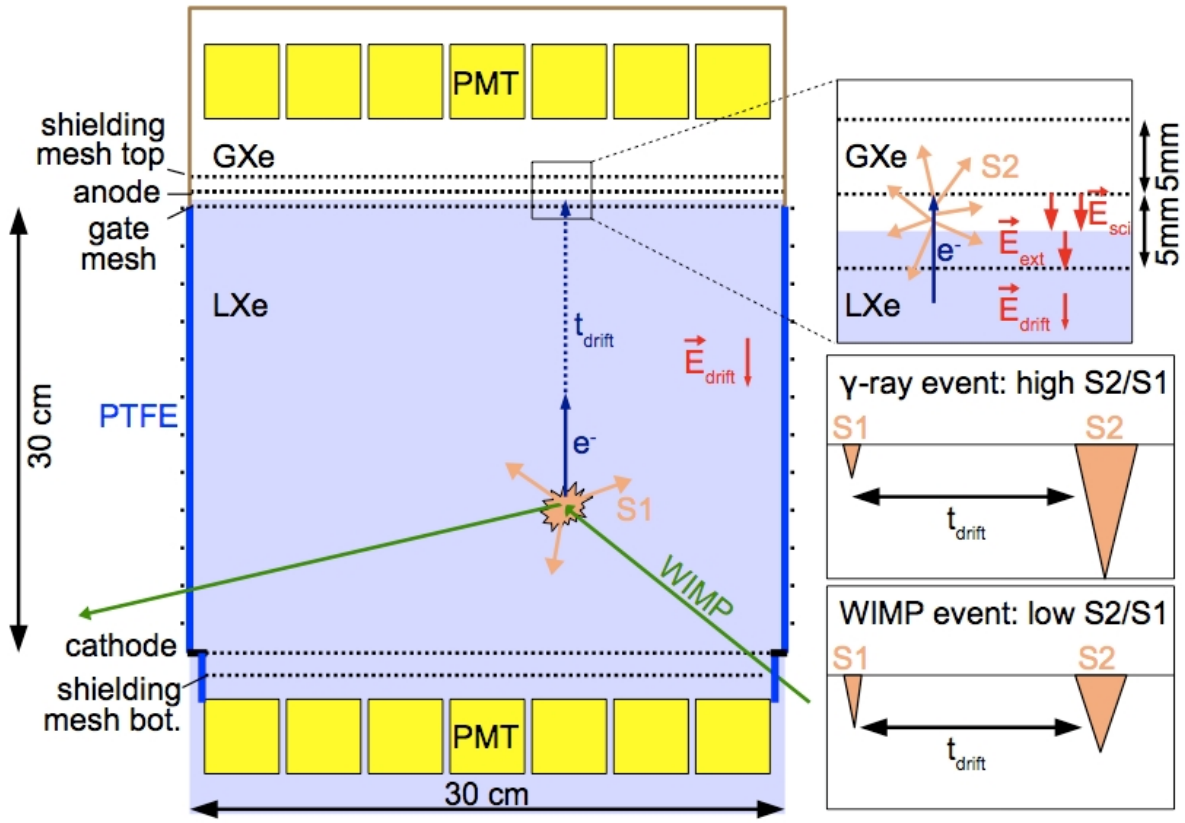

Figure 1.3: Conceptional setup of a xenon-based dual-phase Time Projection chamber (XeTPC) with a PMT array at the top and bottom of the chamber indicated by the yellow boxes. The liquid xenon volume is surrounded by PTFE reflectors indicated by the thick blue line at the edge of the TPC. A potential incident WIMP particle scatters of a xenon atom in the liquid volume. The incoming WIMP particle excites and ionizes the xenon atom and induces prompt scintillation light (S1 signal), which is detected by the bottom and top PMT arrays. The ionization electrons drift due to the external electric field to the top part of the TPC, which is displayed by the dashed blue line. After a drift time t_{drift} the electrons are extracted and accelerated to the gas phase of the TPC, producing proportional scintillation light (S2 signal) shown in the subfigure on the top right. Different incident particles give rise to different S2/S1 signal ratios, which can be used for particle discrimination. Taken from [56].

CHAPTER 2

Introduction to Silicon Photomultipliers

Since Silicon Photomultipliers are semiconductor devices a short introduction into semiconductor physics is made in this chapter. It is followed by the description of the working principle of an APD in section 2.4, which makes up the basic element of a silicon photomultiplier.

2.1 Basics of Semiconductors

Electrons are bound in free atoms to the nucleus and occupy discrete energy states. When a large amount of atoms are brought together, the energy states start to split. This is a quantum mechanical effect described by the Pauli exclusion principle, where two fermions are not allowed to occupy the same energy state. When atoms form a crystalline structure, the energy levels form rather bands instead of discrete states. The spacing between the valence band and the conduction band cannot be occupied by electrons, creating therefore a potential barrier also called a "forbidden gap". The valence band contains electrons with the highest energies and is fully filled at a temperature of absolute zero. The conduction band is located above the valence band, where free electrons contribute to the electric conductivity of a material. The band gap energy E_{G} is determined by the difference of the highest valence band energy E_{V} and the lowest energy of the conduction band E_{C}. The valence electrons are lightly bound in the valence band and are able to gain energy due to increasing temperatures. If the acquired energy $\sim k_B T$ is in the order of the energy gap E_{G}, the electrons can overcome the energy gap and are transported to the conduction band. In materials with large energy gaps in the order of E_{G} >3 eV, electrons are not able to overcome these energy gaps even at room temperatures. The valence electrons are all bound in the valence band giving no free electrons in the conduction band. These materials are so-called insulators. In conductors on the contrary, the valence and the conduction band partially overlap enabling electrons to occupy energy states in the conduction band. Silicon is a very good example for a semiconductor and is widely used as a main element for semiconductor technology applications such as the silicon photomultiplier. When silicon forms a crystalline structure, the atoms align in a diamond cubic crystal structure, where the lattice spacing is about 5.43 Å [57].

2.2 Semiconductor Doping

The conductivity of a material is dependent on the concentration of free charge carriers. In order to improve the conductivity in semiconductors, impurities are deliberately introduced. This process is called doping. There are two different ways to dope a semiconductor. One refers to a n-type doping when the conductivity is provided by electrons, or a p-type doping when the conductivity is provided by holes. A silicon atom belongs in the periodic table to the group 4, which means it has four valence electrons. Replacing a silicon atom in a silicon lattice by an atom with five valence electrons - Phosphor (P), Arsenic (As), Antimony (Sb) - leaves one valence electron without a partner. The added impurity atom of the group 5 therefore introduces a lightly bound electron,

that can move freely under the influence of an electric field (see figure 2.1.c). Since the impurity contributes an excess electron to the lattice, it is called a donor atom. The donor atom forms a new energy state - the donor level - just below the conduction band, which can be occupied by free electrons. The electrons can easily be excited into the conduction band (see figure 2.1.d).

In contrast to the n-type doping, the p-type doping process is done by introducing a foreign atom of the group 3 - Boron (B), Aluminium (Al), Gallium (Ga), Indium (In) - into the silicon lattice. The atoms from the periodic group 3 provides bonds for all silicon valence electrons, but leaves one impurity valence electron without a partner (see figure 2.1.a). These missing electrons in the valance band form mobile positively charged states called holes, which can move freely within the lattice. By implementing an acceptor atom such as B, Al, Ga or In in the semiconductor material a new energy state just above the valence band is formed. This new energy state is called the acceptor level and lies in the forbidden gap. By thermal excitation electrons from the valence band can fill the acceptor level, leaving behind a hole in the valence band (see figure 2.1.b) [58, 59].

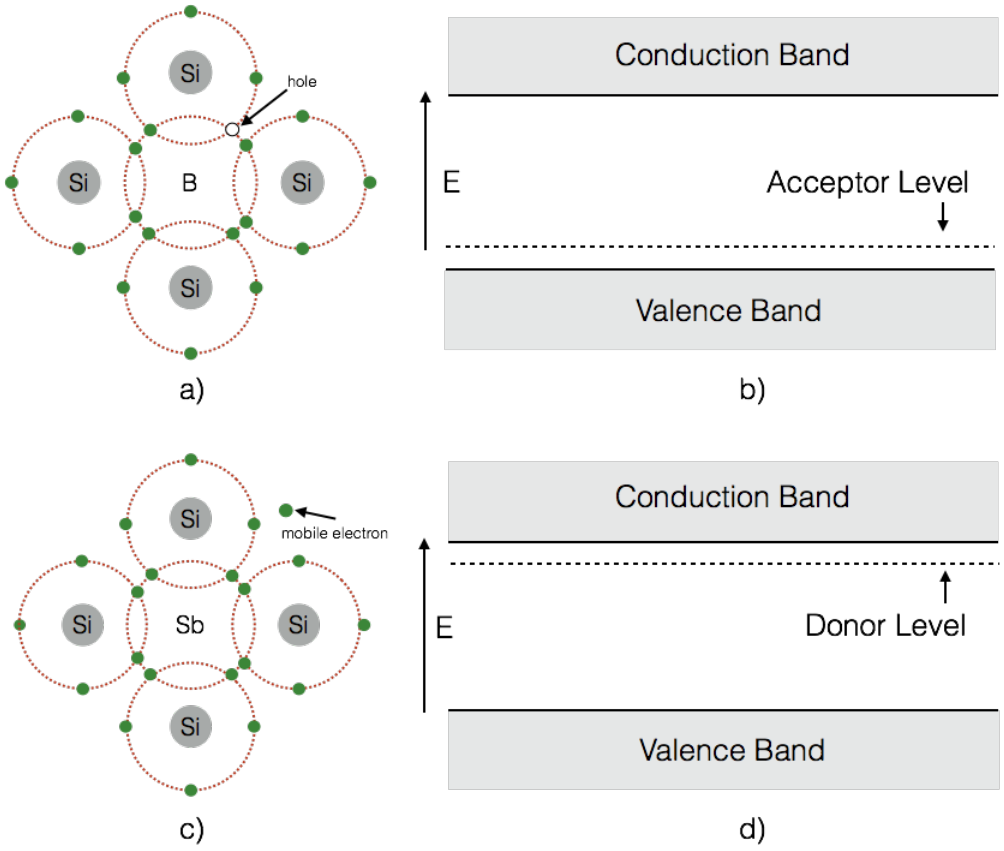

Figure 2.1: (a) Silicon lattice with a boron acceptor impurity, which leaves free moving *holes* in the crystalline silicon structure. (b) The acceptor atom creates a new energy state - the acceptor level - situated just above the valence band, which can be occupied by valence electrons through thermal excitation. (c) Silicon lattice with an antimony donor impurity, which creates free moving *electrons* in the silicon crystalline structure. (d) The newly created energy level - the donor level - is located just below the conduction band. Adapted from [59].

2.3 PN-Junction

By placing a p-type doped semiconductor adjacent to a n-type doped semiconductor one can create a p-n junction diode, which has a different electrical behaviour than the separate components. The electronic behaviour of a p-n junction can be explained with a simple flat band model. When the two differently doped semiconductors adjoin, electrons move by diffusion from the p-type region to the n-type side, while the holes move vice versa. The diffusion of electrons and holes across the junction leaves a region free of mobile charge carriers in the middle. This region is called the depletion region (see figure 2.2 - Left). Due to the diffusion of the charged carriers two adjacent space charge regions are formed, which builds up a potential barrier between the n and p regions. This potential prevents further diffusion of electrons and holes to the corresponding sides (see figure 2.2 - Right). The magnitude of the potential is dependent on the doping level of the used semiconductors. This process gives the p-n junction a capacitive property.

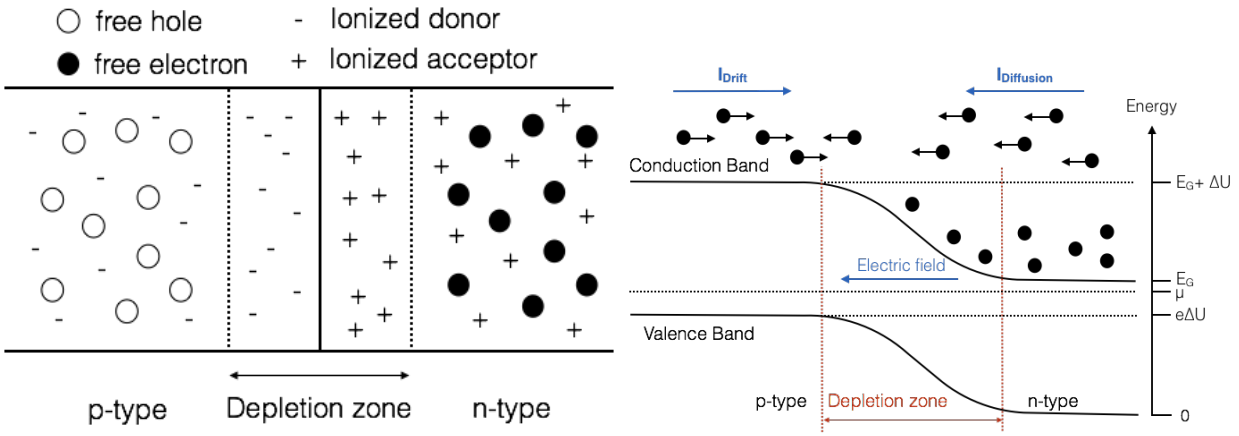

Figure 2.2: (Left) Conceptional model of a p-n junction in thermal equilibrium without any applied bias voltage. The depletion zone is formed by accumulation of ionized acceptor atoms on the right and ionized donor atom on the left, respectively. An intrinsic electric field within the depletion zone is established by the separation of the ionized donors and acceptors. (Right) Band diagram of a p-n junction with zero-bias voltage at thermal equilibrium. Electrons are indicated by the black dots - holes are not shown in this diagram, but the same arguments as for electrons can be made. If an electron from the p-side gets close to the depletion zone, it can be transported due to the intrinsic electric field in the depletion zone to the n-side of the p-n junction and contribute to the so-called drift current I_{drift}. The diffusion current $I_{\text{diffusion}}$ compensates the drift current. On the n-side the concentration of free electrons is larger. Electrons with a sufficient amount of thermal energy can overcome the electrostatic potential of the depletion zone and contribute to the diffusion current $I_{\text{diffusion}}$. Adapted from [59].

2.4 Single APD and Geiger Mode

When a p-n junction photodiode is reverse-biased, the formed electric field in the vicinity of the junction will confine electrons on the n doped side and the holes on the p side. When a photon with sufficient energy (for silicon $E_\gamma > 1.1\,\text{eV}$) is absorbed in the region of the electric field an electron-hole pair is generated. Due to the electric field the electrons will drift to the n-side and the holes to the p-side of the p-n junction. This movement of charge carriers results in a flow of a photocurrent in an external circuit. The time integration of the current yields the charge of one electron.

An **A**valanche **P**hoto**d**iode (APD) uses the same principle of a p-n junction, but is designed to support higher electric fields in the depletion zone. This can be achieved by implementing an additional higher p-doped implant (p^+) just below the n-doped side. The p^+ implant creates a sheet of additional charge that segments the p-n structure into a region of low electric field just below the implant and a high electric field above the implant. In the region of low electric field, referred to the π-layer, the incident photons are absorbed and create the electron-hole pairs. The electron then drifts into the region of higher electric field. The electron can accelerate and gain sufficient energy from the field to collide with the crystal lattice. By loosing a sufficient amount of kinetic energy during the collision it is able to generate another electron-hole pair. This process is called impact ionization. The secondary generated electron-hole pairs can accelerate again and create further electron-hole pairs by impact ionization resulting in a self-sustaining avalanche of electron-hole pair production (see figure 2.3).

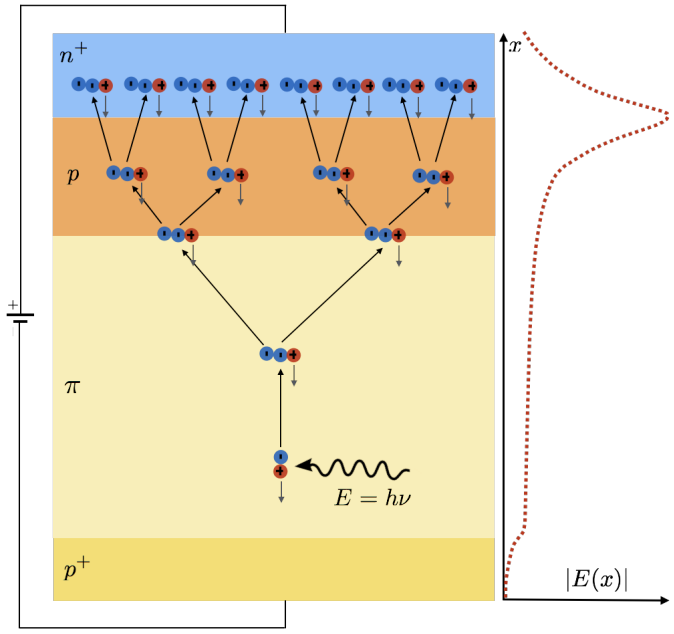

Figure 2.3: Schematic demonstration of a reverse-biased silicon-based APD. A photon with energy $h\nu$ is absorbed in the π-layer and produces an electron-hole pair. Electrons are accelerated due to the electric field to the multiplication zone (p-layer) and initiate a self-sustaining charge avalanche. The characteristic electric field (dashed red line) is a result of specific doping of the silicon layers. Adapted from [60].

When the electron-hole pairs exit the high electric field region they are collected in the crystal lattice. If the magnitude of the applied reverse-biased voltage falls below a value known as the breakdown voltage, the collection rate is higher than the creation rate. The avalanche multiplicity process dies off, resulting in the electron and hole populations to decline. However, when the reverse bias exceeds the breakdown voltage the electron-hole production rate increases on average faster than the collection rate. This configuration, where the reverse-biased voltage is higher than the breakdown voltage, is called Geiger-mode and is used to operate APDs. In fact the electron-hole population increases exponentially in time, resulting in the increased photocurrent. As long as the electric field in the junction is negligibly altered by the presence of electron-hole populations and the growing photocurrent in the junction, the external current continues to grow. In order to stabilize the growing current to a specific value of the order of a few mA, a quenching resistor R_Q is placed in series to the diode. As the current grows, the more and more voltage is dropped at the series resistance lowering the voltage across the high electric field region. The current is finally reduced to the breakdown voltage, where the production and collection rate of electron-hole pairs balance and the current is stabilized. The quenching resistor finally lowers the reverse bias voltage seen by the diode to a value below the breakdown voltage, thus halting the avalanche. The series resistance also stabilizes the current level against fluctuations. In order to use the APD for further photon detection, the bias voltage has to be set again above the breakdown voltage to the initially defined bias voltage [61].

2.5 Silicon Photomultipliers

A **Si**licon **P**hotho**m**ultiplier (SiPM) is an array of APDs connected in parallel (see figure 2.4 - Left). Each microcell or pixel of a SiPM consists of an APD operated in Geiger-mode beyond the breakdown voltage with a quenching resistor R_Q connected in series. Each microcell has the same geometrical size and is an independently operating unit, which starts an avalanche when a photon is absorbed (see figure 2.4 - Right). During an avalanche of a specific microcell all the other microcells remain fully charged and are ready to detect a photon. The active area of a SiPM, which is defined as the total occupied area of the microcell array, can range from 1 mm^2 up to 6 mm^2. The fill factor, which is the fraction of the photosensitive area over the active area, is usually in the range of $\sim 30\,\%$ up to $80\,\%$ for larger SiPMs.

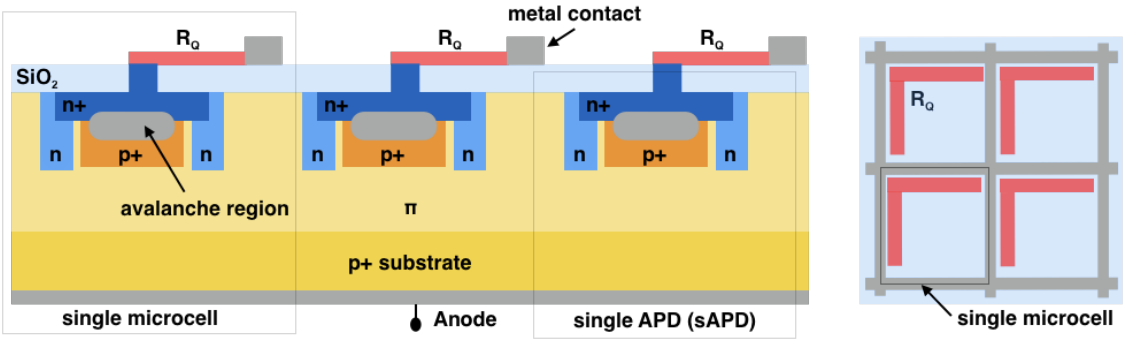

Figure 2.4: (Left) Conceptional cross section structure of a silicon photomultiplier containing three microcells. A SiPM is an array of multiple microcells of same size connected in parallel. As indicated in the first segment in the figure, a single microcell consists of a single APD (indicated by the third segment from the left) connected to a quenching resistor R_Q (red, rectangular structure). (Right) Top view of a conceptional SiPM. Adapted from [62].

SiPM-Equivalent Electronic Circuit: A silicon photomultiplier can be expressed with an equivalent electric circuit to study the signal properties. Figure 2.5 shows the equivalent circuit of a microcell of a SiPM. The Geiger-mode APD is represented with a diode capacitance C_d in reverse bias and a resistance R_S in series. The quenching resistance R_Q is connected in series. The operation of the Geiger-mode APD has tree distinct operation modes - quiescent mode, discharging phase, and recovery phase. During the quiescent mode the switch is open and the diode is reverse-biased to V_BIAS, analogously the capacitor C_D is fully charged to the bias voltage. During this phase no current is flowing until the second stage - discharge phase - is initiated by a photon absorption. The photon absorption and the avalanche process in the APD can be represented by closing the switch in the equivalent circuit. The capacitor C_D discharges from the predefined bias voltage V_BIAS to the breakdown voltage V_Break over the bulk resistance R_S. During the discharge of the capacitor the avalanche multiplication in the Geiger-mode APD is ongoing and is self-sustaining. The growing current is finally quenched by the resistance R_Q and the switch in the equivalent circuit opens again, initiating the final recovery step. In this last step the capacitor in the equivalent circuit is recharged back to the bias voltage over the quenching resistor, restoring the SiPM to its original state.

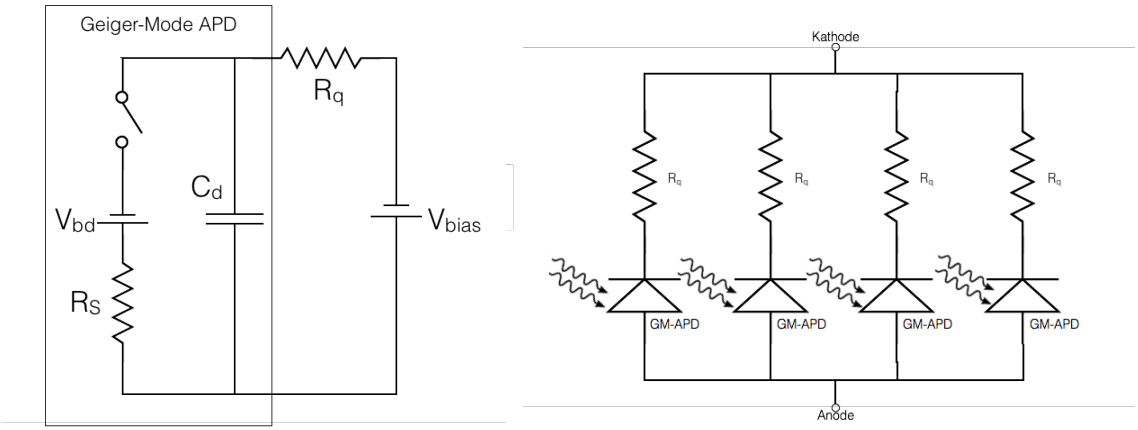

Figure 2.5: A SiPM can be described with an equivalent electronic circuit for a comprehensive understanding of its behaviour. (Left) A single microcell represented as an equivalent electronic circuit consisting of an APD and a quenching resistor R_{q}. The APD is operated in Geiger-Mode and is represented with a diode capacitance C_{d} and a resistance R_{S}. (Right) A SiPM-equivalent electronic circuit, which shows four Geiger-Mode APDs (GM-APD) connected in parallel. A GM-APD is represented here as a diode. Adapted from [63].

Pulse Shape: The signal of a SiPM is characterized by a quick rise at the beginning, which is due to the fast development of the avalanche in the diode, followed by a slow return to the baseline caused by the recharge of the fired pixel. The recovery time of the fired pixel is determined by the microcell recharge time which is given by:

$$\tau = C_D(R_Q + R_S \times N) \quad , \tag{2.1}$$

where R_{Q} is the value of the quenching resistor, C_{D} the capacitance of the microcell, N the total number of pixels, and R_{S} corresponds to the bulk resistance of the sensor. The capacitance of a microcell is dependent on its area, therefore making the recovery time of the pixel strongly dependent on the size of the different pixel sizes. A smaller pixel size results in a smaller capacitance and therefore in a shorter recovery time. With the quenching resistance R_{Q} being of the order of hundreds of kΩ and the capacitance C_{D} being several pF, the recovery time τ will have values of a few nanoseconds. When a photon is absorbed in a pixel at a time t_0, the photocurrent i_0 is increasing to a maximum value, which is dependent on the value of the quenching resistor and the over-voltage applied to the diode. The maximum current is proportional to

$$\sim (V_{\mathrm{BIAS}} - V_{\mathrm{Break}})/R_Q \quad . \tag{2.2}$$

The time integral of the current pulse $i(t)$ yields the net charge Q produced in the avalanche:

$$\int_{i(t=0)}^{\infty} i(t)dt = Q = C_D \cdot (V_{\mathrm{BIAS}} - V_{\mathrm{Break}}) \tag{2.3}$$

Although each pixel operates as a binary detector, the whole silicon photomultiplier is considered an analogue device. The output signal corresponds to the sum of all simultaneously triggered pixels. If two photons impinge the same pixel at the same time, the signal amplitude appears to be the same as if only one photon hit the pixel. If multiple pixels are fired simultaneously, the amplitude of the output signal will increase respectively. This is the reason why the number of detected photons cannot exceed the number of pixels. If the intensity of light is too high, the SiPM will saturate. Therefore a characteristic property of a SiPM is its dynamic range. The dependency of the fired pixels on the number of impinging photons can be determined as follows:

$$N_{\text{fired}} = N_{\text{tot}} \cdot \left(1 - \exp\left(-\frac{N_\gamma \cdot PDE}{N_{\text{tot}}}\right)\right) \quad , \tag{2.4}$$

where N_{tot} is the number of pixels of a SiPM, N_γ the number of impinging photons, PDE the photon detection efficiency and N_{fired} the number of fired pixels.

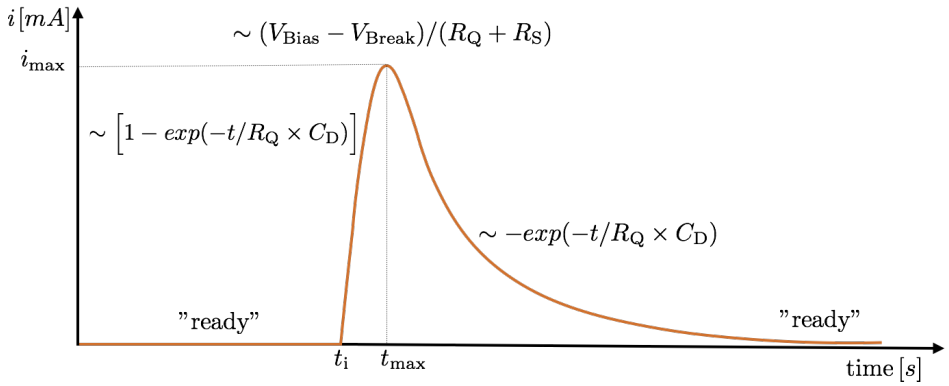

Figure 2.6: Current flow $i(t)$ of one pixel in a SiPM. The peak current i_{max} is dependent on the value of the quenching resistance R_{Q}. The capacitance C_{D} determines the rise and recovery time τ of the SiPM signal. Adapted from [62].

CHAPTER 3

Characterisation of Hamamatsu VUV3 and VUV4 Silicon Photomultipliers

SiPMs commonly used in particle physics are most sensitive for light with peak at 430 nm, which make them not suitable for xenon-based noble gas detectors. These SiPMs require a wavelength shifter (WLS) to convert the vacuum-ultraviolet (VUV) light into visible light. The VUV3 silicon photomultiplier however is a newly developed SiPM from Hamamatsu, which is sensitive to xenon scintillation light at 178 nm, hence it is a viable substitute for PMTs currently used in liquid xenon detectors. A further promising substitute is the SiPM of the VUV4 generation, which is not only sensitive to xenon scintillation light, but also to the scintillation light of argon at 128 nm. A special feature of the VUV4 generation is the windowless front side, which is able to substantially increase the photo detection efficiency (PDE). Other experiments such as MEG-II [64], nEXO [65] and Darkside-20K [66] are among a few experiments, which use VUV based SiPM arrays.

A full characterisation of three different prototype silicon photomultipliers from Hamamatsu was performed in the LArS Setup. One VUV3 $6 \times 6\,\mathrm{mm}^2$ silicon photomulitplier, which is one segment of the VUV3 $12 \times 12\,\mathrm{mm}^2$ Hamamatsu-S13371 SiPM, was tested in a first run in a gaseous nitrogen environment, whereas in a second run two VUV4 $3 \times 3\,\mathrm{mm}^2$ SiPM prototypes were characterised simultaneously in gaseous argon. The two VUV4 SiPM prototypes will be denoted for future reference as Type 10 and Type 11. All three SiPMs possess a pixel size of $50\,\mu\mathrm{m} \times 50\,\mu\mathrm{m}$. During the second run, argon was successfully liquefied and the two VUV4 prototypes were finally measured at 87 K. The following properties were measured for all three silicon photomultipliers:

- Gain as a function of the bias voltage and temperature
- Breakdown voltage
- Crosstalk probability
- Dark count rate
- Afterpulse rate
- Longterm gain and dark count stability in gaseous nitrogen at $\mathrm{T} = 170\,\mathrm{K}$ and liquid argon at $\mathrm{T} = 85\,\mathrm{K}$

The characterisation was performed at different temperatures starting at 300 K room temperature and ending at 85 K. The temperature was gradually decreased in intervals of 5 K at higher temperatures followed by an interval of 20 K for temperatures below 230 K.

3.1 Liquid Argon Setup (LArS) - Measurement facility

For the characterisation of the VUV3 and VUV4 SiPMs, the low-temperature facility LArS was used (see figure 3.1). LArS stands for **L**iquid **Ar**gon **S**etup and was especially designed for performance measurements of PMTs and SiPMs at low temperatures in either liquid argon or gaseous nitrogen. The setup was built in-house at the University of Zurich and is able to sustain a stable temperature over a long period of time. The main part of the setup is the cryostat, which contains a specially designed holding system, which is capable of mounting either a PMT or several SiPM at the same time. The inner volume is evacuated by a turbo-molecular pump to a pressure below 5×10^{-5} mbar and can be filled with argon or nitrogen with a purity of 99.9999 %. A hollow PTFE cylinder is placed between the cryostat wall and the active volume surrounding the holding system. The PTFE cylinder reduces the active area in the cryostat and therefore reduces the amount of argon or nitrogen needed during the measurement. A cylindrical, hollow, copper cooling coil, which is situated inside the upper half of the main cryostat volume, introduces gaseous nitrogen from a pressurized dewar into the vessel for cooling. The cooling coil is fed through the top flange by a double wall tube to reduce thermal conductance to the top flange. An additional copper coil is connected on the output side (outside the cryostat) to evaporate remaining liquid nitrogen 3.2. Since liquid nitrogen has a boiling point of ~ 77 K, it is a suitable coolant for liquid argon with a boiling point of ~ 87 K.

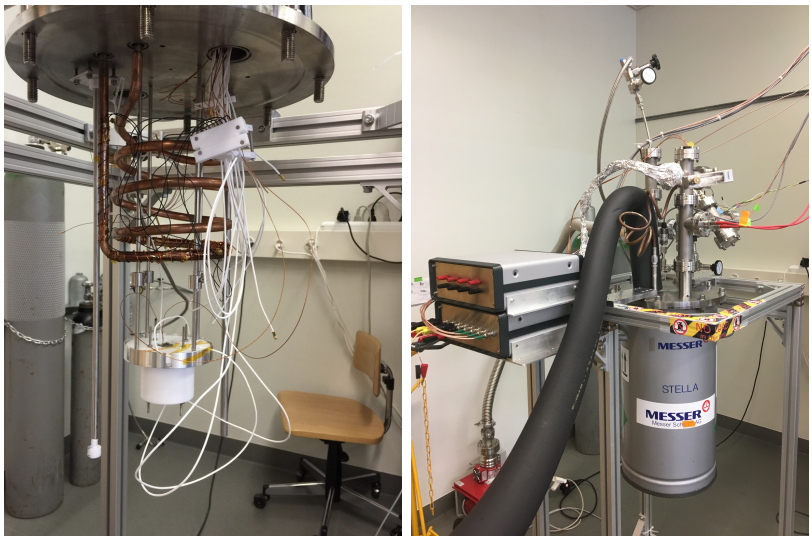

Figure 3.1: (Left) Interior of the LArS facility with the signal and power cabling. The heating foil is wrapped around the copper cooling coil. The PTFE SiPM mounting system is connected with four steel rods to the top of the cryostat. (Right) The LArS facility with an isolated liquid nitrogen hose (black) for the nitrogen insertion. Aluminium foil is used around the signal cables in order to reduce further external noise contributions. The cryostat is held with a special aluminium housing, which serves as a working platform. (Right) CAD sketch of the entire inner and outer part of the experimental setup. The outer part shows the electrical feedthroughs as well as the entire gas system, which includes the pressure and input valves as well as the liquid nitrogen output coil for a stable nitrogen flow during the data taking.

In order to measure and control the inner temperature of the cryostat, two PT-100 resistant thermometers are placed on the PTFE holding platform near the SiPM (see figure 3.3). The PT-100 are read out by a Cryo-Con32 with two channels. In order to stabilize the temperature, a heating tape is wrapped around the cooling coil in the inner part of the cryostat. The whole cooling system is therefore based on the input flow of nitrogen and the corresponding heating of the heating tape.

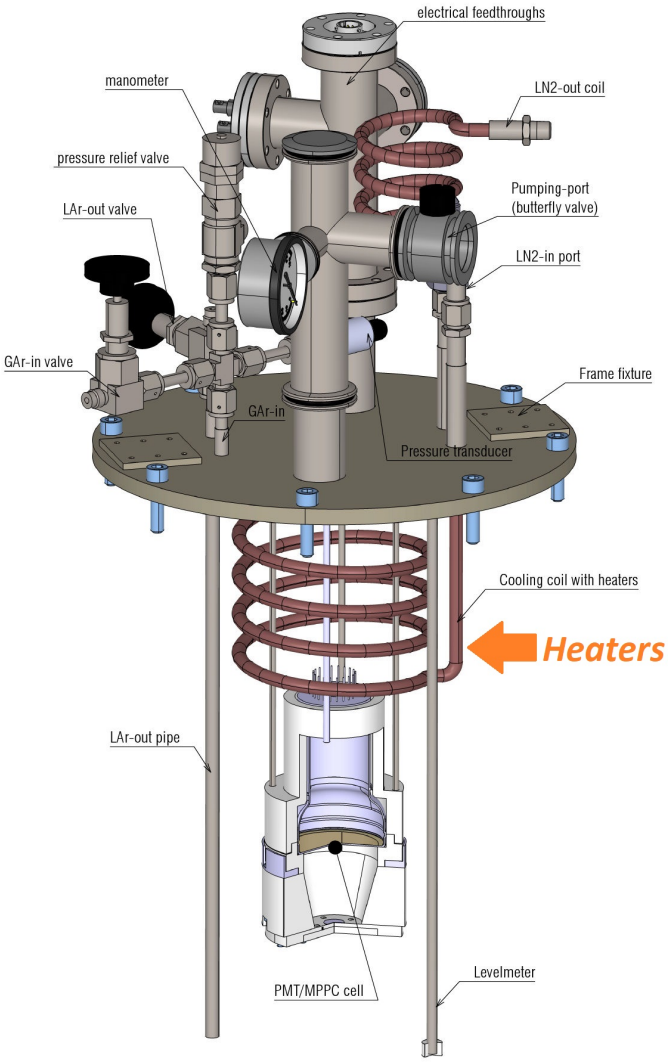

Figure 3.2: CAD sketch of the entire inner and outer part of the LArS setup. The outer part shows the electrical feedthroughs as well as the entire gas system, which includes the pressure and input valves as well as the liquid nitrogen output coil for a stable nitrogen flow during the data taking.

By setting a specific threshold temperature on the thermometers with a PID controller (Cryo-Con 32), the heating power of the heating tape balances the high input flow of the nitrogen and therefore stabilizes the inner temperature of the cryostat. By increasing the nitrogen flow and setting a specific threshold temperature on the temperature, precise temperatures can be achieved.

For a gain calibration at lower temperature a blue LED (λ =470 nm) is installed inside the top part of the active volume, just below the SiPM PTFE base. The LED is connected outside to a pulse generator (AIM-TG5010A), which powers the LED and is able to generate pulses with a specific rise and fall time. The electrical connections are realised by employing feedthroughs in several CF-40 flanges. The voltage cable for the operation of the SiPM as well as the two PT100 resistant thermometers and the LED are fed through a potted CF40 flange, whereby the signal cable are realised by a BNC feedtrough over a separate CF-40 flange. The signals coming from the SiPM are amplified outside of the experimental setup with a $\times 100$ amplifier (RF-BAY-LNA-1440) and are fed to a CAEN V1730D ADC module.

During the characterisation of the SiPMs the temperature was continuously monitored. Figure

3.4 shows the stepwise decreasing temperature, where each plateau represents a stable maintenance of the temperature and the data taking time interval. The fluctuation of the temperature (see Figure 3.4 - right) is small ($\sim$ 20 mK) and supports a temperature-dependant characterisation of the SiPM down to 110 K within a gaseous nitrogen environment in the cryostat. In a secondary characterisation run, argon was successfully liquified in the cryostat, and the temperature of 87 K was maintained. The liquid argon facility is therefore a reliable and suitable experimental setup for the characterisation of SiPMs.

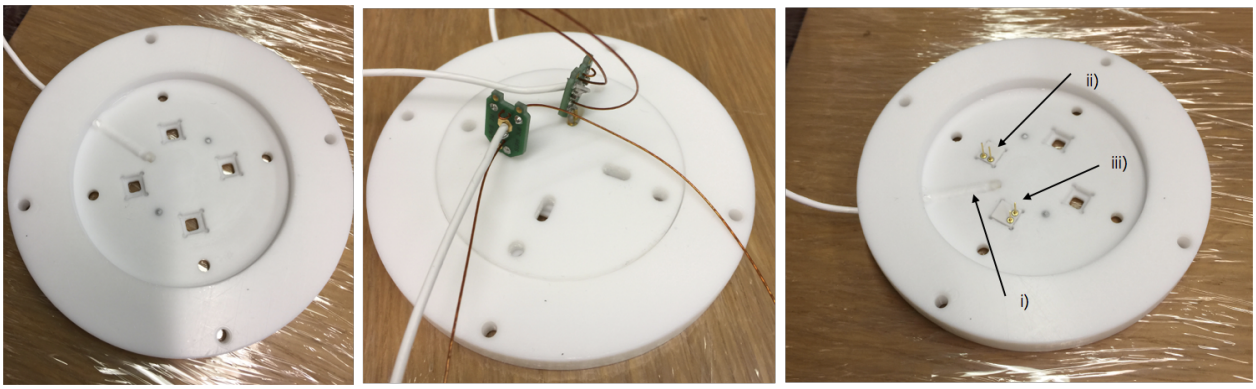

Figure 3.3: (Left) The PTFE SiPM holding disk with four distinct mounting places for SiPMs with the dimensions of $3 \times 3\,\mathrm{mm}^2$. (Middle) The rear side of the PTFE holding system with the installed VUV4 SiPM of the Type 10 on the left and Type 11 on the right. The SiPMs are connected with the readout board, which is equipped with a white PTFE coaxial signal cable and two kapton-insulated copper cables for the grounding and power supply. (Right) (i) shows one PT100 resistant thermometer, which is placed as near as possible to the SiPM through a drill-hole. The temperature is externally set on this thermometer. (ii) and (iii) show the rear side of both $3 \times 3\,\mathrm{mm}^2$ SiPMs with the connection pins.

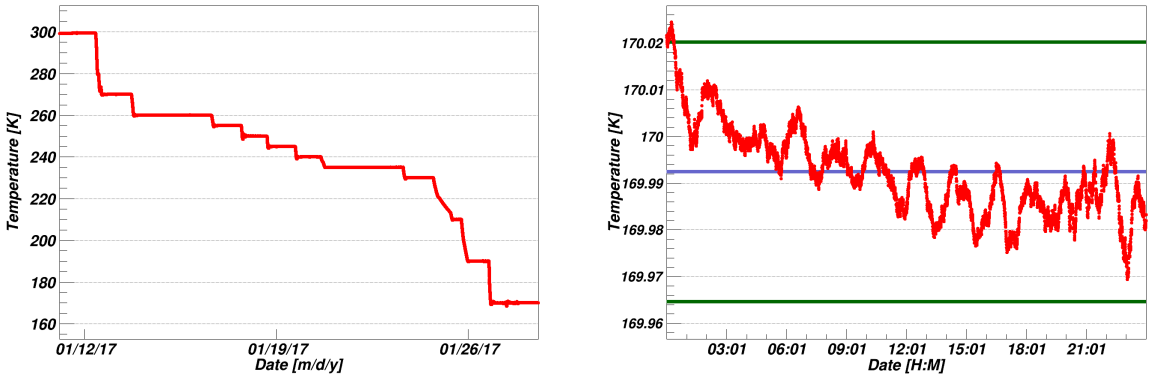

Figure 3.4: (Left) Temperature evolution in the LArS facility. The plot shows a controlled, gradually decreasing temperature from 300 K to 170 K within the cryostat. (Right) The temperature can be stabilized within 20 mK with the installed heating/cooling mechanism. The fluctuation of the temperature is negligible. The green lines show the $3 \times$ RMS of the temperature measurements. The blue line corresponds to the mean temperature during the entire data taking period. The 170 K temperature evolution is a zoom from the last temperature setting from the left figure.

3.2 Read-out Electronics

For a full characterisation of the VUV3 $6 \times 6\,\mathrm{mm}^2$ and the VUV4 $3 \times 3\,\mathrm{mm}^2$ SiPMs, an appropriate electronic readout board (see Figure 3.5) was used [60]. The electronic read-out board is composed of a low-pass filter, which stabilizes the bias voltage from the power supply and cuts off high frequency noise contributions. Further a read-out capacitor of 10 nF and a resistor of 50 Ω are implemented to the read-out board. The small current pulses produced by SiPMs are fed through the read-out capacitor and the resistor, thus generating measurable voltage signals. The voltage signals are then fed to an externally located, low noise $\times 100$ amplifier. The read-out boards are considerably small and less complex in their setup. The need for less electronic components and the choice of an external amplification, reduces further the radioactivity contributions in a potential implementaion of the read-out boards in a time projection chamber such as DARWIN.

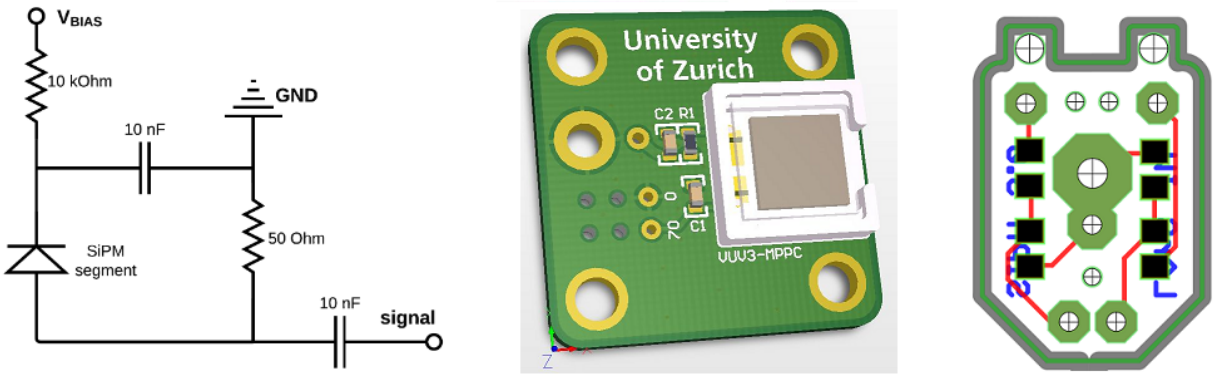

Figure 3.5: (Left) Electronic read-out schematics incorporating a low-pass filter and a read-out capacitor. CAD sketches of the read-out board designed for the VUV3 $6 \times 6\,\mathrm{mm}^2$ (Middle) and the VUV4 $3 \times 3\,\mathrm{mm}^2$ SiPMs (Right), respectively.

3.3 WARP - Offline Data Processing Tool

During the data acquisition process the tested SiPM was powered at different over-voltage settings, which were changed in an interval of 0.4 V. A total of 500'000 waveforms, which contain the waveforms of the respective signal pulses produced by the SiPM and electronic noise components, were taken at every voltage setting during the data acquisition. The acquired data was then processed with an in-house developed data processor called WARP [67]. The offline data processor uses the first 200 ns of the predefined time window to calculate the baseline (see Figure 3.6). This step is important, since one is only interested in the signal in respect to the real zero value. Without this intermediate step, the later integration of the signal area would be overestimated, resulting in wrong determination of the gain.

If a random signal is confined in the baseline calculation time interval, the baseline would be miscalculated and therefore falsify the real signal amplitude. These waveforms are later discarded with an appropriate RMS cut (RMS > 9) in the analysis procedure. Once the baseline is calculated the peak finder scans the waveforms for excursions above $3\times$ of the calculated RMS. If this threshold is exceeded by a signal, the integration of the pulse starts. As soon as the signal falls below the $3\times$ RMS threshold, the integration period is stopped and yielding the total area under the signal pulse. Peaks at the edge of the time interval can be truncated and can therefore not be integrated fully. These events are discarded later with an additional data quality cut during the offline analysis. In order to avoid clipping of the pulse shape due to the saturation of the ADC range, low over-voltages were applied to the SiPM. The integrated peaks are stored into a ROOT file, which contains all the characteristic calculated properties such as peak height, peak position, and peak width.

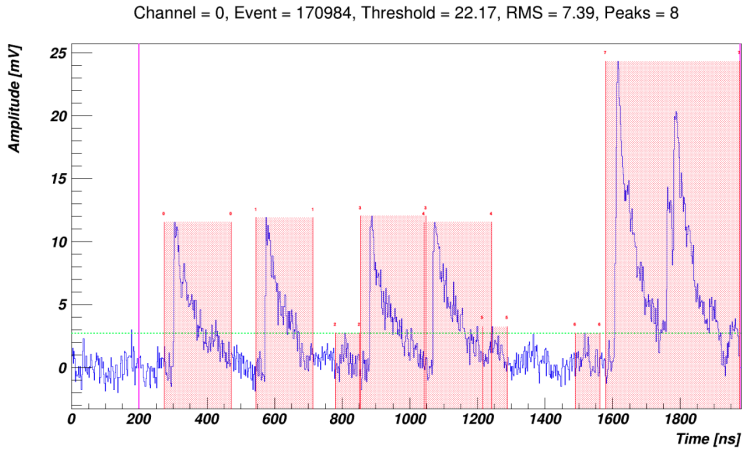

Figure 3.6: Example of waveforms of the VUV3 $6\times6\,\mathrm{mm}^2$ SiPM during data taking with a LED. The first four signals show a 1 photo-electron (p.e.) signal with the first one including an afterpulse event. The last waveform shows a 2 p.e. signal with an additional pile-up signal. The amplidtude is twice as high as the one from a 1 p.e. signal, indicating simultaneous firing of two pixels. The offline WARP processor is not able to distinguish the two signals, integrating therefore over the whole range. This kind of events will be neglected with a proper position cut during the offline data analysis.

3.4 Gain Calibration

The gain G is defined as the number of carriers contained in the single-cell current pulse, since this is the number of carriers generated during the avalanche in response to an absorbed photon. Integrating the current pulse over time yields the total charge Q that is transferred between the terminals of one SiPM pixel. Since the transfer is triggered by a single charge carrier, the gain is equal to :

$$G = \frac{Q}{e}. \tag{3.1}$$

Silicon photomulipliers are operated at a slightly higher bias voltage than the breakdown voltage. The difference of the bias voltage V_{Bias} and the breakdown voltage V_{Break} is the over-voltage ΔV.

$$\Delta V = V_{\text{Bias}} - V_{\text{Break}} \tag{3.2}$$

Since the performance of a SiPM is thus dependent on the over-voltage, the gain can be calculated from the over-voltage ΔV, the pixel capacitance C_j and the electron charge e as following:

$$G(\Delta V) = \frac{C_j}{e}\Delta V, \tag{3.3}$$

where C_j is the capacitance of a pixel j and e the elementary charge. For a subsequent temperature-dependent gain analysis, the individual parameters need to be considered to be variable in temperature as well. For that matter the breakdown voltage V_{Break} and the pixel capacitance C_j are considered to be temperature-dependent, whereas the bias-voltage V_{Bias} is held constant. Equation 3.3 therefore becomes:

$$G(\Delta V) \rightarrow G(T) = \frac{C_j(T)}{e}\Big(V_{\text{Bias}} - V_{\text{Break}}(T)\Big). \tag{3.4}$$

The total temperature derivative of the gain dG/dT from equation 3.4 is determined as the following:

$$\frac{\mathrm{d}G}{\mathrm{d}T} \overset{(3.4)}{=} \underbrace{\left(\frac{\partial G}{\partial T}\right)}_{=0} + \left(\frac{\partial G}{\partial \Delta V}\right)\left(\frac{\mathrm{d}\Delta V}{\mathrm{d}T}\right) + \left(\frac{\partial G}{\partial C_j}\right)\left(\frac{\mathrm{d}C_j}{\mathrm{d}T}\right) \tag{3.5}$$

$$\text{with} \quad \left(\frac{\mathrm{d}\Delta V}{\mathrm{d}T}\right) = \underbrace{\left(\frac{\partial \Delta V}{\partial T}\right)}_{=0} + \left(\frac{\partial \Delta V}{\partial V_{\text{Bias}}}\right)\underbrace{\left(\frac{\mathrm{d}V_{\text{Bias}}}{\mathrm{d}T}\right)}_{=0} + \left(\frac{\partial \Delta V}{\partial V_{\text{Break}}}\right)\left(\frac{\mathrm{d}V_{\text{Break}}}{\mathrm{d}T}\right) \tag{3.6}$$

$$\rightarrow \quad \frac{\mathrm{d}G}{\mathrm{d}T} = \frac{1}{e}\left(\frac{\mathrm{d}C_j}{\mathrm{d}T}\Delta V - \frac{\mathrm{d}V_{\text{Break}}}{\mathrm{d}T}C_j\right). \tag{3.7}$$

Hence, the gain features a temperature dependent characteristic on the basis of assuming the breakdown voltage and the pixel capacity not to be temperature invariant.

Gain Analysis

For the gain calibration an experimental setup shown in Figure 3.7 was used. Since the dark count rate at 260 K is already too low for a gain calibration, the LED was necessary to perform the calibration at low temperatures.
Every measured charge Q for a specific SiPM, powered at a chosen bias voltage, gives a specific charge spectrum (see figure 3.8). Each peak in the charge spectrum corresponds to multiple photo-electrons. The first peak is symmetrical around zero and corresponds to the noise peak. By fitting the 1 p.e. peak with a Gaussian function one can evaluate the gain G at a specific bias voltage. The fitting function has the following form:

$$f(x) = A \cdot exp\left(\frac{(x-G)^2}{2\sigma^2}\right), \tag{3.8}$$

where A corresponds to the peak height, G the peak position and σ the standard deviation of the Gaussian distribution. The peak position G gives the gain. By doing this procedure for several charge distribution at different bias voltages, one yields the bias voltage dependent gain. By increasing the bias voltage, the 1 p.e peak shifts to higher values and therefore increasing the gain. As expected the gain increases linearly with the bias voltage. The different gain values were then fitted with a linear function of the form:

$$f(x) = p_0 + p_1 \cdot x, \tag{3.9}$$

where p_0 is the y-axis intercept and p_1 the slope of the linear function. The slope p_1 can later be used with equation (3.3) for the determination of the pixel capacitance C_j. The intercept of the linear function with the x-axis yields the breakdown voltage, where the gain G is zero.

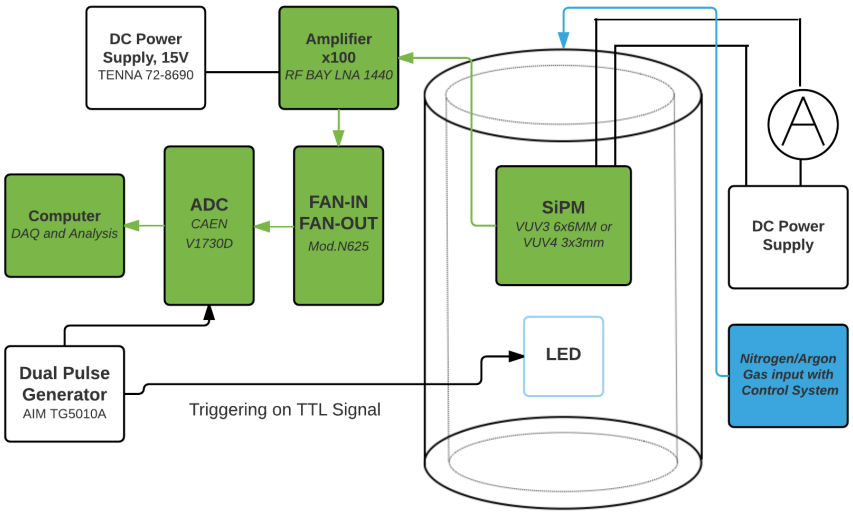

Figure 3.7: Experimental setup for the gain calibration. The SiPM in the cryostat of the LArS setup is illuminated with a blue LED (λ =470 nm), which is triggered and powered by an external dual pulse generator (AIM TG5010A). The signal is fed through an external $\times$ 100 amplifier (RF BAY LNA-1440) to the ADC (CAEN V1730D), which is also triggered by the dual pulse generator (AIM-TG5010A). The signal is then fed to the computer for DAQ (Data Acquisition) and offline analysis.

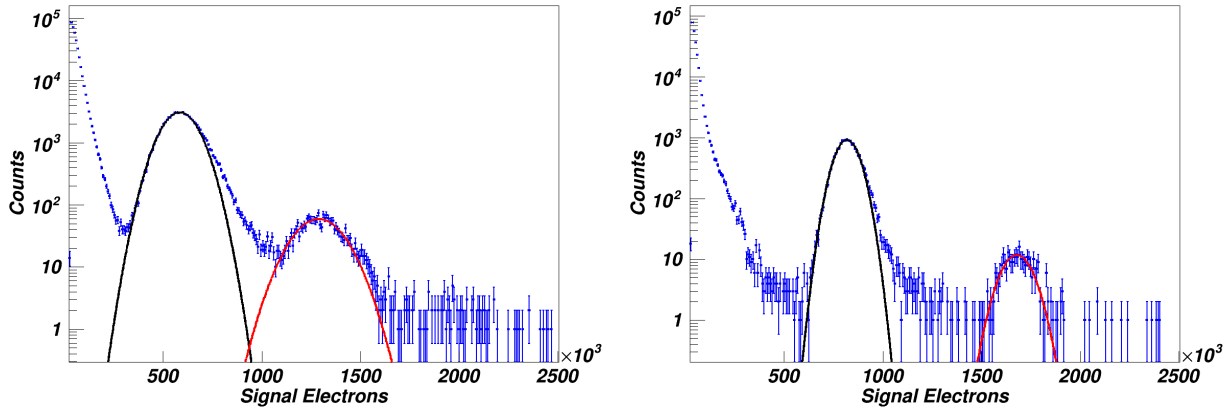

Figure 3.8: An example of a single photo-electron (SPE) Spectrum for the VUV3 $6 \times 6\,\mathrm{mm}^2$ SiPM (Left) and the VUV4 $3 \times 3\,\mathrm{mm}^2$ SiPM (Right) measured at T = 270 K. The first peak is used for the gain evaluation by fitting it with a Gaussian function (black Gaussian fit). The red Gaussian fit corresponds to the 2 p.e. peak.

Gain Results

The gain for VUV3 (see Figure 3.10, left) and VUV4 SiPM of Type 10 (see Figure 3.11, left) and Type 11 (see Figure 3.11, left) were measured at different temperatures (170 K - 300 K) and different over-voltages. The measurements for the VUV4 SiPM of Type 10 and 11 were performed in gaseous argon, while the VUV3 $6 \times 6\,\mathrm{mm}^2$ SIPM was characterized in gaseous nitrogen. The gain measurements were fitted at each temperature T with a linear function (equation 3.9), which yields the slope $p_1 = C/q$, where C is the pixel capacitance and q the electric charge. Evaluating every x-axis intersection of the gain function (equation 3.3) at every temperature T, where the over-voltage $\Delta V = 0$, results in the evaluation of a temperature-dependent breakdown voltage (see Figure 3.10 (Right), Figure 3.11 (Right), Figure 3.12 (Right)) The temperature-dependent breakdown voltages are fitted with a linear function for both VUV3 and VUV4 SIPMs of Type 10 and 11 (see Table 3.2 and A.1 for obtained results).

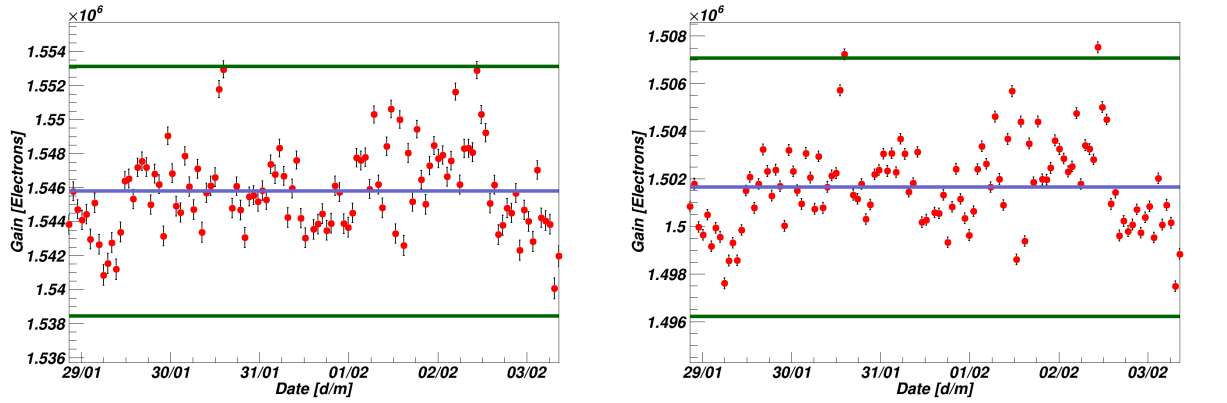

Figure 3.9: Gain evolution for the VUV3 $6 \times 6\,\mathrm{mm}^2$ at an over-voltage of $V_{\mathrm{OV}} = 7.0\,\mathrm{V}$ (Left) and VUV4 Type 11 SiPM at an over-voltage of $V_{\mathrm{OV}} = 4.3\,\mathrm{V}$ (Right) during 5 days of data-taking at T = 170 K. The purple line shows the mean gain and the green lines the $3 \times$ RMS interval. The gain fluctuation is less than 1 % for both SiPMs during the entire data-taking period.

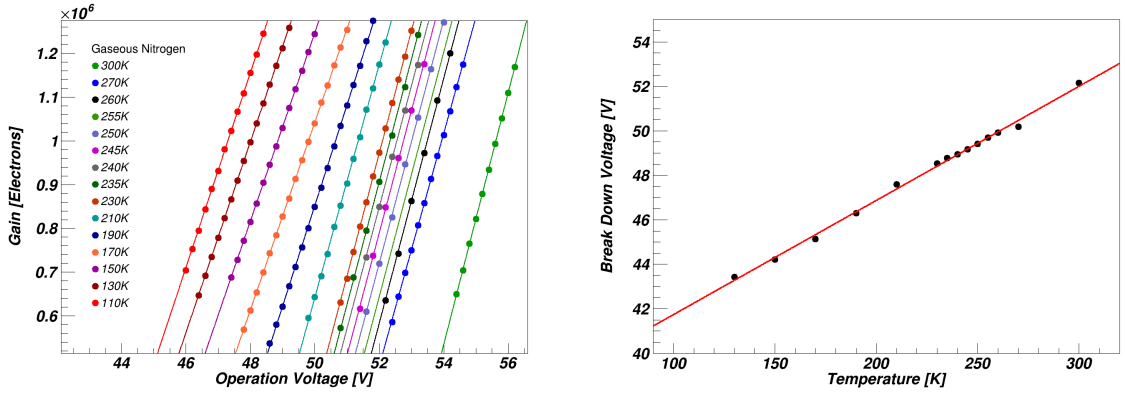

Figure 3.10: (Left) Temperature-dependent gain measurements for the VUV3 $6 \times 6\,\mathrm{mm}^2$ SiPM in gaseous nitrogen (Right) Temperature dependent breakdown voltages for VUV3 $6 \times 6\,\mathrm{mm}^2$ SiPM. The slope of the fit is $p_1 = (51.3 \pm 0.8)\,\mathrm{mV/K}$.

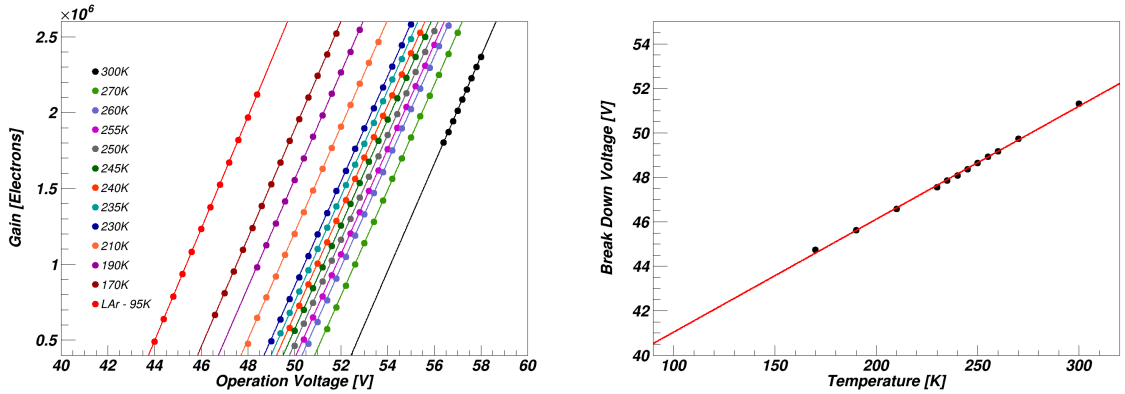

Figure 3.11: (Left) Temperature-dependent gain measurements for the VUV4 SiPM Type 10 in gaseous argon (Right) Temperature dependent breakdown voltages for VUV4 SiPM of Type 10. The slope of the fit is $p_1 = (50.8 \pm 0.6)\,\mathrm{mV/K}$.

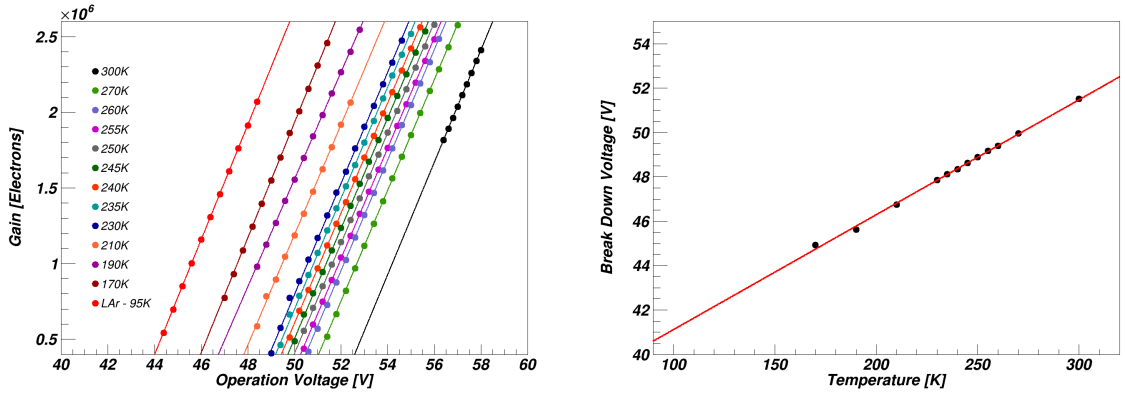

Figure 3.12: (Left) Temperature-dependent gain measurements for the VUV4 SiPM Type 11 in gaseous argon (Right) Temperature-dependent breakdown voltages for VUV4 SiPM of Type 11. The slope of the fit is $p_1 = (51.8 \pm 0.7)\,\mathrm{mV/K}$.

The gain measurements of all three SiPM models shown in Figure (3.10, 3.11 and 3.12 - left) confirm the predicted linear behaviour from equation 3.3. The gain changes linearly to the applied over-voltage at a certain temperature setting. The linear change of the breakdown voltage seen in Figure (3.10, 3.11 and 3.12 - Right) for each SiPM model results in the shift of the gain with decreasing temperatures. The temperature-dependent gain is thus a result of the temperature-dependent behaviour of the breakdown voltage. The effective capacitance of the SiPM is considered to be constant over temperature and has hence no implications on the temperature dependence of the gain [68]. The sudden change in the effective capacitance of the VUV4 $6 \times 6\,\mathrm{mm}^2$ SiPM at $\mathrm{T} = 210\,\mathrm{K}$ could be reconstructed with a second measurement, but always showed a constant behaviour before and after the drastic change. The effective capacitance C_{eff} at high temperatures of $\mathrm{T} = 300\,\mathrm{K}$ is $C_{\mathrm{eff}} = (460.8 \pm 0.6)\,\mathrm{fF}$ and changes at a temperature of $\mathrm{T} = 210\,\mathrm{K}$ rapidly to a constant value of $C_{\mathrm{eff}} = (356.4 \pm 0.2)\,\mathrm{fF}$ at $\mathrm{T} = 170\,\mathrm{K}$. The effective capacitance of the VUV3 SiPM of Type 10 and 11 are constant over temperature, which is indicated by the slope of the temperature-dependent gain measurements. For both VUV3 SiPMs an effective capacitance of $C_{\mathrm{eff}} = (567.2 \pm 0.3)\,\mathrm{fF}$ at $\mathrm{T} = 300\,\mathrm{K}$ and $C_{\mathrm{eff}} = (573.3 \pm 0.2)\,\mathrm{fF}$ at $\mathrm{T} = 170\,\mathrm{K}$ was measured. Thus, considering equation 3.7 the total derivative dC/dT is negligible for both VUV4 SiPMs and the temperature dependence of the gain can be entirely deduced to the temperature-dependent breakdown voltage.

For future implementation of the SiPM in a TPC, the gain stability over time at cryogenic temperatures needs to be guaranteed. Hence, a gain stability measurement at $\mathrm{T} = 170\,\mathrm{K}$ was performed for all three SiPM models. Figure 3.9 shows the gain stability measurement for the VUV4 $6 \times 6\,\mathrm{mm}^2$ SiPM in gaseous nitrogen and the VUV4 SiPM of Type 10 in gaseous argon. Further, a second gain stability measurement for all three SiPM models in liquid argon ($\mathrm{T} = 87\,\mathrm{K}$) was performed over a time period of one month (see figure A.1). In conclusion all three SiPM models show a stable gain at cryogenic temperatures and are thus suitable for the use in potential experiments operated at cryogenic temperatures.

SiPM Model	V_{Break} **[V]**	**Over-Voltage** V_{over} **[V]**		
		Gain 1.0 $\times 10^6$	**Gain** 1.5 $\times 10^6$	**Gain** 2.0 $\times 10^6$
Temperature $\mathrm{T} = 170\,\mathrm{K}$				
VUV3 $6 \times 6\,\mathrm{mm}^2$	45.14 ± 0.04	4.66 ± 0.04	7.00 ± 0.04	9.33 ± 0.04
VUV4 Type 10	44.73 ± 0.03	2.79 ± 0.03	4.19 ± 0.03	5.59 ± 0.03
VUV4 Type 11	44.93 ± 0.07	2.62 ± 0.07	3.94 ± 0.07	5.25 ± 0.07
Temperature $\mathrm{T} = 270\,\mathrm{K}$				
VUV3 $6 \times 6\,\mathrm{mm}^2$	50.17 ± 0.04	$3.77 \pm$,0.04	5.65 ± 0.04	7.53 ± 0.04
VUV4 Type 10	49.72 ± 0.03	2.88 ± 0.03	4.13 ± 0.03	5.75 ± 0.03
VUV4 Type 11	49.95 ± 0.03	2.73 ± 0.03	4.10 ± 0.03	5.46 ± 0.03

Table 3.1: Breakdown voltage V_{break} and over-voltage V_{over} measurements for VUV3 $6 \times 6\,\mathrm{mm}^2$, and VUV4 of Type 10 and 11, respectively. Measurements were performed at temperatures of $\mathrm{T} = 170\,\mathrm{K}$ and $\mathrm{T} = 270\,\mathrm{K}$. The error on the bias-voltage is $\pm 1\,\mathrm{mV}$. For an extensive list of results see A.1.

3.5 Noise Contributions

In silicon photomultipliers there are several noise characteristics, which can be divided into uncorrelated noise and pixel discharging correlated noise. An example for an uncorrelated noise is the dark count rate, whereas crosstalk and afterpulse are pixel discharging correlated noise contributions.

3.5.1 Dark Count Rate

In the absence of light it is still possible for a signal to be produced by thermally generated carriers (electrons and holes) in the silicon substrate of the photomultiplier. If an electron or a hole is generated in the active area of the silicon photomultiplier an avalanche is initiated, which results in a measurable output signal. This kind of output pulse has a 1 p.e. amplitude and is indistinguishable with a photo-generated one. This is called Dark Current. There is a finite probability $p(T)$ for an electron-hole pair to be produced by thermal excitations leading to these specific dark count events:

$$p(T) = CT^{3/2}e^{-\frac{E_g}{2k_BT}}, \tag{3.10}$$

where T is the absolute temperature, E_g the bandgap energy, k_B the Bolzmann constant and C refers to the proportionality constant which is dependent on the used silicon doping material [69].

There are two different processes, which lead to the generation of free charge carriers. The first process is referred as the Shockley-Read-Hall process. During this process electrons are transferred from the valence to the conduction band over an intermediate state (trap) within the band gap. This process is highly dependant on the temperature and is sensible to the density and relative energy of these traps (Equation 3.10). Impurities in the silicon lattice generate these traps and are therefore the main contribution of a high dark count rate (DCR) at temperatures above 230K. The second process is sensitive to high electric fields in the depletion zone of the silicon photomultiplier. Due to these high electric fields charge carriers either directly tunnel from the valence to the conduction band or are transferred over a trap-assisted tunneling effect. Due to the high sensitivity of the electric field , the DCR is therefore expected to be dependent on the bias voltage [68].

Dark Count Rate Analysis

In order to measure the DCR, an experimental setup (see Figure 3.13) containing a leading-edge discriminator (CAEN V895B) and a scaler module (CAEN V830AC) was used. The DCR measurement of the VUV3 SiPM was performed in the LArS setup at different temperatures in gaseous nitrogen. For the second measurement run the two VUV4 SiPMs of Type 10 and 11 were tested in a gaseous argon environment. In order to measure the DCR of all three SiPMs a specific procedure was performed. By increasing the threshold of the discriminator within intervals of 1mV and counting the number of events with the scaler module, a threshold-dependent DCR was measured. This procedure was done for several temperatures at 15 different over-voltage settings in an interval of 0.4 V. Every specific point of the threshold-dependent DCR step function seen in Figure 3.14 represents the calculated median of the acquired data within a specific time interval. By interpolating two intermediate data points the threshold-dependent DCR could be fitted in an offline analysis procedure. In order to extract the specific threshold for the later evaluation of the crosstalk probability, the gain calibration for each SiPM was used.

The threshold-dependent DCR plot is characterised by a series of plateaus, where the values decrease sharply for specific thresholds. Since the dark count signals have a discrete pulse area, one expects also a discrete pulse height for various p.e. populations. Once the threshold of the discriminator exceeds the threshold of a certain p.e. population, the DCR rate drops drastically. This manifests itself in these characteristic DCR plateaus. Taking this fact into account the signal

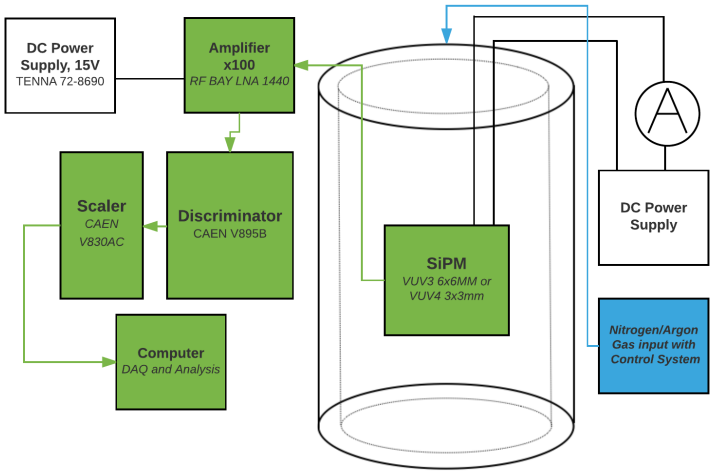

Figure 3.13: Experimental setup for threshold-dependent DCR measurement.

height spectrum from the gain calibration was used to fit the 1 p.e. population with a Gaussian. Figure 3.15 shows the measured pulse height spectrum with the Gaussian fit. With this fitting procedure one can evaluate the pulse height for the 0.5 p.e and 1.5 p.e populations. Knowing the threshold value for the 0.5 p.e. and 1.5 p.e. and the corresponding pulse heights, one can extract the over-voltage dependant dark count rate. Figure 3.14 shows the over-voltage dependent DCR at a specific temperature (T = 270 K).

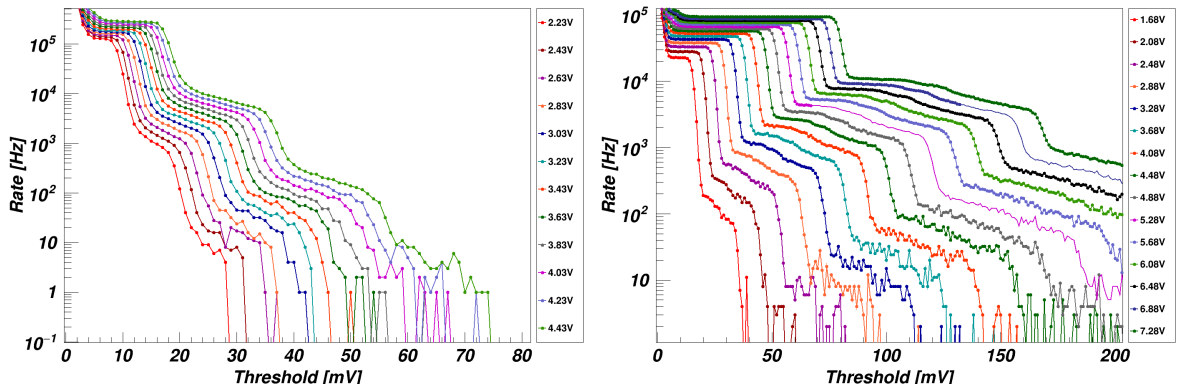

Figure 3.14: (Left) Measurement of the threshold-dependent DCR of the VUV3 $6 \times 6\,\mathrm{mm}^2$ SiPM at T = 270 K. The coloured curves represent different over-voltages. (Right) Measurement of the threshold-dependent DCR of the VUV4 $3 \times 3\,\mathrm{mm}^2$ SiPM of Type 10 at T = 270 K. The coloured curves represent different over-voltages.

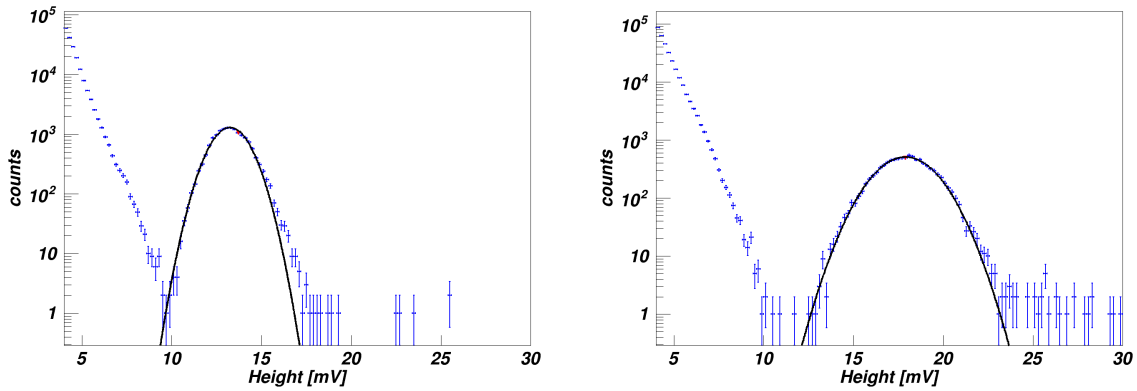

Figure 3.15: (Left) Pulse amplitude p.e. spectrum of the VUV3 $6 \times 6\,\mathrm{mm}^2$ SiPM at T = 270 K. The first two p.e. peaks are fitted by a Gaussian to determine the 0.5 p.e. and the 1.5 p.e. thresholds respectively. (Right) Pulse amplitude p.e. spectrum of the VUV4 $3 \times 3\,\mathrm{mm}^2$ SiPM of Type 10 at T = 270 K. The first two p.e. peaks are fitted by a Gaussian to determine the 0.5 p.e. and the 1.5 p.e. thresholds respectively.

Dark Count Rate Results

The DC rates were measured at different temperatures for various over-voltages and were fitted with a linear function for each specific temperature setting. Figure 3.16 shows an exemplary linear fit for the VUV3 $6 \times 6\,\mathrm{mm}^2$ and the VUV4 SiPM of Type 10 at a temperature of T = 245 K.

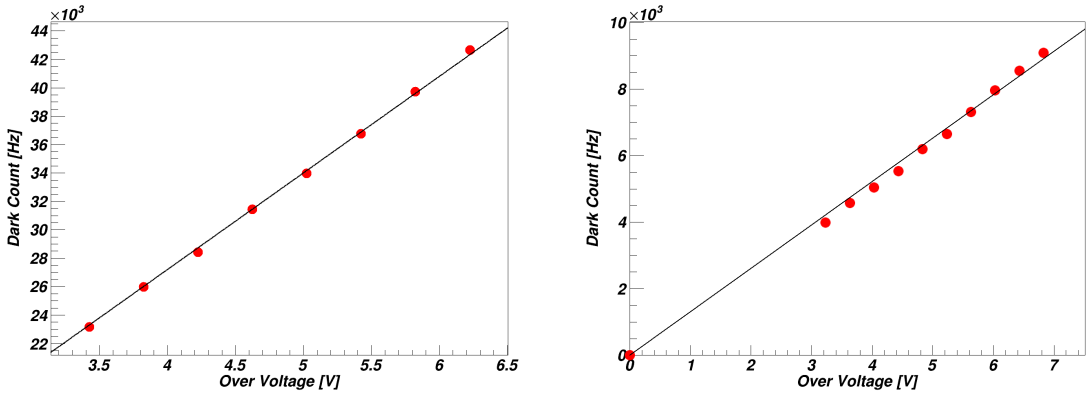

Figure 3.16: (Left) Over-voltage dependent DCR measurement at T = 245 K for the VUV3 $6 \times 6\,\mathrm{mm}^2$ SiPM and for the VUV4 SiPM of Type 10 at T = 270 K (Right).

Both the VUV3 and VUV4 SiPM of Type 10 show an exponentially decreasing dark count rate over a decreasing temperature. This is indicated in Figure 3.17. Due to the relative low dark count rate at lower temperatures, a statistical significant measurement at a temperature of T = 170 K was not possible in the first run. Thus, the DCR was primary extrapolated from the temperature-dependent DCR measurements (see Figure 3.17) at higher temperatures. Figure A.2 shows the extrapolated over-voltage-dependent DCR at T = 170 K for all three SiPM models. For consistency, a longterm dark count measurement of the $6 \times 6\,\mathrm{mm}^2$ SiPM at a temperature of T = 170 K and gain of 1.5×10^6 was performed during the longterm gain stability measurement (see Figure 3.9). A mean dark count rate of $R_{\mathrm{DC}} = 21\,\mathrm{Hz}$ for the $6 \times 6\,\mathrm{mm}^2$ SiPM was measured (see Figure 3.18). The long-term DCR measurement for the $6 \times 6\,\mathrm{mm}^2$ SiPM is in good agreement with the extrapolated dark count rate from the temperature-dependant DCR measurement.

SiPM Model	Dark Count Rate R_{DC} [Hz]		
	Gain 1.0 $\times 10^6$	**Gain** 1.5 $\times 10^6$	**Gain** 2.0 $\times 10^6$
Temperature T = 170 **K**			
VUV3 $6 \times 6\,\mathrm{mm}^2$	21.6	32.9	42.4
VUV4 Type 10	4.7	7.1	9.5
VUV4 Type 11	1.5	2.2	3.0
Temperature T = 270 **K**			
VUV3 $6 \times 6\,\mathrm{mm}^2$	3.0 $\times 10^5$	4.5 $\times 10^5$	5.6 $\times 10^5$
VUV4 Type 10	0.4 $\times 10^5$	0.5 $\times 10^5$	0.7 $\times 10^5$
VUV4 Type 11	0.3 $\times 10^5$	0.4$\times 10^5$	0.6 $\times 10^5$

Table 3.2: DCR at T = 170 K and T = 270 K for the $6 \times 6\,\mathrm{mm}^2$ VUV3 SiPM, VUV4 SiPM of Type 10 and the VUV4 SiPM of Type 11. The DCR value for the T = 170 K were extrapolated from the temperature-dependent DCR measurement.

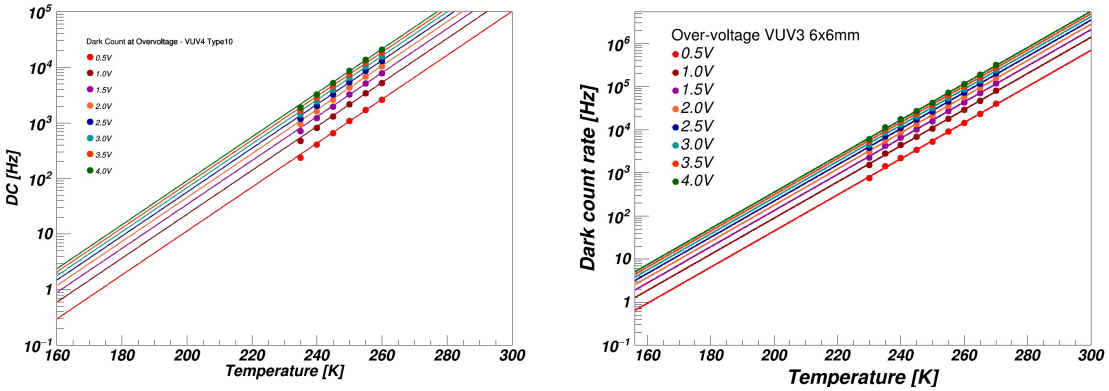

Figure 3.17: (Left) Temperature-dependent DCR for the VUV4 SiPM of Type 10 and (Right) for the VUV3 $6 \times 6\,\mathrm{mm}^2$ SiPM. Both DCR follow an exponential decrease over three orders of magnitudes.

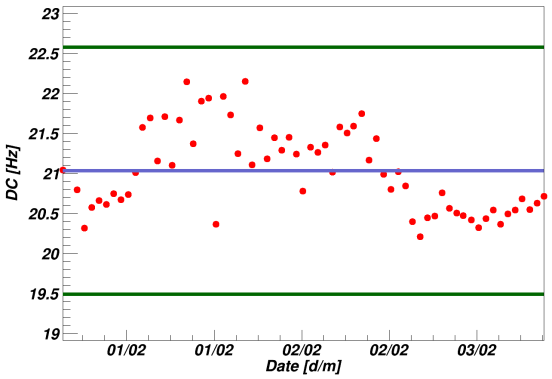

Figure 3.18: Long-term DCR measurement at T = 170 K for the VUV4 $6 \times 6\,\mathrm{mm}^2$ SiPM at a gain of 1.5 $\times 10^6$. The purple line shows the mean DCR and the green lines the 3 $\times$ RMS interval. The DCR fluctuation is less than 1% during the entire data-taking period.

3.5.2 Crosstalk

Optical crosstalk occurs when a breakdown in one pixel of the SiPM triggers an additional breakdown avalanche in a neighbouring cell of the silicon photomultiplier. During the primary avalanche process, initiated in the the active area of the SiPM, secondary photons can be generated and emitted and propagated to the neighbouring cell either by a direct path or by reflection on the silicon bulk of the SiPM, thus triggering a secondary avalanche. The secondary photons are emitted due to the acceleration of the charge carriers in the high electric field region. The secondary avalanches are almost simultaneously to the primary ones. A further contribution of crosstalk comes from the absorption of secondary emitted photons within the silicon substrate. The absorbed photon creates an electron-hole pair, where the created electron (or hole) can diffuse into a neighbouring cell and produce there a delayed signal avalanche. The delay of these crosstalk events is in the order of a few nanoseconds (see Figure 3.19).In order to reduce optical crosstalk and therefore improve the excellent photon counting resolution of a SiPM, one can consider the implementation of opaque trenches between the neighbouring cells. A sufficient amount of photons propagating on a direct path to the neighbouring cell can be absorbed and therefore reduces the optical crosstalk [70].

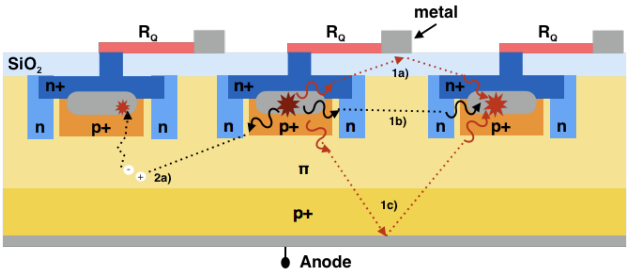

Figure 3.19: (Left) Conceptional structure of a silicon photomultiplier with three pixels. Crosstalk events occur when a secondary photon escapes the active area of a certain pixel during the avalanche process. These photons enter a neighbouring cell either by a direct path (1b) or by reflection on the upper SiO_2 layer (1a) or on the silicon substrate at the bottom (1c). A further mechanism of crosstalk comes from the production of a electron-hole pair in the surrounding silicon substrate (2a). The electron drifts into the active area of the neighbouring pixel initiating an avalanche in that pixel. When the created electron on the contrary drifts into the same pixel active area, it initiates an afterpulse event. Adapted from [68].

Crosstalk Analysis

For the measurement of the Crosstalk Rate (CTR) and Probability P_{CT}, the same experimental setup for the DCR measurement was used. The CT probability P_{CT} can be calculated from the DCR measurements performed in section 3.5.1:

$$P_{\mathrm{CT}} = \frac{\mathrm{DCR}_{1.5\mathrm{p.e.}}}{\mathrm{DCR}_{0.5\mathrm{p.e.}}}, \tag{3.11}$$

where $\mathrm{DCR}_{1.5p.e.}$ and $\mathrm{DCR}_{0.5p.e.}$ are the measured DCR at the discriminator threshold settings of 1.5 and 0.5 photo-electrons, respectively. Since the whole experiment was performed with the absence of light, the first signal corresponds to a dark count signal. All entries above the second threshold setting of 1.5 p.e. are considered to have more than 2 pixels simultaneously fired and may originate either from a random dark count event or a crosstalk. The probability for a second random dark count event to occur simultaneously is negligible. For demonstration purpose a simple calculation is performed. The pixel size of a VUV3 $6 \times 6\,\mathrm{mm}^2$ SiPM is $50\mu\mathrm{m} \times 50\mu\,\mathrm{m}$ and the dark count rate for the VUV3 $6 \times 6\,\mathrm{mm}^2$ SiPM at T = 170 K is $\sim 21\,\mathrm{Hz}$ (see Figure 3.18). This would results in a DCR per pixel of $R_{\mathrm{px}} = 1.5\,\mathrm{mHz}$. The accidental coincidence rate R_{E} for two pixels

firing due to two random dark count events within a coincidence time window of $\tau = 100\,\text{ns}$ can be calculated the following:

$$R_E = 2 \cdot R_{\text{px1}} \cdot R_{\text{px2}} \cdot \tau \tag{3.12}$$

The coincidence time window of $\tau = 100\,\text{ns}$ was chosen, since it is the time-resolution of a scaler. The accidental coincidence rate R_E is thus in the order of 4 $\times 10^{-13}\,\text{Hz}$. This is an upper limit calculation, since the fill factor of the VUV3 $6 \times 6\,\text{mm}^2$ SiPM was assumed to be 100%. Hence, all additional signals above the 1.5 p.e. threshold can be considered to be CT. Counting all events with the scaler in an interval of 1 second yields therefore the crosstalk rate.

Crosstalk Results

The crosstalk analysis procedure described above has been used to calculate the crosstalk probability P_{CT} for different over-voltages and temperatures. The CT probability was determined with equation 3.11 at different over-voltages in steps of 0.4 V. An example of the resulting CT probability for different over-voltages for the VUV3 $6 \times 6\,\text{mm}^2$ and the VUV4 SiPMs of Type 10 and 11 are shown in Figure 3.20.

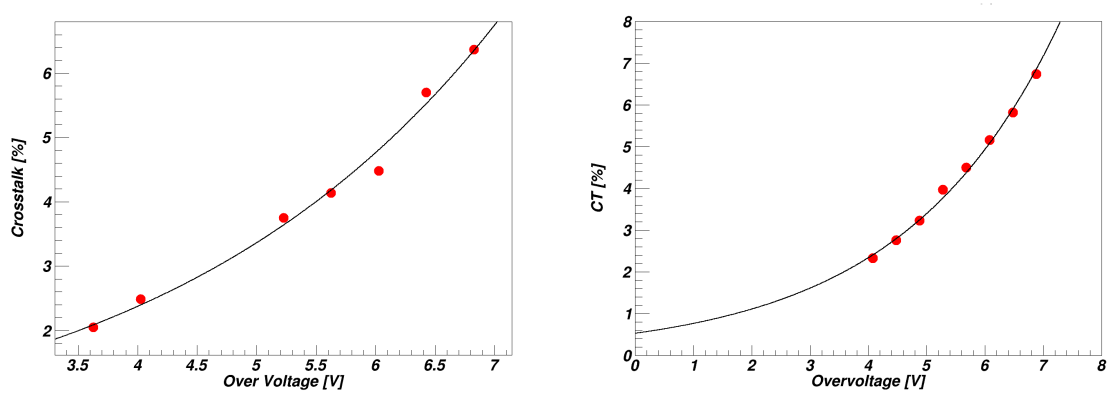

Figure 3.20: CT Probability in a function of over-voltage of the VUV3 $6 \times 6\,\text{mm}^2$ SiPM at T = 270 K (Left) and for the VUV4 SiPM of Type 10 at T = 270 K (Right). The red data points are fitted with an exponential function.

The resulting CT probabilities in a function of over-voltage at a certain temperature, as shown in Figure 3.20, have been fitted with an exponential function. The resulting fit function for every temperature has been used to calculate the CT probability for a certain over-voltage at a certain temperature. The calculation of the CT probability at different temperatures at various over-voltages was performed. (see Figures 3.21).

The crosstalk probability stays constant for different temperatures for all three tested SiPMs, but is growing exponentially with increasing over-voltages. This behaviour can be explained by the presence of higher electric fields in the depletion zone of the SiPM, when operated at high over-voltages. Since the gain increases with the over-voltage as well, the number of emitted photons and trapped charge carriers increase. This manifests itself in a strongly gain-dependent crosstalk probability. The crosstalk probability for all three SiPMs is in the same order, which confirms the equal pixel density of all three SiPMs provided by Hamamatsu. The crosstalk probability for temperatures at T = 170 K are shown in Figure 3.22 and Table 3.3. Theses values were extrapolated from higher temperature measurements (230 K - 270 K), since the dark count measurements and thus the crosstalk probability evaluation are too low for cryogenic temperatures.

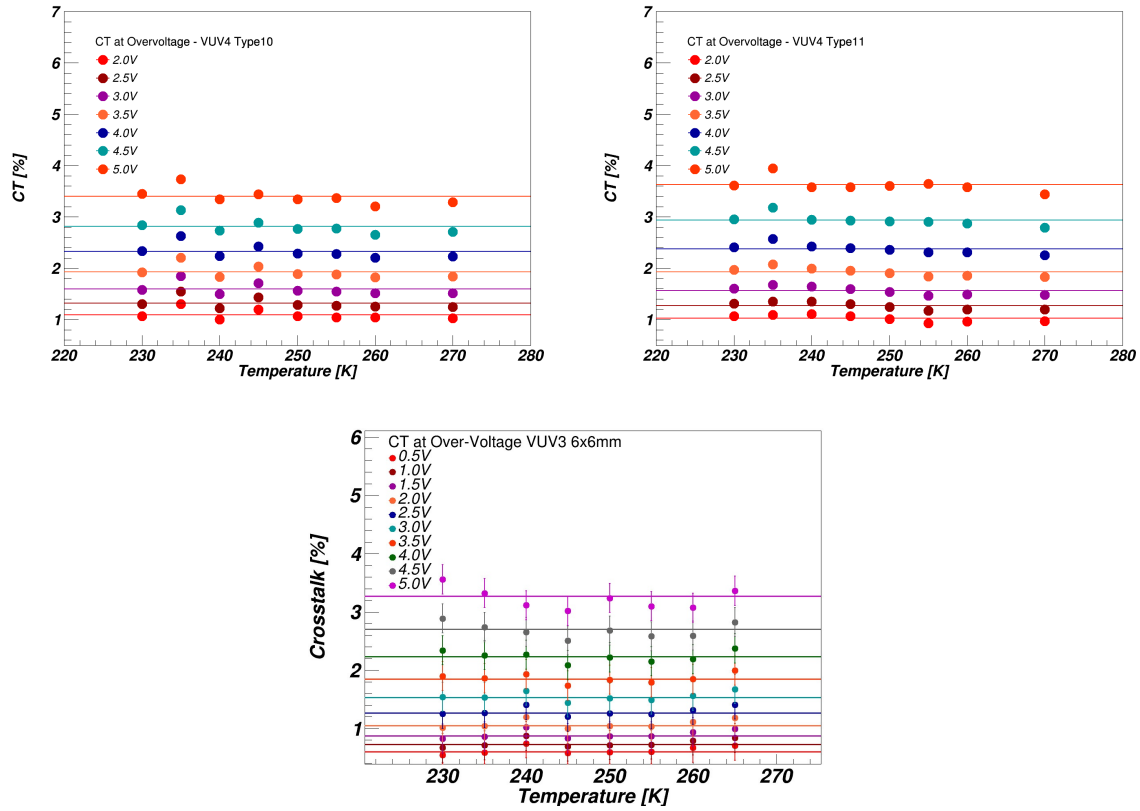

Figure 3.21: The temperature-dependent CT probability for different over-voltages of the VUV4 SiPM of Type 10 (top, left) and Type 11 (top, right) and for the VUV3 $6 \times 6\,\mathrm{mm}^2$ SiPM (Bottom). The CT probability is for all three SiPM models constant over temperature.

SiPM Model	**Crosstalk Probability** [%]		
	Gain 1.0 $\times 10^6$	**Gain** 1.5 $\times 10^6$	**Gain** 2.0 $\times 10^6$
Temperature T = 170 **K**			
VUV3 $6 \times 6\,\mathrm{mm}^2$	2.7	6.9	17.1
VUV4 Type 10	1.5	2.5	4.3
VUV4 Type 11	1.3	2.3	4.0

Table 3.3: Crosstalk probability results at T = 170 K for the $6 \times 6\,\mathrm{mm}^2$ VUV3 SiPM, VUV4 SiPM of Type 10 and the VUV4 SiPM of Type 11.

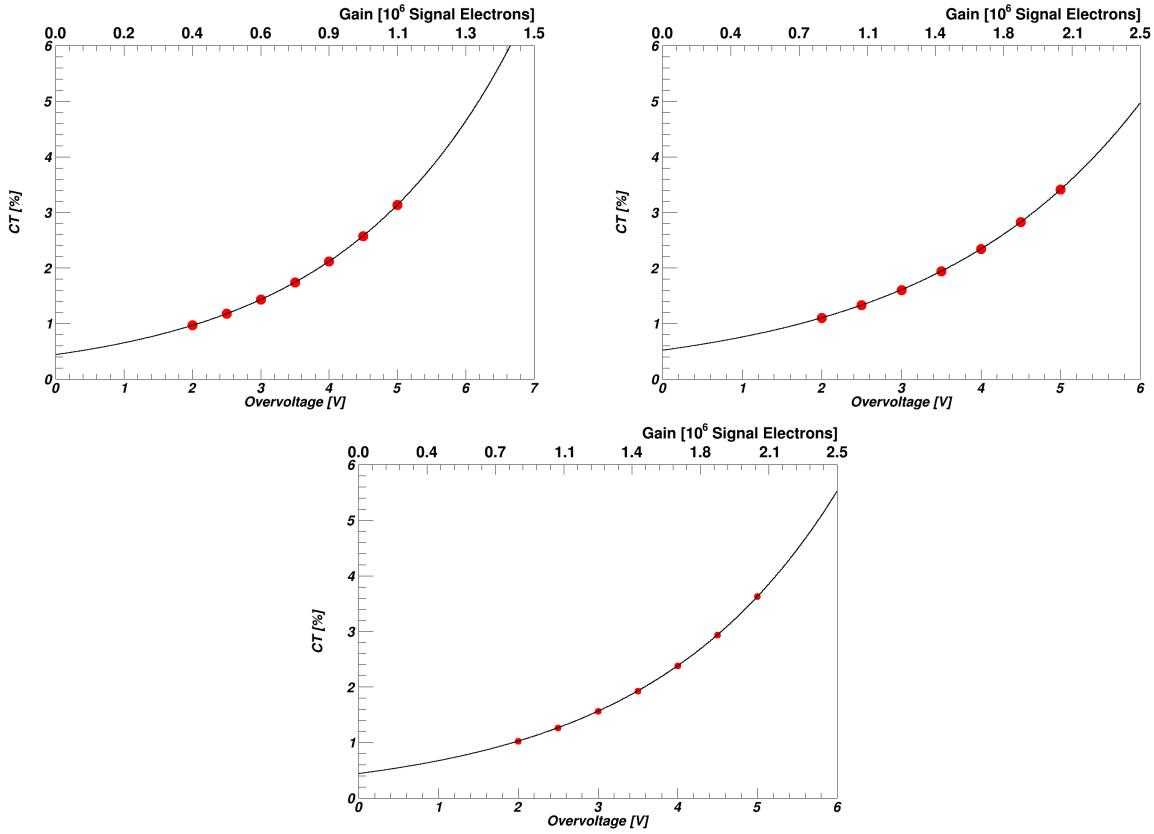

Figure 3.22: The crosstalk probability for different over-voltages for the VUV3 $6 \times 6\,\mathrm{mm}^2$ (Left) the VUV4 SiPM of Type 10 (Right) and Type 11 (Bottom) for a temperature of $\mathrm{T} = 170\,\mathrm{K}$. These values are extrapolated from the fitted exponential function of measurements performed at higher temperatures.

3.5.3 Afterpulse Studies

A further contribution to the correlated noise comes from afterpulses, which originate due to traps created by impurities in the silicon substrate. When charge carriers are created during the avalanche process - primary initiated by an absorption of a photon in a pixel - there is a finite probability for these carrier to be trapped in specific impurity. These trapped charge carrier have energies of the order of the band gap and can be released later with a characteristic time constant. The released free charier has enough energy to induce a further breakdown in the pixel before the initial pixel is fully recharged to the bias voltage. This results in an additional delayed signal, which is characterised by a lower charge output than the gain of the pixel [71, 72].
The probability $P_{\mathrm{AP}}(t)$ for an afterpulse signal to occur can be described by the following approach:

$$P_{\mathrm{AP}}(t) = P_{\mathrm{trap}} \cdot \frac{exp(-t/\tau_{\mathrm{trap}})}{\tau_{\mathrm{trap}}} \cdot P_{\mathrm{trigger}} \quad , \tag{3.13}$$

where the time-dependent afterpulse probability $P_{\mathrm{AP}}(t)$ is dependant on the trap capture probability P_{trap}, the trap lifetime τ_{trap} and the avalanche triggering probability P_{trigger} [72]. The trap capture probability P_{trap} is highly dependent on the density of impurities in the silicon substrate and the carrier flux during the avalanche, which increases with higher gains. In order to reduce the afterpulse probability drastically, an improvement in the manufacturing of SiPM with a higher purity level of silicon has to be taken into account.

Since the gain increases with the size of the SiPM, higher afterpulse rates are expected with larger detector sizes. Therefore the size of the SiPM is limited to a specific size, since the afterpulse and optical crosstalk rates would dominate, contributing to high background signals when measuring scintillation photons. Furthermore the trap lifetime τ_{trap} depends on the energy level of the trap within the band gap and the lattice temperature. So performing measurements at lower temperatures decreases the afterpulse rate substantially. The avalanche trigger probability P_{trigger} increases with higher electric fields in the active area, thus increasing the afterpulse rate at higher over-voltages and higher gains.

Afterpulse Analysis

Since an afterpulse signal is delayed by a few nanoseconds with respect to the primary signal, the waveform has a characteristic peak during the recovery of the pixel. The amplitude of this afterpulse signal is smaller than the original pulse height. Due to the small time delay of this secondary peak the processor is not able to distinguish these two peaks and integrates therefore over the whole range of the signal. Thus the deposited charge is higher than a normal 1p.e. signal. Taking this fact into account, a quantitative method was developed to estimate the afterpulse contribution [60]. Since the 1 pe. signals have a distinct pulse height distribution, one can plot the pulse height over the acquired charge area of the signal (see Figure 3.24). One expects a distinct Gaussian distributed 1 p.e. population with afterpulse events being shifted to increased pulse heights with higher charge depositions. The 1p.e. population was fitted with a two dimensional elliptical Gaussian distribution of the form:

$$f(x,y) = A \times exp\left[-\left(a(x-x_0)^2 + 2b(x-x_0)(y-y_0) + c(y-y_0)^2 \right) \right], \tag{3.14}$$

with the coefficients a, b, c having the form of:

$$a = \frac{cos^2(\theta)}{2\sigma_x^2} + \frac{sin^2(\theta)}{2\sigma_y^2} \qquad b = -\frac{sin(2\theta)}{4\sigma_x^2} + \frac{sin(2\theta)}{4\sigma_y^2} \qquad c = \frac{sin^2(\theta)}{2\sigma_x^2} + \frac{cos^2(\theta)}{2\sigma_y^2}$$

The elliptical Gaussian can be rotated clockwise with an angle θ. The x_0, y_0 coefficients correspond to the mean height and integrated charge respectively and A is the amplitude. σ_x^2 and σ_y^2 are the standard deviations of the Gaussian distributions and θ gives the angle with which the ellipse is titled in the x-y plane. The elliptical contour of the fit is constrained by the following cut

$$\frac{(x \cdot cos\theta - y \cdot sin\theta)^2}{a^2} + \frac{(x \cdot sin\theta + y \cdot cos\theta)^2}{b^2} < 1, \tag{3.15}$$

where a is the major axis and b the minor axis. All the events within the 3σ contour belong to the 1 p.e. population, whereas other events are considered to be afterpulse events. The afterpulse contribution can be calculated by taking the ratio of the afterpulse events N_{AP} over the number of primary 1 p.e. events N_{1pe}.

$$P_{AP} = \frac{N_{\text{AP}}}{N_{\text{1pe}}} \tag{3.16}$$

Afterpulse Results

The afterpulse calculation described above was performed for both the VUV3 and VUV4 of the type 10 and 11 SiPM at a temperature of 170K. The AP contribution was calculated for lower overvoltage with a stepwise increase of 0.4V and was fitted with an exponential function. The fitted

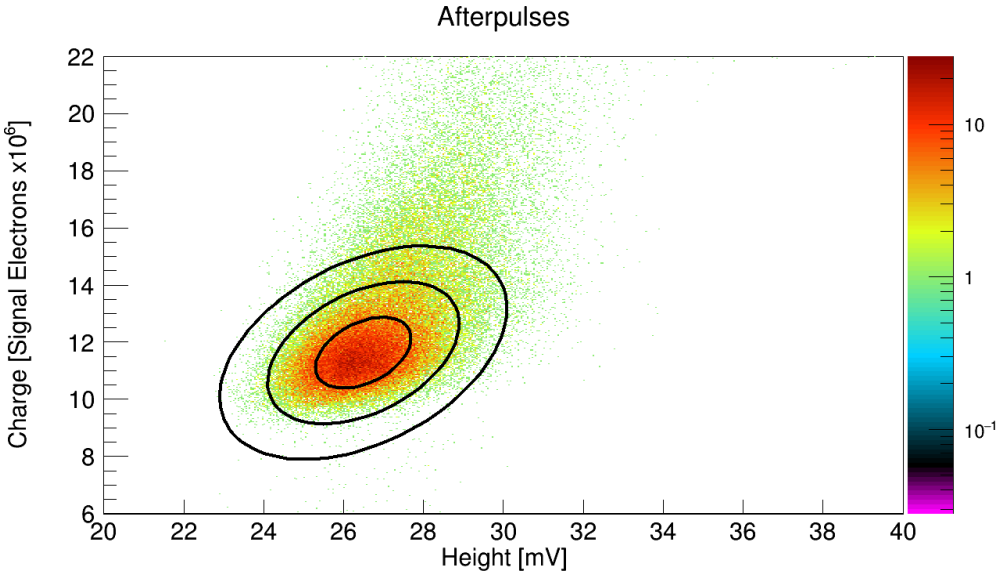

Figure 3.23: Example of an afterpulse calculation procedure for data taken at T = 170 K and at an over-voltage of V=10.6 V for the VUV3 $6 \times 6\,\mathrm{mm}^2$ SiPM. The black ellipse define the 1σ, 2σ and 3σ confidence levels. Events within the 3σ ellipse are considered as 1 p.e. events, whereas the outer events are afterpulse events.

exponential function was used to extrapolate the AP contributions at higher gains (G$\geq 2.0 \times 10^6$) and higher over-voltages.

The measured AP rates for all three SiPM are shown in Table 3.4. The AP rates for the VUV3 6x6mm SiPM for gains of 2.0×10^6 and 2.5×10^6 are determined by the extrapolation of the fitted function from lower over-voltage measurements. It is cleary seen that at higher gains the AP rate exceeds over 100%, which indicates, that the extrapolation is not a good approach to estimate the AP rates at high gains. In order to make good afterpulse rate estimations at higher gains, meaurements at over-voltage above 9V have to be performed. For lower over-voltages acceptable AP rates were measured for both the VUV3 and VUV4 SiPM of Type 10 and 11. Table 3.4 shows lower AP rates for the VUV4 SiPM, which is due to the smaller active area of these photomultipliers. The AP rate per unit area is in the same order for all three tested SiPM.

SiPM Model	**Afterpulse Probability [%]**		
	Gain 1.0 $\times 10^6$	**Gain** 1.5 $\times 10^6$	**Gain** 2.0 $\times 10^6$
Temperature T = 170 **K**			
VUV3 $6 \times 6\,\mathrm{mm}^2$	13.33	39.33	116.30
VUV4 Type 10	4.87	9.4	18.12
VUV4 Type 11	3.52	6.39	11.60

Table 3.4: Afterpulse contributions for VUV3 and VUV4 at T = 170 K.

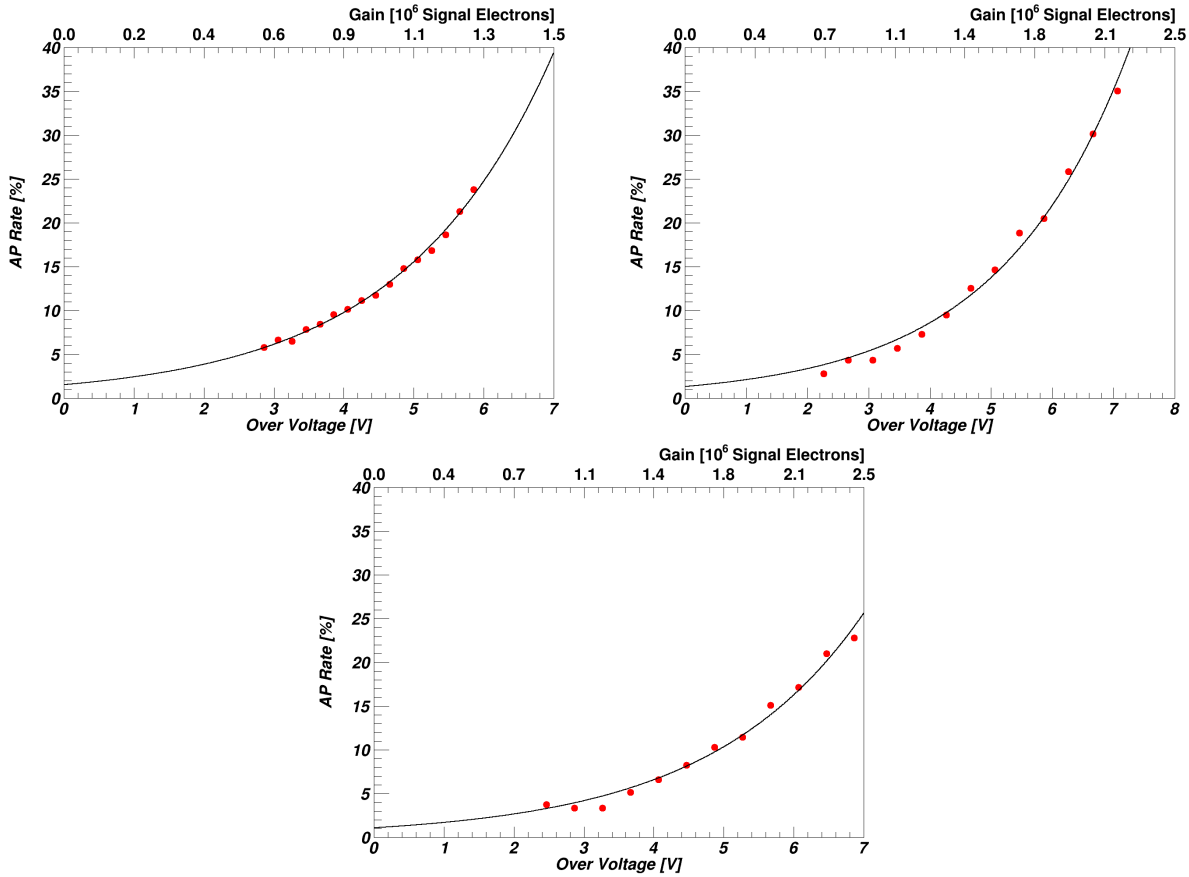

Figure 3.24: Afterpulse contributions for the VUV3 $6 \times 6\,\mathrm{mm}^2$ SiPM (top, left) the VUV4 of Type 10 (top, right) and the VUV4 of Type 11 (Bottom). All SiPM show an exponentially increasing AP rate with the applied over-voltages.

3.6 SiPM Requirments for Large-Scale Dark Matter Detectors

For a potential incorporation of Silicon Photomultipliers in future large scale dual-phase xenon TPCs like DARWIN, a full characterisation of viable SiPMs need to be performed and additionally several crucial requirements need to be fulfilled and considered. SiPMs are very promising new solid-state based photo-detectors, which are considered to replace former photomultiplier tubes (PMT) used in current xenon-based dual-phase TPCs like XENON1T. SiPMs have higher sensitivities and superior timing performances compared to other solid state photo-detectors like APDs and PIN diodes.

Physical Differences: The technology of silicon-based sensors - in particular SiPM - experienced a huge leap in current years and are today able to compete directly with the vacuum-based photomultiplier tubes (PMT) due to their intrinsic advantages of being more compact, rugged, and insensitive to magnetic fields. They possess an excellent timing resolution of $\sim 120\,\mathrm{ps}$ for single photoelectron detection, fast risetime (sub-ns), good dynamic range in the order of $\sim 10^3/\mathrm{mm}^2$ and are not highly affected by radiation damage [73]. In comparison to PMTs used in xenon based TPCs, SiPMs can not be affected by leaks and could therefore be operated without any failures. Since SiPMs are operated comparatively to PMTs ($\sim 1.5\,\mathrm{kV}$ - $2\,\mathrm{kV}$) at lower voltages ($50\,\mathrm{V}$ - $100\,\mathrm{V}$), the signal readout boards are considerably smaller and less complex in their setup. The need for less electronic components reduce further the radioactivity contributions and thus the background contributions. These physical features make the SiPM a viable candidate for implementation in large scale xenon detectors such as DARWIN.

Gain: Both PMTs and SiPMs are able to achieve high gains in the order of $10^5 - 10^7$ and are capable of single photo-electron detection. The gain of a SiPM increases linearly with the over-voltage (see section 3.4), whereas the gain of a PMT follows a power law. A 3-inch PMT operated at 1500 V shows a gain of 5.4×10^6 [74], which can be increased by a factor of 1000 by a relative low operation voltage increase. For the SiPM on contrary, a gain of 1.5×10^6 is achieved at an operation voltage of 52 V and a higher gain can be achieved by a small change of the over-voltage V_{OV}. A gain of 1.5×10^6 for the VUV3 $6 \times 6\,\mathrm{mm}^2$ SiPM is achieved at an over-voltage $V_{\mathrm{OV}} = 7.0\,\mathrm{V}$ and a gain of 3.0×10^6 equals to an applied over-voltage of $V_{\mathrm{OV}} = 14.0\,\mathrm{V}$ at $\mathrm{T} = 170\,\mathrm{K}$.

The single photo-electron spectrum of a 3-inch PMT shows a non-Gaussian shape [74]. The non-Gaussian part can be explained by the so-called under-amplified electrons, which are not participating in the entire amplification chain of the PMT. This results in a reduced 1 p.e. resolution $\sim 27\,\%$ at a gain of $3{\times}10^6$ [74]. The SiPM in contrast does not show this feature and shows a Gaussian distributed SPE spectrum (see section 3.4 for the VUV3 $6 \times 6\,\mathrm{mm}^2$ SiPM) and thus a higher single photon acceptance can be achieved.

PDF efficiency: In order to achieve high sensitivities for dark matter interactions a high photon detection efficiency at a wavelength of 178 nm is required. For PMTs the photon detection efficiency can be expressed with the quantum efficiency (QE) and is thus an essential characteristic property of the photosensor. The quantum efficiency of a PMT does not only depend on the glass material through which the photons need to traverse to reach the photocathode, but as well as the material used for the photocathode itself. The quantum efficiency does not depend on the applied voltage. For the 3-inch PMT used in XENON1T a quantum efficiency of 32.5% at a wavelength of $\lambda = 175\,\mathrm{nm}$ at an operation temperature of T= 170K was measured [74]. In contrast, the photon detection efficiency η of a SiPM is dependent of the fill factor ϵ and the quantum efficiency QE. The fill factor is a geometrical factor and does not depend on either the wavelength nor the applied operation voltage and is thus a constant for each SiPM. The QE-value for SiPM are highly wavelength dependent. The VUV3 $6 \times 6\,\mathrm{mm}^2$ has a photon detection efficiency in the range of $20\,\%$ - $25\,\%$ for a sensitive wavelength of $\lambda = 175\,\mathrm{nm}$ at room temperature [75]. The photon detection efficiency at room temperature

for a VUV-sensitive SiPM is therefore in the same order of magnitude as for PMTs currently used in the XENON1T experiment at a temperature of T = 170 K. In conclusion further temperature and voltage-dependent PDE measurements still need to be performed to make a viable statement.

Accidental Coincidence The high DCR for SiPMs are still a major disadvantage for a potential use in large-scale detectors. The VUV3 $6 \times 6\,\mathrm{mm}^2$ SiPM shows a DCR of $R_{\mathrm{DC}} \approx 0.6\,\mathrm{Hz/mm}^2$ at a gain of 1.5×10^6 and at a temperature of T = 170 K, thus accidental event coincidence is not negligible. An accidental event coincidence occurs when two events happen simultaneously or within an acceptable delay time interval, but are causally unrelated. Thus in context to a TPC detector system, a lone S1 & S2 event are randomly produced within a time interval, which would mimic a true event induced by an incident particle. The lone S1 events can be generated by dark count events within the SiPM in the photon detection array, whereas lone S2 events can be generated by photons produced by delayed extracted electrons in the upper region of the TPC. The accidental event coincidence R_E can be calculated with the following formula:

$$R_E = 2 \cdot R_{S1} \cdot R_{S2} \cdot t \quad , \tag{3.17}$$

where R_{S1}, R_{S2} are the lone S1 & S2 rates, t the coincidence time interval, which is maximal the travel time of the ionization electrons in the electric field of the the entire TPC. For an overall estimate of the extent of accidental event coincidence, the lone S1 and S2 accidental coincidence rates R_{S1} and R_{S2} and the electron drift time t_{drift} need to be calculated, respectively estimated. For the evaluation of the drift time t_{drift} the electric drift field needs to be known. The DARWIN experiment is planned to operate at an electric drift field of $\sim 0.5\,\mathrm{kV/cm}$ [46], which would result with a corresponding drift velocity $v_{\mathrm{drift}} \sim 2\,\mathrm{mm}/\mu\mathrm{s}$ [74] and drift length of z = 2.6 m [46] to a drift time $t_{\mathrm{drift}} = 1300\,\mu\mathrm{s}$.

lone S1 Rate estimation: The accidental coincidence rate of the lone S1 signal is induced by random dark count event of the VUV3 $6 \times 6\,\mathrm{mm}^2$ SiPM and is dependent on how many independent SiPM units are used in the entire detector system and how many of them need to be triggered within an acceptable time window to account for a lone S1 event. This accidental lone S1 coincidence rate can be calculated with the following formula:

$$R_{M-n} = \binom{M}{n} \cdot R_{DC}^{n} \cdot \tau^{n-1} \quad , \tag{3.18}$$

where M is the total amount of used SiPMs in the detector, n the degree of accidental coincidence, R_{DC} the DCR of an individual SiPM unit and τ the coincidence time window [76].

To make a first upper estimate of the extent of accident coincidence rates a few parameter assumptions need to be done. The DCR from the VUV3 $6 \times 6\,\mathrm{mm}^2$ SiPM characterization in section 3.5.1 of $R_{DC} = 21\,\mathrm{Hz}$ at a gain of 1.5×10^6 at a temperature of T = 170 K was used. Further a coincidence time window of $\tau = 10\,\mathrm{ns}$ was assumed. The DARWIN experiment is planned to incorporate $\sim$1800 3-inch or $\sim$1000 4-inch PMTs [46]. In order to implement SiPMs for both the bottom and top detection array of the TPC, the same area coverage of the planned $\sim$1800 3-inch PMTs is assumed. This would result in a total of 228000 potential VUV3 $6 \times 6\,\mathrm{mm}^2$ SiPMs installed in the DARWIN experiment.

Table (3.5) shows the upper limit calculations for different degrees of accidental coincidences with equation 3.18. Compared to currently used 3-inch Hamamatsu R11410-21 photomultipliers [74] in XENON1T, the $6 \times 6\,\mathrm{mm}^2$ SiPM lone S1 rate for a 3-fold accidental coincidence is in the order of $\sim$6 higher. For the calculation of the 3-fold accidental coincidencte for the

3-inch PMTs, the same coincidence time window $\tau = 10\,\text{ns}$ was assumed and a DCR of 40 Hz [74] was used.

S1 lone rate R_{S1} induced by DC		
	$6 \times 6\,\text{mm}^2$ SiPM	**3-inch PMT**
3-fold Coincidence	1.8 kHz	6 mHz
4-fold Coincidence	21 Hz	-
5-fold Coincidence	200 mHz	-
6-fold Coincidence	1.6 mHz	-
7-fold Coincidence	11 μHz	-

Table 3.5: This table shows the upper limit calculations for various degrees of accidental coincidences for the VUV3 $6 \times 6\,\text{mm}^2$ SiPM. The lone S1 rate R_{S1} is induced by dark count events ($R_{DC} = 21\,\text{Hz}$ at $T = 170\,\text{K}$). The 3-inch PMT used in the XENON1T experiment is listed as a reference.

The calculated accidental event coincidence with formula (3.18) are shown in Table (3.6). In order to have an accidental event coincidence rate R_E of the SiPM in the same order of magnitude as for 3-inch PMT (3-fold coincidence), a preliminary 6-fold coincidence for the S1 is required. This would then shift the detector threshold to 6 p.e. and the energy threshold too higher values. In comparison the 3-inch PMTs at XENON1T have a 3 p.e. detector threshold. The DCR for SiPMs are thus currently to high for a potential implementation in large scale detector systems. In order for SiPMs to be a viable competitor to the vacuum-based PMTs the DCR needs to be significantly reduced.

Event Rate Comparison $6 \times 6\,\text{mm}^2$ SiPM			
S2 lone Rate R_{lone}	**3-fold Coincidence**	**4-fold Coincidence**	**5-fold Coincidence**
0.1 Hz	0.5 Hz	6 mHz	55 μHz
1.0 Hz	5 Hz	57 mHz	545 μHz
10 Hz	48 Hz	569 mHz	5.5 mHz

Table 3.6: This table shows the calculated accidental event coincidence for different assumptions on the S2 lone rate R_{lone} and the degree of the S1 accidental coincidence.

CHAPTER 4

Light Collection Efficiency Simulation

This chapter is dedicated to the Light Collection Efficiency simulation performed for the Xurich-II dual-phase Time Projection Chamber (TPC) detector. The detector was developed at the University of Zurich for R&D purposes for xenon-based TPC detectors. While the first section (4.1) will focus on the the Xurich-II detector, the second section 4.2 covers the essential part of this thesis - The Light Collection Efficiency Simulation for the Xurich-II TPC detector with a newly developed SiPM top array.

4.1 Xurich-II TPC detector

The Xurich-II detector is composed of a small dual-phase TPC based on liquid and gaseous xenon as the inner part of the detector. Further it consists of a cooling and liquification system, which sustains the core temperature and chemically purifies the xenon through recirculation in the gas phase. The active area of the TPC consists of a cylindrical chamber with a diameter of 31 mm and a height of 31 mm, which is placed inside a stainless steel cryostat with a diameter of 83.7 mm. The slightly larger cryostat minimizes the required amount of xenon and therefore reduces potential neutron scatterings before reaching the drift chamber [77].

With the assumption of the liquid xenon density of $2.92\,\mathrm{g/cm^3}$ the active area contains 68 g of xenon. The inside of the cylindrical chamber is covered with a PTFE insulator, which maximizes the light collection efficiency. The gate and the cathode electrodes, which is situated at the bottom of the TPC, are vertically separated by 30.5 mm and are both placed in liquid xenon. The grounded gate mesh is situated only a few mm below the liquid xenon surface. The placement of the two electrodes limit the drift velocity of the ionization electrons produced by an incident particle. The anode on the contrary is placed above the gate in the gaseous xenon part of the TPC and is vertically displace to the gate by 4 mm. All three electrodes are composed by a 0.1 mm thick stainless steel mesh with a hexagonal pattern. The hexagonal pattern was realized by chemical etching and each hexagon opening has a width of 2.7 mm. This structure results in a geometrical transparency of 93 % [78]. In order to sustain a uniform electric field within the detector, the electrode meshes are horizontally displaced to each other, such that the center of the hexagon of the gate mesh is horizontally aligned with the vertices of the hexagons of the anode and cathode. Further cooper field shaping rings, which are separated and insulated by PTFE spacers, are installed around the active detector area in order to sustain a uniform electric field. Since the detector is operated at liquid xenon temperature, the electrode meshes are confronted with a lot of stress during the cooling period. In order to prevent the bending, breaking and displacement of the delicate meshes, the anode and gate meshes are surrounded by an additional stabilizer ring, which is horizontally mounted with PEEK screws into the outer stabilizing structure. Torlon was used for the electrical insulation of the gate and anode mesh, since it has a similar thermal expansion coefficient like the adjacent stainless steel cryostat. The torlon structure facing the inner part of the detector is further covered with PTFE in order to maximize the light collection efficiency. For the detection of photons two

cylindrical 2-inch Hamamatsu-R9869 PMTs with a 16 cm^2 synthetic silica window are used and are placed in a PTFE holder. For a potential upgrade of the Xurich-II detector the upper PMT can be exchanged with an appropriate designed SiPM array. The design of the TPC allows operations of a bias voltage ΔV between the cathode and the gate from $\sim 500\,V$ to $\sim 9\,kV$, which corresponds to an electric field of $\sim 0.170\,kV/cm$ and respectively $\sim 9\,kV/cm$ [77, 79].

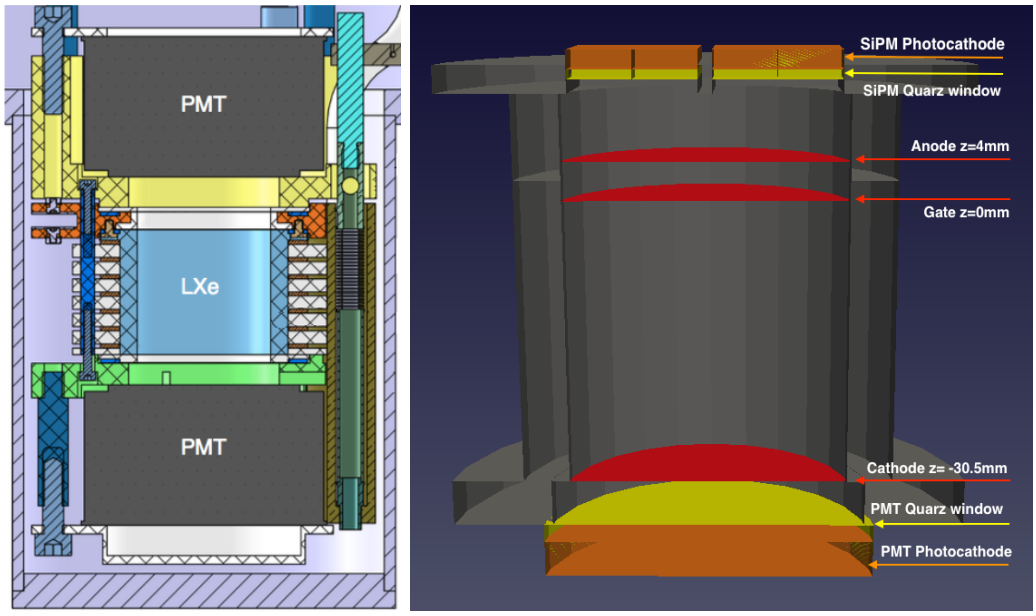

Figure 4.1: (Left) shows the the interior of the Xurich-II detector containing a total of two PMTs - one placed at the top and bottom. (Right) The Xurich-II TPC geometry in the GEANT4 framework. The three electrodes are highlighted in red. The gate is positioned at $z = 0\,mm$, whereas the anode is located at $z = 4\,mm$ and the cathode at $z = -30.5\,mm$. The photosensitive areas of the photocathodes are indicated in orange and the yellow segments are the quarz windows of the respective photocathodes. Left picture taken from [78].

4.1.1 Top Array with SiPM

A potential upgrade for the Xurich-II TPC is the replacement of the top 2-inch Hamamatsu-R9869 PMT with four VUV3 $12 \times 12\,mm^2$ Hamamatsu-S13371 SiPMs. Such an upgrade would improve the detectors ability to reconstruct the xy-position of the interaction vertex from the S2 signal. In order to realise such an upgrade a primary light collection efficiency (LCE) simulation with the newly designed top SiPM array was performed. The simulation was performed within the GEANT4 framework, which was also used to perform previous simulations with the original settings of the detector. Figure 4.2 shows the top SiPM array incorporating four VUV3 $12 \times 12\,mm^2$ Hamamatsu-S13371 SiPMs, which was used for the LCE simulation. Since an individual VUV3 $12 \times 12\,mm^2$ SiPM consists of four identical segments, which can either be read out individually or collectively, two different top SiPM arrays were simulated in the GEANT4 framework. The first SiPM top array, denoted as configuration A, consists of four segments with a dimension of $12 \times 12\,mm^2$. Each $12 \times 12\,mm^2$ SiPM will be readout in series. For the second SiPM top array each individual $12 \times 12\,mm^2$ SiPM is subdivided into four equally sized segments, which will result in a total of 16 individually readout segments. This SiPM top array will be denoted for future references as configuration B. The idea is to analyse the impact of different readout approaches on the total light collection efficiency and especially on the position reconstruction of the S2 signal. Since the second top array consist of more segmentations a better position resolution is expected. All four SiPM are symmetrically aligned and cover the original spacing of the PMT. The total height of the SiPM is 3 cm, where the photosensitive part is 2 cm and the remaining part is the 1 cm thick quartz

window. This SiPM geometry was incorporated in the GEANT4 simuluation code as well, in order to account for different reflection indices of the used materials.

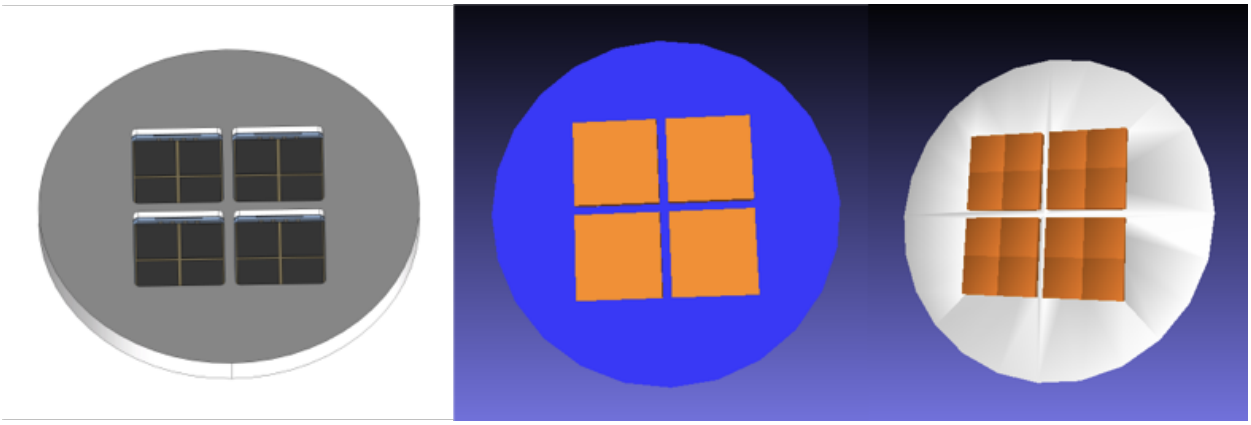

Figure 4.2: (Left) CAD sketch of the SiPM top array for the Xurich-II TPC containing four VUV3 $12 \times 12\,\mathrm{mm}^2$ Hamamatsu-S13371 SiPMs. Each SiPM is subdivided into four equally sized segments, which can either be read out in parallel or in series. (Middle) The first top array within the GEANT4 framework, where all segments of a single SiPM are read out in series (orange). (Right) Top array with a total of 16 segmentations designed in GEANT4. All segments of a single SiPM are readout individually - respectively in parallel.

4.2 Light Collection Efficiency

An essential part of operating a xenon-based dual-phase TPC detector is to efficiently detect all the scintillation photons of low energetic nuclear recoil events. Since WIMP scatterings with the xenon atoms are associated to a low energetic nuclear recoil events and the event rates are very low, it is important to optimize the reflectivity of the detector and improve the detection ability of the photosensors in the top and bottom array of the TPC. In order to take into account the geometry of the detector, the effect of the used target and detector materials and the geometry of the photosensor array consisting of PMTs and SiPMs, a light collection efficiency simulation needs to be performed. The light collection efficiency (LCE) is defined as the ratio of the detected number of photons over the total amount of generated photons due to an initial event:

$$\mathrm{LCE} = \frac{\#\text{detected photons}}{\#\text{generated photons}} \tag{4.1}$$

For the upgrade of the Xurich-II experiment a light collection efficiency simulation was performed for the two different type of top array (configuration A and B) consisting of SiPMs. The simulation in the GEANT4 framework not only considers the geometry of the detector, but also its compounds and the physical processes while interacting with different parts of the detector. The entire detector is created within a simulation world which is by default in vacuum. The distinct components, which make up the entire detector, can be gradually implemented into the simulation world. The geometrical shape and the material composition properties can be assigned to the specific detector volumes. While setting the geometry of the detector in GEANT4, one has to define which volumes of the detector are sensitive to particle interactions and define their possible physical interactions. In the simulation the following properties were taken into consideration:

PTFE: Polytetrafluoroethylene - PTFE - is used in detectors for their many advantageous properties at low temperatures. It is known for its high reflectivity, which is why it is commonly used as a reflector material within the detector and therefore improves the light collection

efficiency of scintillation photons in liquid xenon. Performing experiments at cryogenic temperature demand further essential properties of the used reflection material. PTFE remains its high strength and toughness at low temperatures up to 5K and maintains its good reflectance at even thin thicknesses. These properties make it an instrumental material for low temperature direct dark matter experiments [80].

For the simulation of the scintillation light signal S1 in the liquid xenon target area, a PTFE reflectivity of 95 % was used. The determination of the reflectivity parameter accounts for the possible absorption of the scintilation light in the PTFE wall. The reflectivity in gaseous xenon on the contrary could be 10 % to 25 % less than in liquid xenon, but affects the light collection efficiency of the S1 signal only to a small degree [81]. This affect is due to the higher refractive index of liquid xenon compared to the gaseous xenon. Only a small amount of photons will enter the gas phase due to total internal reflection at the gas-liquid level. Hence, a lower reflectivity in gaseous xenon can be afforded for. For the S2 signal light collection efficiency simulation a PTFE reflectivity of 90 % was used [78].

Rayleigh Scattering λ_{Ray}: When photons travel through a medium such as xenon, they scatter. Thus, the direction and the travel distance increase before the photon finally reaches the PMT or SiPM. The Rayleigh scattering length λ_{Ray} is inversely proportional to the fourth power of the wavelength. For xenon scintillation light the Rayleigh scatting effect is therefore crucial and may even influence the design of the detector. For the simulation a Rayleigh scattering length in liquid and gaseous xenon of $\lambda_{\mathrm{Ray,GXe}} = \lambda_{\mathrm{Ray,LXe}} = 100\,\mathrm{cm}$ were used [78].

Absorption Length λ_{abs}: The probability for a particle travelling in a specific medium and not being absorbed drops to 1/e at an absorption length λ_{abs}. Main impurity contributions from O_2 and H_2O as well as CO_2, N_2 and CH_4 down to the ppb (part-per-billion) level in the detector material can affect the absorption length and therefore decrease the light collection efficiency of the detector. With an additional purification system these specific impurities can be minimized. For the light collection efficiency simulation of the Xurich-II detector an absorption length for liquid and gaseous xenon $\lambda_{\mathrm{LXe}} = \lambda_{\mathrm{GXe}} = 50\,\mathrm{m}$ was used [78]. Within the dimensions of the detector the xenon detector material is transparent for the scintillation light with a wavelength of λ =178 nm.

Electrodes & Gate Transparency: The real physical hexagonal shape of the three electrode mashes are not implemented, but instead are encoded with a 0.1 mm thick stainless steel disk with a corresponding transparency of 93 %. To establish the specific geometrical transparency of 93 %, the absorption length for the electrode meshes was set to 1.38 mm. This setting results in the desired absorption probability of 7 %. In order to avoid additional refraction of the photons at the three electrodes, the refractive indices for the gate (n_{G}), anode (n_{A}) and cathode mesh (n_{C}) are matched with their surrounding materials. In particular, the refractive index of the anode mesh is equal to the gaseous xenon one ($n_{\mathrm{GXe}} = 1.0$), whereas the refractive indices of the gate and the cathode mesh are matched to the refractive index of liquid xenon ($n_{\mathrm{LXe}} = 1.63$). With this procedure the meshes are "invisble" for the incoming photons generated during the simulation.

Optical Properties: The propagating scintillation light in the TPC is exposed to different material surfaces and hence can reflect or refract due to transmissions to a different medium. Possible transitions of the scintillation light to adjacent materials have to be account for in the simulation. Possible material cross-overs include the transition from liquid to gaseous xenon at the gas-liquid level, liquid and gaseous xenon to the PTFE walls of the TPC, liquid xenon to the synthetic silica of the bottom PMT and gaseous xenon to the SiPMs in the top array of the TPC, respectively. The individual refraction indices used for the simulation are listed in Table (4.1).

The transmission from the protective silica window of the photosensors (PMT and SiPMs) to the actual photocathode is not considered, hence the refractive indices for both materials are equal. In order for the scintillation light to be absorbed in the photocathode and contribute to the LCE, the absorption length of the photocathode needs to be smaller than the actual thickness of the photocathode itself. Otherwise the simulated scintillation light would travel through the photocathode and could thus not be detected. The absorption length of the photocathode was set to 1 nm.

Refractive Indices	**Value**
Gaseous xenon (GXe)	1.00
Liquid xenon (LXe)	1.63
PTFE	1.58
Synthetic silca at PMT and SiPM	1.60
Photoscathode of PMT and SiPPM	1.60

Table 4.1: Refractive indices for different materials used in the LCE simulation [78].

4.2.1 S1 Signal LCE Simulation

The S1 simulation was performed for both designed top SiPM arrays denoted as configuration A and B shown in figure (4.2). Since the physical S1 signal is initiated in the liquid xenon volume of the TPC, the event production location within the simulation is set in a predefined production area in the liquid xenon just below the gate mesh (z = 0 mm) and the cathode (z = −30 mm). The liquid/gaseous xenon boundary is located at z = 2 mm. In order to remove potential photons trapped in the PTFE wall, the fiducial volume was limited with the condition $R^2 < 240.25\,\mathrm{mm}^2$. For both simulations a total of 10^6 S1 events with 5000 photons/event were simulated. Figure 4.3 shows for both performed simulations the distribution of the primary locations of the generated events in the x-y plane as well as the z-R^2 dependency. The events are uniformly generated in the entire LXe volume.

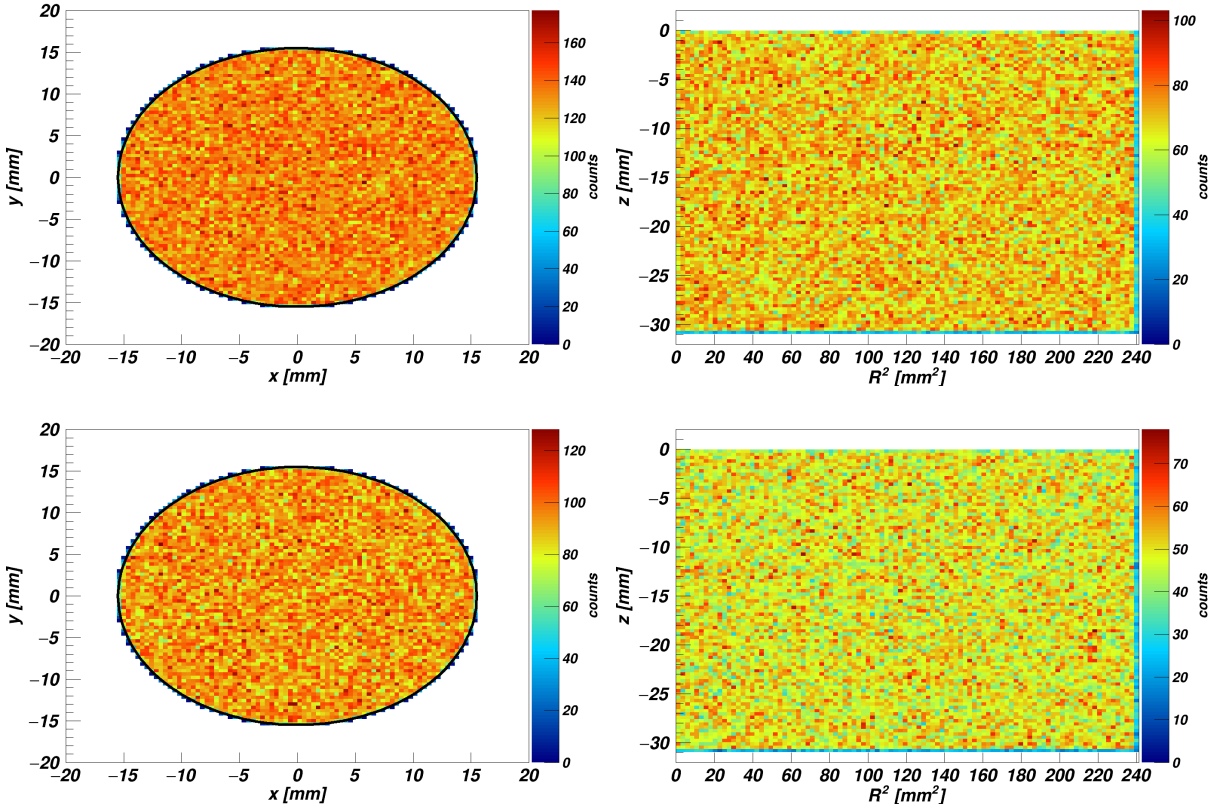

Figure 4.3: Primary location distribution of the generated S1 events in the x-y plane (Left) and in the z-R^2 plane (Right) for the top SiPM array configuration A (top) and configuration B (bottom).

If a simulated photon hits either the sensitive top SiPM array or the bottom PMT, the event information including the primary generation location and the absorption location in the corresponding photocathode is recorded and is included into the LCE measurement. The LCE measurements for both configurations A and B are shown in table 4.2 . The total LCE measurement is in good agreement with previous simulations results with no SiPMs included in the geometry. The S1 LCE for the top array for both configurations A and B are slightly lower than for a top PMT in previous simulations. This discrepancy can be explained by the fact, that the SiPM arrays do not cover the entire previous area from the top PMT. Due to stability requirements of the SiPM installation, the individual SiPMs cannot be mounted seamlessly and thus the PTFE spacing between the SiPMs are exposed to the interior of the TPC. Incident photons may reflect or are absorbed at these specific locations and therefore decrease the light collection efficiency to a small degree.

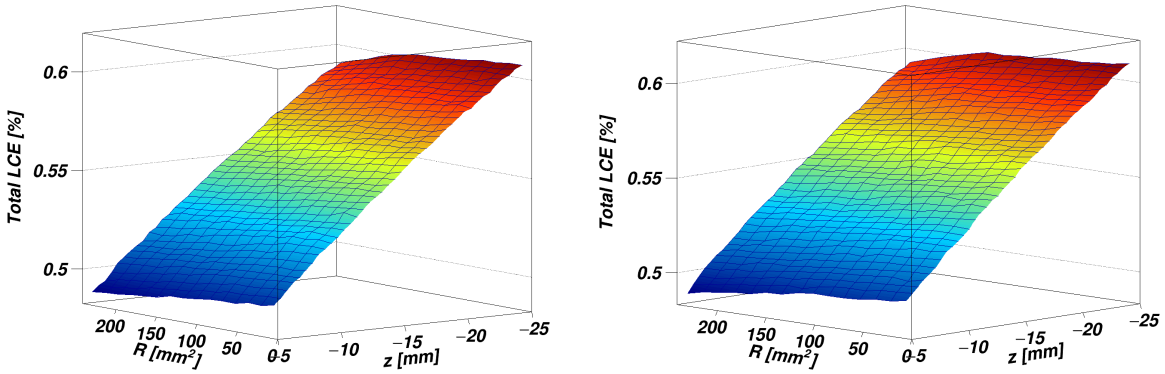

Figure 4.4: LCE maps for (Left) configuration A including 4 SiPM segmentations and (Right) configuration B including 16 segmentations.

The spacial total light collection efficiency map for both configurations A and B is shown in figure 4.4. The LCE map includes all registered events in the top and bottom photocathodes. It is clearly indicated that the total LCE increases with lower z. The total light collection efficiency increases therefore for events generated in the vicinity of the bottom PMT. The photons do not experience many reflections on the PTFE walls an also have shorter travel distances. Further the LCE is higher for events generated in the middle of the fiducial volume, since reflections are minimized. In order to evaluate which photocathode collects the most primary scintillation light, an asymmetry factor A_{sym} is introduced and is defined the following:

$$A_{\text{sym}} = \frac{N_{\text{top}} - N_{\text{bottom}}}{N_{\text{top}} + N_{\text{bottom}}} \quad , \tag{4.2}$$

with N_{bottom} the number of events detected by the bottom PMT and N_{top} the number of events detected by the SiPM array at the top. Figure 4.5 shows the spacial asymmetry distribution for both configurations A and B. For both configurations a negative value of the asymmetry factor A_{sym} is observed, which implies that the bottom PMT sees more light than the two top SiPM arrays. This can be explained by the reflection of the photons at the liquid/gaseous boundary. Photons originating from the liquid xenon phase get reflected due to the higher reflection index of liquid xenon in comparison to gaseous xenon ($n_{\text{LXe}} > n_{\text{GXe}}$).

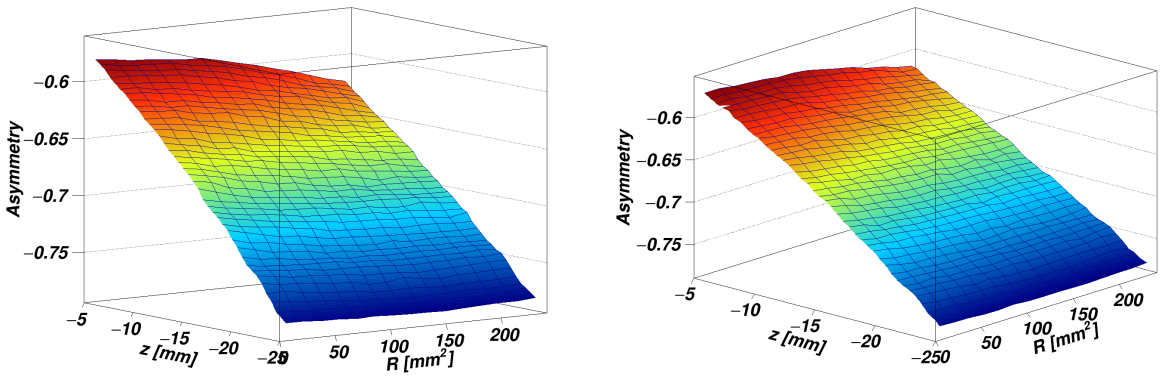

Figure 4.5: Asymmetry map for (Left) configuration A including 4 SiPM segmentations and (Right) configuration B including 16 segmentations.

Configuration A: SiPM Top Array with 4 Segments		
Hit location	**S1 Mean LCE [%]**	**S2 Mean LCE [%]**
Top SiPM array	8.52 ± 0.16	26.08 ± 0.63
Bottom PMT	46.51 ± 0.02	32.21 ± 0.04
Total (SiPM & PMT)	55.03 ± 0.16	58.29 ± 0.63

Configuration B: SiPM Top Array with 16 Segments		
Hit location	**S1 Mean LCE [%]**	**S2 Mean LCE [%]**
Top SiPM array	8.76 ± 0.13	27.06 ± 0.53
Bottom PMT	46.52 ± 0.03	32.14 ± 0.04
Total (SiPM & PMT)	55.28 ± 0.13	59.20 ± 0.53

Configuration C: 2 PMTs - no SiPM Array		
Hit location	**S1 Mean LCE [%]**	**RMS [%]**
Top PMT	12.67	1.88
Bottom PMT	46.74	5.13
Both PMTs	59.41	3.76

Table 4.2: (Top) Table shows the S1 and S2 LCE for the top array configuration A including SiPMs with 4 segmentations. (Middle) Table shows the LCE measurements for configuration B incorporating 4 SiPMs, which are segmented into 16 equally sized segments. (Bottom) Table shows the LCE measurements from a previous simulation with no SiPMs included. The configuration C incorporates two 2-inch PMTs - one at the top and the other at the bottom.

4.2.2 S2 LCE Simulation

For both SiPM top arrays an additional S2 simulation was performed. The S2 signal is induced by the extraction of ionization electrons into the gas phase of the TPC. Due to the secondary acceleration the electrons emit proportional scintillation photons, which are therefore produced mainly in the gaseous part of the TPC. Thus a new production volume for the simulation was determined just below the anode (z = 4 mm) and above the gate mesh (z = 0 mm) in the gaseous xenon volume. The liquid level is set to z = 2 mm. The upper limit of the production volume is defined as 0.1 mm below the anode at z = 3.9 mm and the lower limit at z = 3.3 mm. The distance of the upper limit of the production volume to the anode is in the same order as the distance of the top SiPM array to the anode. The implication of a different setting of the upper level of the production volume to the light collection efficiency is not examined in this simulation and would be part of a further detailed simulation study. For the S2 LCE simulation a total of 10^5 events were uniformly generated in the predefined production area. Each generated event corresponds to 10^4 photons in the VUV range. Figure 4.6 shows the two different SiPM top array configurations with the x-y distribution of the primary locations of the generated events. The events are uniformly generated, which is also emphasized in figure (4.6 - right) showing the z-R^2 event location distribution.

If a generated photon hits a specific part of the top SiPM array, the track properties are collected and is accounted for in the LCE simulation. This procedure is the same as in the S1 simulation, but provides due to the segmentation of the SiPM a higher granularity, which is promising for a potential event reconstruction of the primary events in the x-y plane. This study is done in section (4.2.3). The total S2 light collection efficiency is evaluated by the the sum of all LCE values of every individual segmentation of a specific configuration. Thus, a total S2 light collection efficiency for configuration A of (26.08 ± 0.63) % was achieved and maintained constant within the entire detector. For configuration B a total light collection efficiency of (27.06 ± 0.53) % was achieved and is within the statistical range as for configuration A (see table 4.2). The total S2 light collection efficiency should not differ with different segmentations of the SiPM top array, since both configurations cover the same area and are not rearranged in any way. Figure 4.7 shows the total S2 top light collection efficiency over R^2 for both configurations A and B. For the fitting of the LCE distribution over R^2 the event distribution of every slice i was fitted with a Gaussian and the mean value μ_i and the $3\sigma_i$ evaluated. Plotting all mean values μ_i and the corresponding $3\sigma_i$ intervals show that most of the generated events are within the 3σ band.

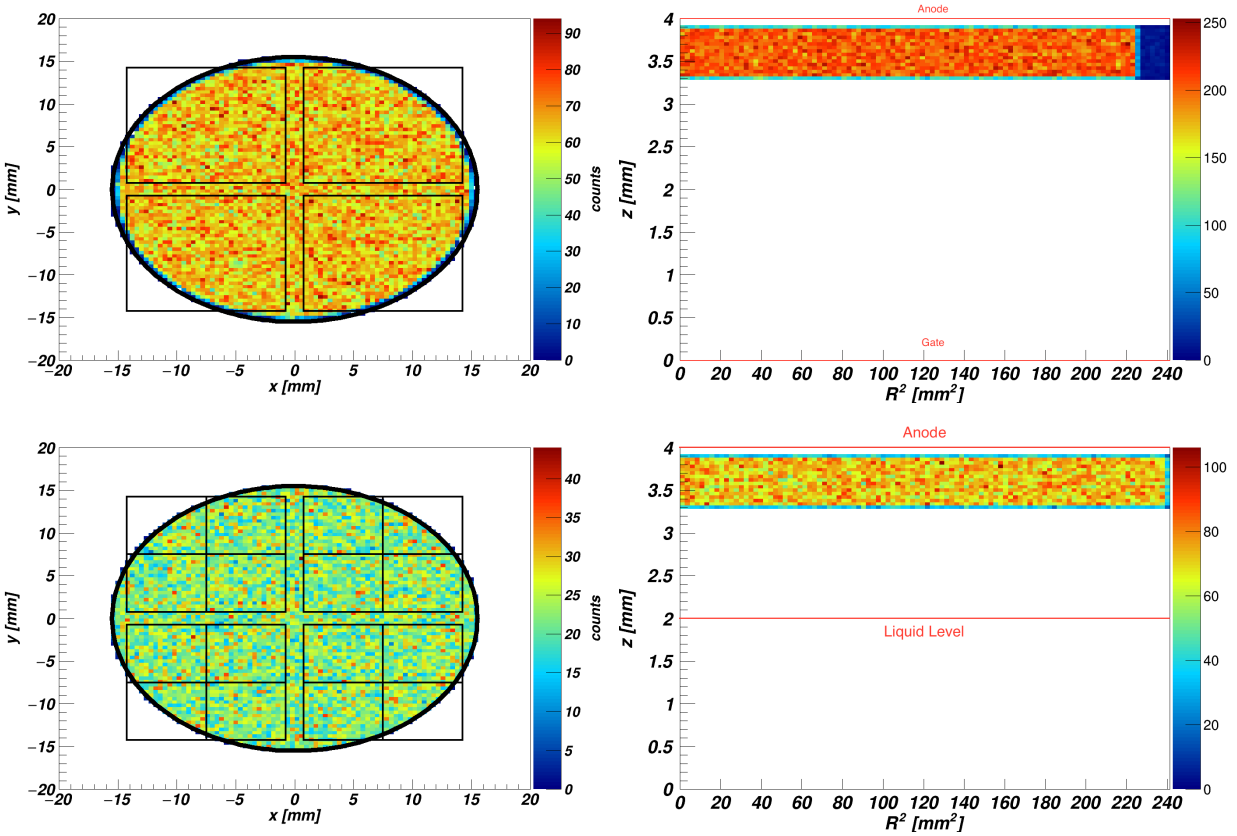

Figure 4.6: The left plots show the primary event location distribution in the xy-plane for the top array configuration A (top) and for configuration B (bottom). The four respectively 16 SiPM segments are highlighted with black rectangles with the correct dimensions. The right plots show the predefined production area for configuration A (top) and configuration B (bottom) in the zR^2-plane. The anode (z = 4 mm), the liquid level (z = 2 mm) and the gate (z = 0 mm) are highlighted with red lines.

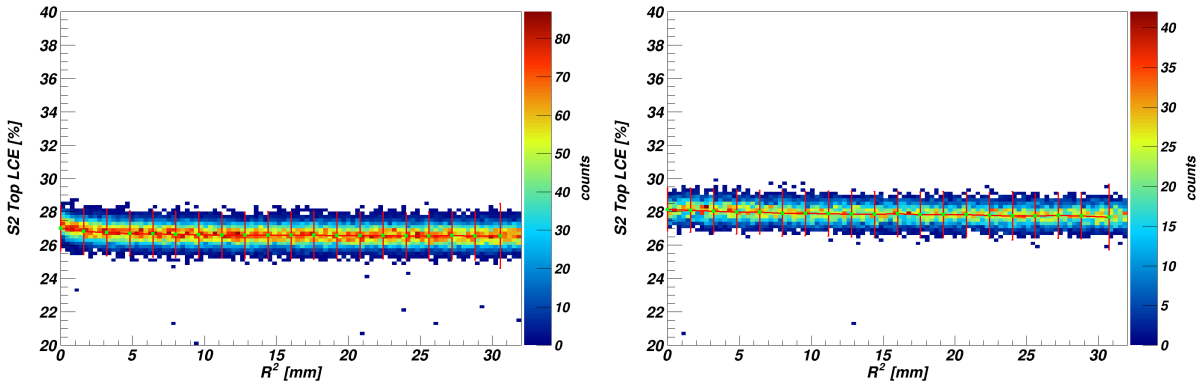

Figure 4.7: The total S2 Top LCE for both top SiPM arrays with 4 segmentations (Left) and 16 segmentations (Right). The total S2 LCE is constant over the entire detector range for both configurations and all generated events are within the 3σ range shown in red.

4.2.3 S2 XY Position Reconstruction

In a dual-phase xenon detector the 3D event position can be determined with two distinct methods. The z position within the TPC can be determined through the drift time of the ionization electrons from the primary event location to the liquid-gas interface. The xy-position on the contrary can be determined from the S2 signal distribution in the top PMT or top SiPM array by applying specific reconstruction algorithms and compare the reconstruction locations with Monte Carlo data. For the xy-position reconstruction of the S2 signal distribution on the top SiPM array from the simulation performed in section 4.2.2, a center-of-gravity (COG) based algorithm was used:

$$\vec{r} = \frac{\sum_{i=1}^{N} N_{\mathrm{pe}}^{i} \vec{r_i}}{\sum_{i=1}^{N} N_{\mathrm{pe}}^{i}} \quad , \tag{4.3}$$

where N_{pe}^{i} is the number of detected photoelectrons of a SiPM segment i within a top array configuration, $\vec{r_i}$ represents the projection vector of each SiPM segment i center on the xy-plane and $\vec{r}$ represents the reconstructed event position. For the position reconstruction for the SiPM top array configuration A the upper bound of the summation in equation (4.3) is N=4 and N=16 for the SiPM configuration B respectively.

Figure 4.8 shows the reconstructed event position achieved with the center of gravity algorithm for both SiPM top array configurations. It is clearly shown, that all reconstructed positions are biased to the center of the TPC. In order to achieve a proper position reconstruction a further scaling has to be taken into account. The anode mesh will be visible by applying the COG-algorithm to a real data sample (e.g Kr83m). The non-linear scaling factor can then be extracted by comparing the real mesh size with the reconstructed mesh size and an appropriate fiducial volume can be determined for the exclusion of boundry effects. Figure B.1 show the radial distribution of the primary location of the generated events in the simulation for both SiPM top array configurations. Comparing the distribution with the reconstructed event location with the COG-algorithm shows a non linear development of the radial distribution. For larger radii optical warping and position reconstruction degeneracy is observed. The COG-algorithm is not an optimal reconstruction method. For an improved location reconstruction a further method like neural networking (NN) can be used. The individual SiPM segment LCE maps (seen in figure B.3) can be be used as a basis for an artificial neural network (ANN) reconstruction.

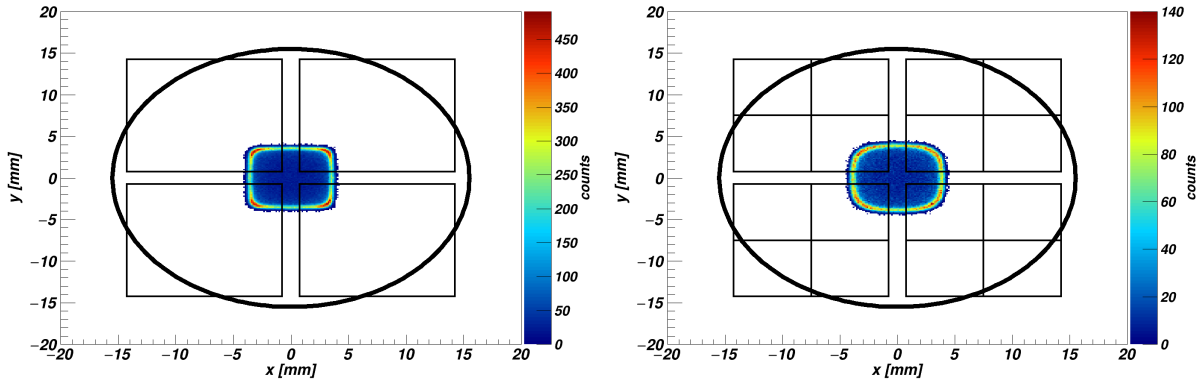

Figure 4.8: Reconstructed S2 events with the COG-algorithm for the SiPM top array configuration A (Left) and configuration B (Right). These are not the actual positions.

CHAPTER 5

Conclusion and Future Prospects

In order to fully satisfy the requirements of novel VUV-SiPMs for a potential implementation in large-scale dark matter experiments such as DARWIN, more R&D work needs to performed. During the work of this thesis, several new ideas for additional SiPM measurements and potential simulation extensions emerged. This short chapter should give a short conclusion on the performed work during this thesis and should present a few new ideas for future projects.

Characterisation of VUV3 and VUV4 SiPM

LArS Facility: The LArS facility was successfully operated at a constant low temperature of T=170K with small fluctuation in the order of 20 mK. It was shown, that the setup is able to gradually decrease the temperature to a desired value and sustain it for a long period of time. It is thus a suitable setup for the characterisation of SiPMs at cryogenic temperatures and is able to be operated with either gaseous nitrogen or gaseous/liquid argon. In a further experimental run argon was successfully liquefied, which would encourage further scintillation light measurements induced by a suitable radioactive source in the interior of the setup. The LArS facility is constructed in such a way, that future measurements with multiple SiPMs or a variation of SiPMs and PMTs can be performed.

Gain: The gain of the VUV3 6 × 6 mm SiPM at T=170K is $\sim 1.54 \times 10^6$ and was operated at an over-voltage of 7.00 V. The next-generation VUV4 SiPM prototypes of Type 10 and 11 were measured at a temperature of T=170K and showed a gain of 1.5 $\times 10^6$ at an over-voltage of 4.19V and 3.94V, respectively. The long-term gain evolution measurements for all three SiPM models in either gaseous nitrogen or liquid argon, showed a stable gain with fluctuations of less than 1%. Further, a temperature-dependent gain measurement of all three SiPM models in a temperature interval of 170K-300K were performed and showed a linear decreasing breakdown voltage. A change in the breakdown voltage of (51.3 ± 0.8) mV/K for the VUV3 6 × 6 mm, (50.8 ± 0.6) mV/K for the VUV4 Type 10 and (51.8 ± 0.7) mV/K for the VUV4 SiPM of Type 11 were observed. In addition, the effective capacitance C_{eff} of both VUV4 SiPMs showed a constant value of C_{eff} =(567.2 ± 0.3) fF for Type 10 and C_{eff} =(573.3 ± 0.2) fF for Type 11 SiPM over the measured temperature range. For the VUV3 6 × 6 mm SiPM a drastic change in the effective capacitance at T=190K was observed. The effective capacitance C_{eff} at high temperatures of T=300K is C_{eff} = (460.8 ± 0.6) fF and changes rapidly to a constant value of C_{eff} = (356.4 ± 0.2) fF at lower temperature of T=170K.

Dark Count: The measured mean dark count rate of the VUV3 6 × 6 mm SiPM at T=170K and a gain of 1.5 $\times 10^6$ is $\sim$ 21 Hz. The long-term stabililty measurement at T=170K show besides a stable gain also a stable DCR during a data-taking window of five days. The dark count rate for the VUV4 SiPM of Type 10 and 11 were extrapolated from the temperature-dependent DCR measurements and were calculated at a gain of 1.5 $\times 10^6$ to be 7.1 Hz for the VUV4

Type 10 and 2.2 Hz for the VUV4 Type 11 respectively. The extrapolated dark count rate of the VUV3 6 × 6 mm SiPM is 39.4 Hz and is in the same order of magnitude as the measured dark count rate from the long-term stability measurement. This method redeemed itself to be a good upper estimate for dark count rates at lower temperatures (T < 210K).

In general, the dark count rate for all three SiPM models are still to high for an implementation in large-scale detectors such as DARWIN. With the assumption of implementing 225000 potential VUV3 SiPM in a large-scale TPC, the 3-fold accidental coincidence of the S1 signal induced by random dark count events for the VUV3 6 × 6 mm SiPM was calculated to be 1.8 kHZ. This value is in comparison to the 3-inch PMT currently operated in the XENON1T experiment, six order of magnitudes higher. With a further assumption of a 1.0 Hz lone S2-signal rate, induced by delayed extracted ionization electrons, the 3-fold accidental event coincidence is in the order of 5 Hz. Thus, the VUV3 6 × 6 mm SiPM in its current form is not suitable for an implementation in large-scale xenon-based TPCs. In order for SiPMs to be a viable competitor to the vacuum-based photomultipliers, the dark count rate needs to be significantly reduced by the manufacturers.

Crosstalk: The crosstalk (CT) probability for all three SiPM models showed an exponential over-voltage dependence. The CT probability of VUV3 6 × 6 mm SiPM at a gain of 1.5 $\times 10^6$ is $\sim$ 6.9 % at a temperature of T=170K, whereas for the VUV4 Type 10 the CT probability was measured to be 2.5% and 2.3% for the VUV4 Type 11 SiPM respectively. The crosstalk probability per unit area is in the same order of magnitude for all three tested SiPM and is constant over temperature at a certain applied over-voltage.

Afterpulse: The Afterpulse rate was measured with a non-standard method and resulted in a general overestimation of the afterpulse rate in all three SiPMs. For all three SiPM models an exponential increasing AP-rate for higher applied over-voltages is observed. The rise of the probability with rising over-voltage could be explained by the greater number of electrons that gain enough energy to occupy the trap levels. The afterpulse rate at a gain of 1.5 $\times 10^6$ at a temperature of T=170K for the VUV3 6 × 6 mm SiPM was measured to be $\sim$ 40 %, and 9.4% for the VUV4 Type 10 and 6.4 % for the VUV4 SiPM of Type 11 respectively. For all three SiPM the AP-rate per unit area is in the same order of magnitude and are currently to high for an implementation in large-scale xenon-based TPCs. By purifying the silicon used for the SiPM construction, the AP-rates can be significantly reduced.

Light Collection Efficiency

For the entire light collection efficiency simulation two newly designed SiPM top arrays, incorporating four VUV3 12 × 12 mm SiPM, were successfully implemented in the XURICH-II detector geometry in the GEANT4 framework. The two top array configurations A and B were divided into 4 and 16 equal sized segments, respectively.

S1 & S2 Light Collection Efficiency: The S1 signal simulation showed for the top array configuration A a light collection efficiency of (8.52 ± 0.16) % and a light collection efficiency of (8.76 ±0.13)% for configuration B. The total light collection efficiency, which also includes the bottom PMT, is (55.03 ± 0.16) % for configuration A and (55.28 ± 0.13) % for configuration B. Both results are in the same order as for a previously performed LCE simulation with two PMTs 59.41% with RMS = 3.76%. A total S2 light collection efficiency for configuration A of (26.08 ± 0.63) % was achieved and maintained constant within the entire detector. For configuration B a total light collection efficiency of (27.06 ± 0.53) % was achieved and is within the statistical range as for configuration A.

XY-Reconstruction: A simple center-of-gravity (COG) based algorithm was used for the xy-reconstruction of the primary generated S2 events. The COG-algorithm showed poor results

in its ability to reconstruct the xy-position of the generated events. The reconstructed positions are biased to the center. For larger radii optical warping and position reconstruction degeneracy is observed.

Future Prospects

- This thesis should serve as a good basis for future SiPM characterisations. To fully understand the performance of novel VUV-SiPM and investigate their potential for xenon-based detectors, a full characterisation of the VUV3 and VUV4 SiPM needs to be performed in liquid and gaseous xenon. By inserting an americium (^{241}Am) radioactive source into the cryostat, the ability of the new VUV-SiPM to detect scintillation light of xenon (λ=178nm) can be tested.
- The drastic change of the effective capacitance of the VUV3 6 $\times$ 6 mm SiPM during the temperature-dependent gain measurements needs to be further investigated.
- The non-standard method of calculating the afterpulse rate is unsatisfactory. A dedicated afterpulse measurement setup with a Time-to-Digital Converter (TDC) needs to be performed for a better knowledge of the extent of the afterpulse rate of SiPMs. An extensive temperature-dependent afterpulse rate analysis can be of further interest.
- The designed top array for the XURICH-II detector can be constructed and implemented into the detector for further R&D studies of SiPMs in a small TPC.
- A further interesting study is to implement the real physical shape of the electrodes into the geometry of the XURICH-II detector and investigate its implications on the light collection efficiency of the top SiPM array.
- The COG-algorithm showed poor results in the LCE simulation. The COG-algorithm can be applied to a real data sample (e.g Kr83m). The anode mesh will then be visible. The non-linear scaling factor can then be extracted by comparing the real mesh size with the reconstructed mesh size. This scaling factor can then be used to correct the reconstruced xy-event positions. Further an appropriate fiducial volume can then be determined for the exclusion of boundary effects.
- For an improved xy-reconstruction in the LCE simulation, the individual SiPM segment LCE maps from the two top array configurations can be used to train an artificial neural network algorithm. The dependence of the SiPM array granularity to the reconstruction resolution can then be further investigated.

List of Figures

List of Tables

APPENDIX A

SiPM Characterisation

Breakdown Voltage Results

	VUV3 6×6 mm	**VUV4 Type 10**	**VUV4 Type 11**
Temperature [K]	V_{Break}[V]	V_{Break}[V]	V_{Break}[V]
110	42.81	-	-
130	43.43	-	-
150	44.21	-	-
170	45.14	44.73	44.93
190	46.30	45.62	45.62
210	47.59	46.58	46.74
230	48.54	47.55	47.85
235	48.77	47.87	48.11
240	48.94	48.09	48.35
245	49.18	48.37	48.63
250	49.41	48.64	48.90
255	49.70	48.92	49.17
260	49.92	49.18	49.39
270	50.17	49.72	49.95
300	52.15	51.31	51.51

Table A.1: Temperature-dependent breakdown voltage for the tested VUV3 6× 6 mm SiPM (in nitrogen) and the VUV4 of the Type 10 and 11 (in argon). The statistical error on the voltage is ± 10mV

Longterm Gain Measurement

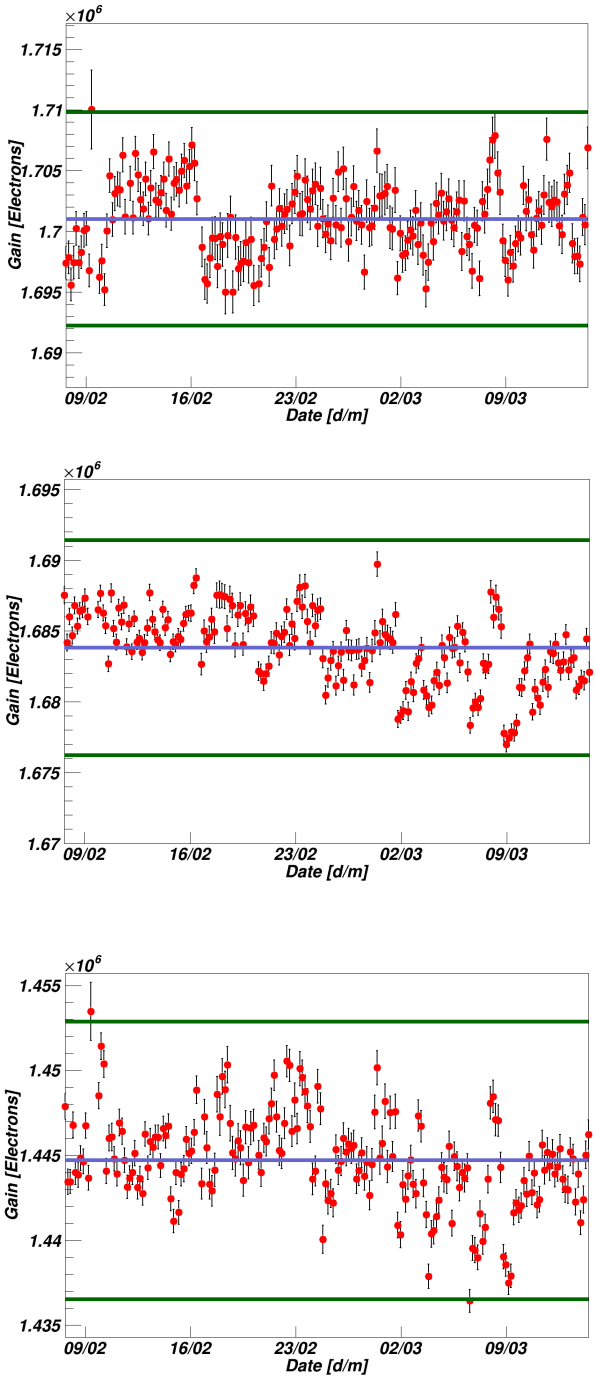

Figure A.1: Longterm gain stability measurement in LAr for VUV4 6×6 mm (top) and VUV3 SiPM of Type 10 (middle) and Type 11 (bottom) in a time period of 1 month. The purple line shows the mean gain and the green lines the 3× RMS interval. The gain fluctuation is less than 1% for both SiPMs during the entire data-taking period.

Dark Count Measurement

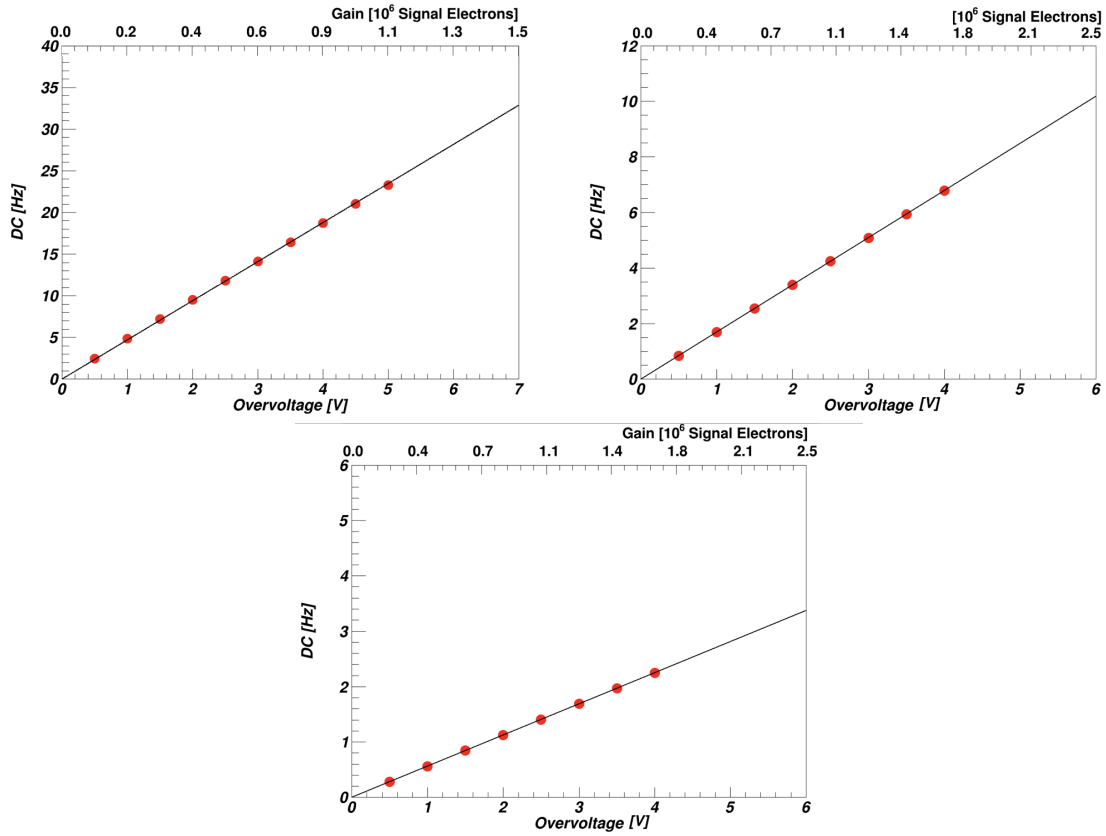

Figure A.2: Extrapolated DC rate at T=170K for the 6×6 mm VUV3 SiPM (top, left), VUV4 SiPM Type 10 (top, right) and VUV4 SiPM Type 11 (bottom).

APPENDIX B

Light Collection Efficiency

XY-Position Reconstruction

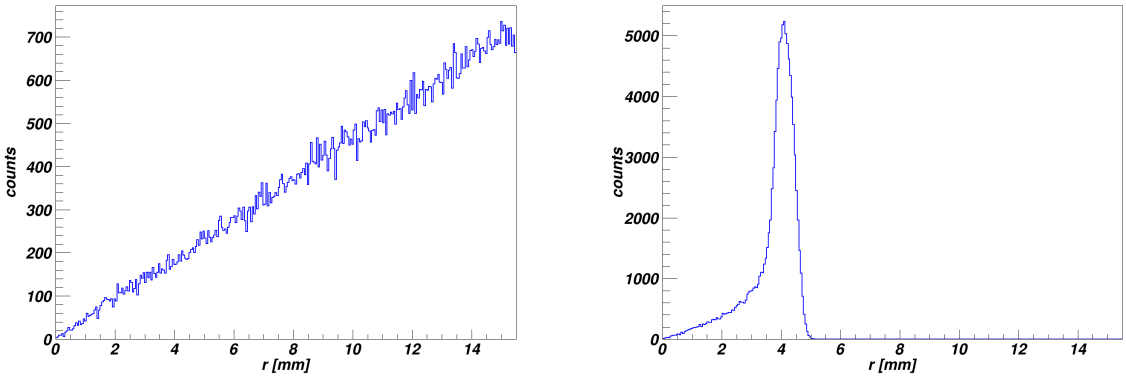

Figure B.1: S2 LCE Simulation - Radial distribution of primary location of generated events (left) for a top SiPM array with 16 segmentations. (right) The reconstructed event location with a Center-of-Gravity algorithm.

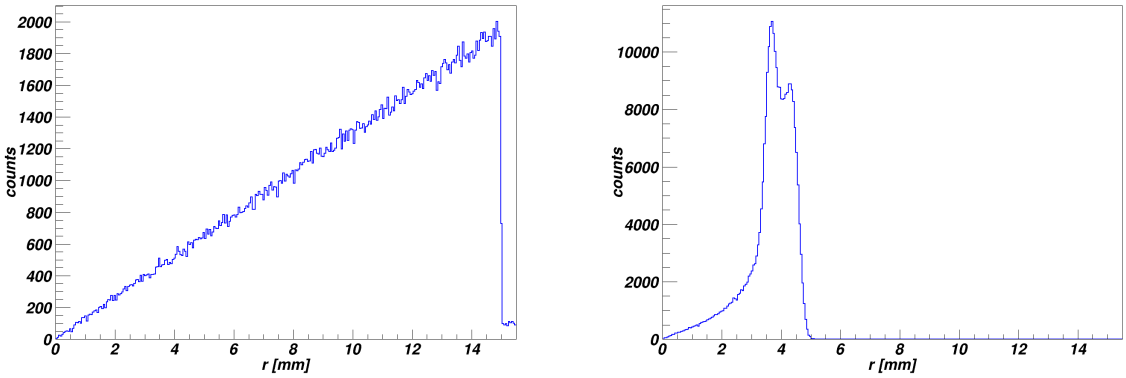

Figure B.2: S2 LCE Simulation - Radial distribution of primary location of generated events (left) for a top SiPM array with 4 segmentations. (right) The reconstructed event location with a Center-of-Gravity algorithm.

Light Collection Efficiency Maps

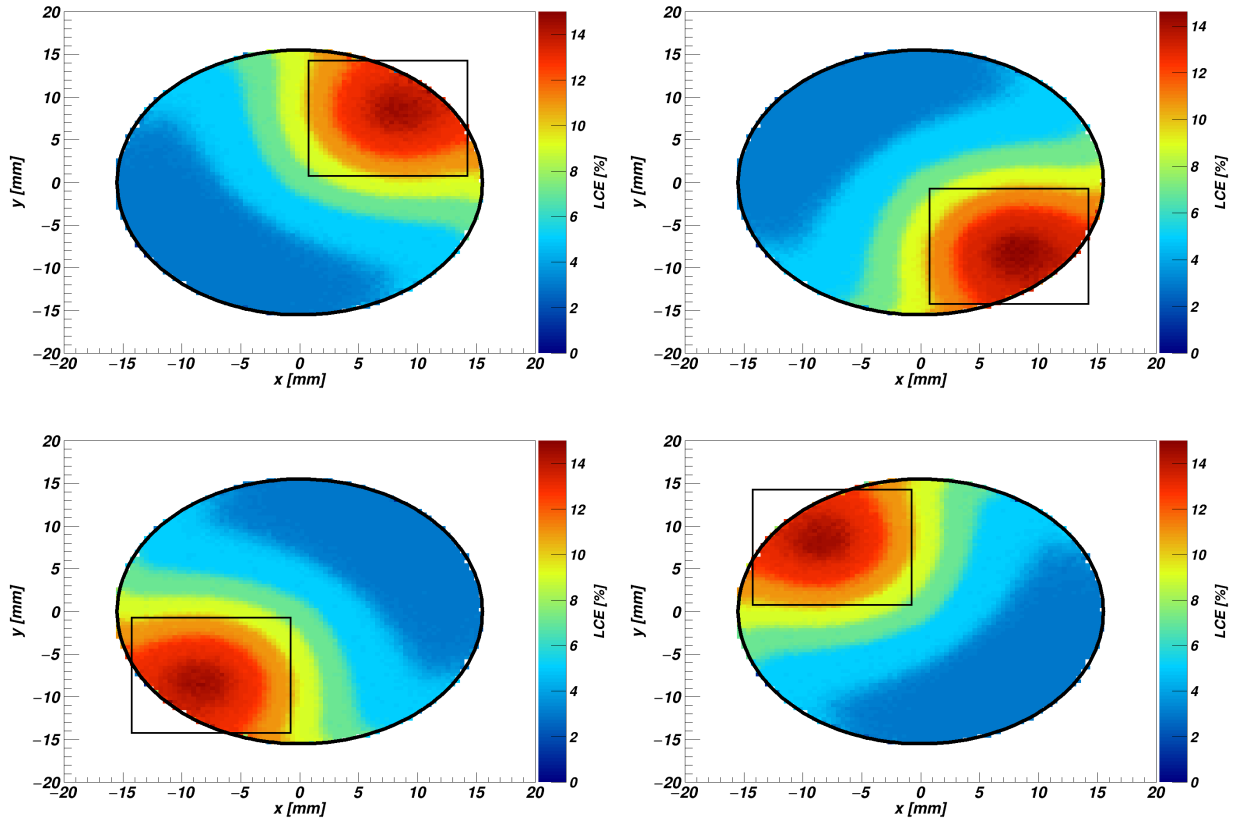

Figure B.3: S2 LCE map for 4SiPM segmentations

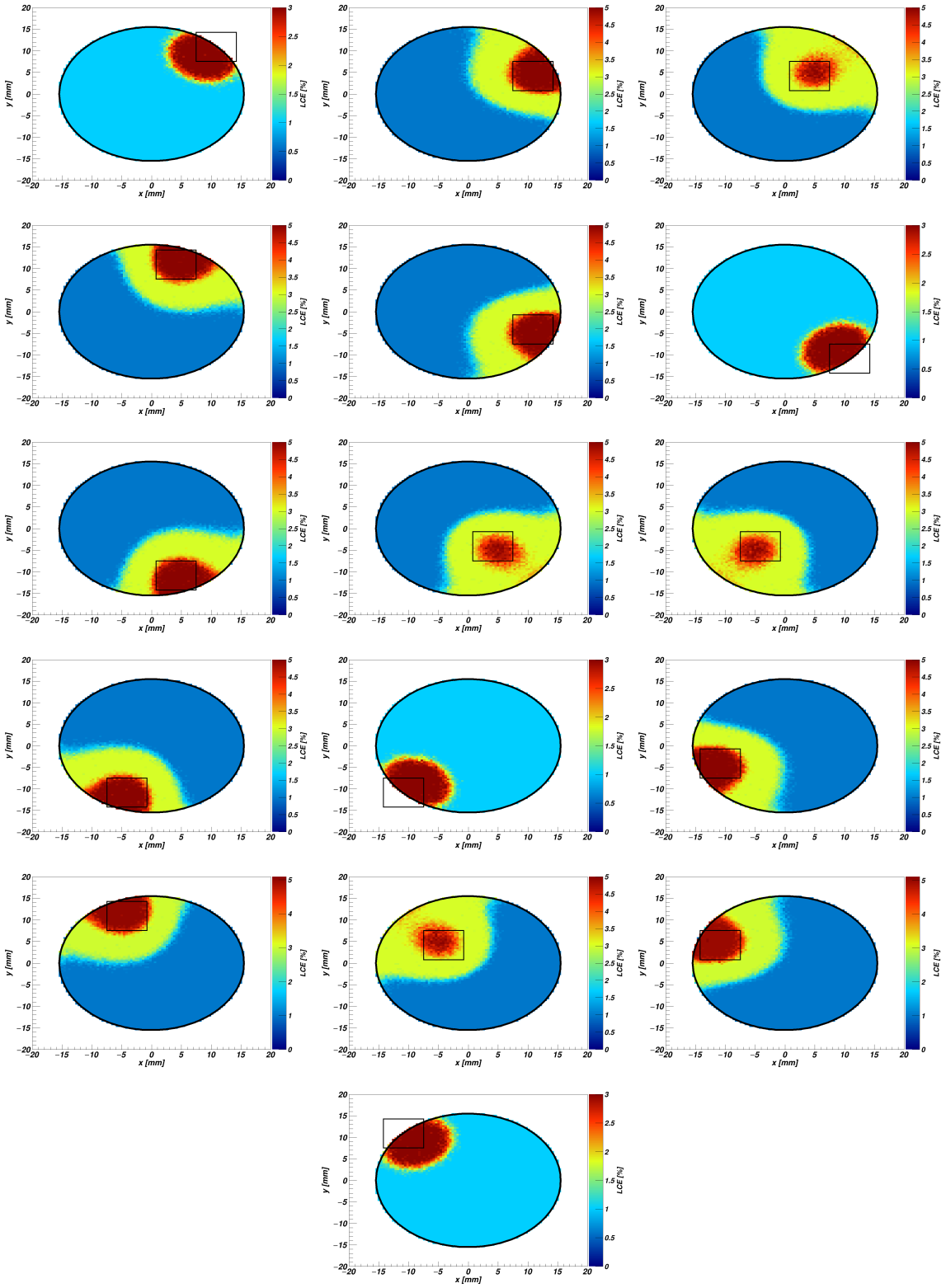

Figure B.4: S2 LCE map for 16 SiPM segmentations

Bibliography

[1] P. Gondolo, "Non-baryonic dark matter," *NATO Sci. Ser. II*, vol. 187, pp. 279–333, 2005. [,279(2003)].

[2] F. Zwicky, "Nebulae as Gravitational Lenses," *Phys. Rev. 51, 290*, 1936.

[3] F. Zwicky, "Die Rotverschiebung von extragalaktischen Nebeln," *Helvetica Physica Acta*, vol. 6, pp. 110–127, 1933.

[4] V. C. Rubin and W. K. Ford, Jr., "Rotation of the Andromeda Nebula from a Spectroscopic Survey of Emission Regions," *Astrophysical Journal*, vol. 159, p. 379, Feb. 1970.

[5] G. D'Amico, M. Kamionkowski, and K. Sigurdson, "Dark Matter Astrophysics," *ArXiv*, July 2009.

[6] K. G. Begeman, A. H. Broeils, and R. H. Sanders, "Extended rotation curves of spiral galaxies - Dark haloes and modified dynamics," *Monthly Notices of the Royal Astronomical Society*, vol. 249, pp. 523–537, Apr. 1991.

[7] Wambsganss, "Gravitational Lensing in Astronomy." `https://doi.org/10.12942/lrr-1998-12`, (1998).

[8] Bartelmann, Matthias and Maturi, Matteo, "Weak gravitational lensing," 2016.

[9] D. Clowe, M. Bradač, A. H. Gonzalez, M. Markevitch, S. W. Randall, C. Jones, and D. Zaritsky, "A direct empirical proof of the existence of dark matter," *The Astrophysical Journal Letters*, vol. 648, no. 2, p. L109, 2006.

[10] N. Benitez et al., "Abell 1689 Warps Space." `https://apod.nasa.gov/apod/ap030109.html`, (2003).

[11] M. Markevitch et al., "The Bullet Cluster." `http://chandra.harvard.edu/photo/2006/1e0657/`, (2003).

[12] P. Salati, "Dark Matter Annihilation in the Universe," *Int. J. Mod. Phys. Conf. Ser.*, vol. 30, p. 1460256, 2014.

[13] F. Calore, V. de Romeri, and F. Donato, "Conservative upper limits on WIMP annihilation cross section from Fermi-LAT gamma rays," *Physical Review D*, vol. 85, p. 023004, Jan. 2012.

[14] F. Aharonian *et al.*, "Observations of the Crab Nebula with H.E.S.S," *Astron. Astrophys.*, vol. 457, pp. 899–915, 2006.

[15] Aleksi, "Performance of the MAGIC stereo system obtained with Crab Nebula data," *Astroparticle Physics*, vol. 35, pp. 435–448, Feb. 2012.

[16] J. Holder *et al.*, "Status of the VERITAS Observatory," *AIP Conf. Proc.*, vol. 1085, pp. 657–660, 2009.

[17] M. Doro *et al.*, "Dark Matter and Fundamental Physics with the Cherenkov Telescope Array," *Astropart. Phys.*, vol. 43, pp. 189–214, 2013.

[18] M. Actis, G. Agnetta, F. Aharonian, A. Akhperjanian, J. Aleksicć, E. Aliu, D. Allan, I. Allekotte, F. Antico, L. A. Antonelli, and et al., "Design concepts for the Cherenkov Telescope Array CTA: an advanced facility for ground-based high-energy gamma-ray astronomy," *Experimental Astronomy*, vol. 32, pp. 193–316, Dec. 2011.

[19] J. Conrad, "Indirect Detection of WIMP Dark Matter: a compact review," in *Interplay between Particle and Astroparticle physics (IPA2014) London, United Kingdom, August 18-22, 2014*, 2014.

[20] A. Achterberg *et al.*, "First Year Performance of The IceCube Neutrino Telescope," *Astropart. Phys.*, vol. 26, pp. 155–173, 2006.

[21] M. Ageron, J. A. Aguilar, I. Al Samarai, A. Albert, F. Ameli, M. André, M. Anghinolfi, G. Anton, S. Anvar, M. Ardid, and et al., "ANTARES: The first undersea neutrino telescope," *Nuclear Instruments and Methods in Physics Research A*, vol. 656, pp. 11–38, Nov. 2011.

[22] J. Lavalle and P. Salati, "Dark Matter Indirect Signatures," *Comptes Rendus Physique*, vol. 13, pp. 740–782, 2012.

[23] G. A. Gomez-Vargas, M. A. Sánchez-Conde, J.-H. Huh, M. Peiro, F. Prada, A. Morselli, A. Klypin, D. G. Cerdeno, Y. Mambrini, and C. Munoz, "Constraints on WIMP annihilation for contracted dark matterin the inner Galaxy with the Fermi-LAT," *JCAP*, vol. 1310, p. 029, 2013.

[24] M. Cirelli, "Dark matter indirect searches: charged cosmic rays," *Journal of Physics: Conference Series*, vol. 718, no. 2, p. 022005, 2016.

[25] P. Picozza *et al.*, "PAMELA: A Payload for Antimatter Matter Exploration and Light-nuclei Astrophysics," *Astropart. Phys.*, vol. 27, pp. 296–315, 2007.

[26] O. Adriani *et al.*, "An anomalous positron abundance in cosmic rays with energies 1.5-100 GeV," *Nature*, vol. 458, pp. 607–609, 2009.

[27] J. N. Bahcall, R. M. Soneira, and M. Schmidt, "The galactic spheroid," *Astrophysical Journal*, vol. 265, pp. 730–747, Feb. 1983.

[28] F. Reindl *et al.*, "The CRESST Dark Matter Search - Status and Perspectives," in *Proceedings, 12th Conference on the Intersections of Particle and Nuclear Physics (CIPANP 2015): Vail, Colorado, USA, May 19-24, 2015*, 2015.

[29] E. Armengaud *et al.*, "Performance of the EDELWEISS-III experiment for direct dark matter searches," *JINST*, vol. 12, no. 08, p. P08010, 2017.

[30] R. Agnese *et al.*, "Results from the Super Cryogenic Dark Matter Search Experiment at Soudan," *Phys. Rev. Lett.*, vol. 120, no. 6, p. 061802, 2018.

[31] M. A. et al., "Search of neutrinoless double beta decay with the gerda experiment," *Nuclear and Particle Physics Proceedings*, vol. 273-275, pp. 1876 – 1882, 2016. 37th International Conference on High Energy Physics (ICHEP).

[32] S. T. Petcov, "The Nature of Massive Neutrinos," *Adv. High Energy Phys.*, vol. 2013, p. 852987, 2013.

[33] K. Abe and the XMASS Collaboration, "XMASS detector," *Nuclear Instruments and Methods in Physics Research A*, 2013.

[34] N. Fatemighomi, "DEAP-3600 dark matter experiment," in *35th International Symposium on Physics in Collision (PIC 2015) Coventry, United Kingdom, September 15-19, 2015*, 2016.

[35] K. Rielage *et al.*, "Update on the MiniCLEAN Dark Matter Experiment," *Phys. Procedia*, vol. 61, pp. 144–152, 2015.

[36] T. Bruch, "Recent results from the CDMS-II experiment," in *Proceedings, 4th Patras Workshop on Axions, WIMPs and WISPs (AXION-WIMP 2008): Hamburg, Germany, June 18-21, 2008*, pp. 91–94, 2008.

[37] J. Calvo *et al.*, "Commissioning of the ArDM experiment at the Canfranc underground laboratory: first steps towards a tonne-scale liquid argon time projection chamber for Dark Matter searches," *JCAP*, vol. 1703, no. 03, p. 003, 2017.

[38] D. A. et al., "The large underground xenon (lux) experiment," *Nuclear Instruments and Methods in Physics Research Section A: Accelerators, Spectrometers, Detectors and Associated Equipment*, vol. 704, pp. 111 – 126, 2013.

[39] K. Han, "PandaX-III: Searching for Neutrinoless Double Beta Decay with High Pressure Gaseous Time Projection Chambers," in *15th International Conference on Topics in Astroparticle and Underground Physics (TAUP 2017) Sudbury, Ontario, Canada, July 24-28, 2017*, 2017.

[40] X. Collaboration, "The XENON100 dark matter experiment," *Astroparticle Physics*, vol. 35, pp. 573–590, Apr. 2012.

[41] E. Aprile *et al.*, "The XENON1T Dark Matter Experiment," *Eur. Phys. J.*, vol. C77, no. 12, p. 881, 2017.

[42] B. J. Mount *et al.*, "LUX-ZEPLIN (LZ) Technical Design Report," 2017.

[43] E. Aprile and Xenon Collaboration, "The XENONnT Dark Matter Experiment," in *APS April Meeting Abstracts*, p. J9.003, Jan. 2017.

[44] J. Liu, X. Chen, and X. Ji, "Current status of direct dark matter detection experiments," *Nature Phys.*, vol. 13, no. 3, pp. 212–216, 2017.

[45] J. Aalbers *et al.*, "DARWIN: towards the ultimate dark matter detector," *JCAP*, vol. 1611, p. 017, 2016.

[46] L. Baudis, "DARWIN: dark matter WIMP search with noble liquids," *J. Phys. Conf. Ser.*, vol. 375, p. 012028, 2012.

[47] T. Marrodán Undagoitia and L. Rauch, "Dark matter direct-detection experiments," *J. Phys.*, vol. G43, no. 1, p. 013001, 2016.

[48] A. Hitachi, "Properties of liquid xenon scintillation for dark matter searches," *Astroparticle Physics*, vol. 24, no. 3, pp. 247 – 256, 2005.

[49] N. Kaixuan, *Development of a Liquid Xenon Time Projection Chamber for the XENON Dark Matter Search*. PhD thesis, University of Columbia, 2006.

[50] M. Schumann, L. Baudis, L. Buetikofer, A. Kish, and M. Selvi, "Dark matter sensitivity of multi-ton liquid xenon detectors," *JCAP*, vol. 1510, no. 10, p. 016, 2015.

[51] N. Ackerman *et al.*, "Observation of Two-Neutrino Double-Beta Decay in ^{136} Xe with EXO-200," *Phys. Rev. Lett.*, vol. 107, p. 212501, 2011.

[52] E. Aprile *et al.*, "Physics reach of the XENON1T dark matter experiment," *JCAP*, vol. 1604, no. 04, p. 027, 2016.

[53] A. Hitachi, T. Takahashi, N. Funayama, K. Masuda, J. Kikuchi, and T. Doke, "Effect of ionization density on the time dependence of luminescence from liquid argon and xenon," *Phys. Rev. B*, vol. 27, pp. 5279–5285, May 1983.

[54] T. Doke, A. Hitachi, J. Kikuchi, K. Masuda, H. Okada, and E. Shibamura, "Absolute scintillation yields in liquid argon and xenon for various particles," *Japanese Journal of Applied Physics*, vol. 41, no. 3R, p. 1538, 2002.

[55] M. Schumann, "Dual-Phase Liquid Xenon Detectors for Dark Matter Searches," *JINST*, vol. 9, p. C08004, 2014.

[56] E. Aprile and L. Baudis, "Liquid noble gases," in *In *Bertone, G. (ed.): Particle dark matter* 413-436*, 2010.

[57] C. Kittel, *Einführung in die Festkörperphysik*. 978-3-486-59755-4: Gruyter, de Oldenbourg, 2013.

[58] R. J. Tilley, *Understanding Solids*. 978-1-118-42346-2: Wiley-VCH, 2013.

[59] P. Hofmann, *Solid State Physics - An Introduction*. 978-3-527-40861-0: Wiley-VCH, 2008.

[60] D. Sandro, "Characterization of silicon photomultiplier arrays in liquid xenon and development of dedicated read-out electronics," Master's thesis, University of Zurich, 2016.

[61] B. F. A. et al., "Geiger-mode avalanche photodiodes for three-dimensional imaging," *Lincoln Laboratory Journal*, vol. 13, pp. 335–349, 2002.

[62] Hamamatsu, "A technical guide to silicon photomultipliers (sipm)." `https://www.hamamatsu.com/us/en/community/optical_sensors/articles/technical_guide_to_silicon_photomultipliers_sipm/index.html`.

[63] First-Sensor, "Introduction to silicon photomultipliers (sipm)." `https://www.first-sensor.com/cms/upload/appnotes/AN_SiPM_Introduction_E.pdf`.

[64] A. M. Baldini *et al.*, "The design of the MEG II experiment," 2018.

[65] I. Ostrovskiy *et al.*, "Characterization of Silicon Photomultipliers for nEXO," *IEEE Trans. Nucl. Sci.*, vol. 62, no. 4, pp. 1825–1836, 2015.

[66] C. E. Aalseth *et al.*, "DarkSide-20k: A 20 Tonne Two-Phase LAr TPC for Direct Dark Matter Detection at LNGS," 2017.

[67] J. Wulf, "WARP- Offline Processing Tool." `https://github.com/Physik-Institut-UZH/WARP`, 2014.

[68] S. Piatek, "Effects of temperature on dark count rates in a silicon photomultiplier (sipm)." `http://www.hamamatsu.com/eu/en/community/optical_sensors/articles/temperature_and_sipm_dark_counts/index.html`, 2017.

[69] M. Ramilli, "Characterization of sipm: Temperature dependencies," in *2008 IEEE Nuclear Science Symposium Conference Record*, pp. 2467–2470, Oct 2008.

[70] J. Rosado and S. Hidalgo, "Characterization and modeling of crosstalk and afterpulsing in hamamatsu silicon photomultipliers," JINST **10** (2015) no.10, P10031.

[71] A. Para, "Afterpulsing in Silicon Photomultipliers: Impact on the Photodetectors Characterization," 2015.

[72] C. Xu, *Study of the Silicon Photomultipliers and Their Applications in Positron Emission Tomography.* PhD thesis, University of Hamburg, 2014.

[73] K. F. Johnson, "Extending the dynamic range of silicon photomultipliers without increasing pixel count," *Nuclear Instruments and Methods in Physics Research Section A: Accelerators, Spectrometers, Detectors and Associated Equipment*, vol. 621, no. 1, pp. 387 – 389, 2010.

[74] P. Barrow *et al.*, "Qualification Tests of the R11410-21 Photomultiplier Tubes for the XENON1T Detector," *JINST*, vol. 12, no. 01, p. P01024, 2017.

[75] Hamamatsu, "Tentative specifications for vuv3-s10943-3186 sipm." unpublished, internal Review Hamamatsu, 2014.

[76] F. Ritter, *Analysis of the GERDA Muon Veto - First Light.* PhD thesis, University of Tübingen, 2011.

[77] L. Baudis, Y. Biondi, C. Capelli, M. Galloway, S. Kazama, A. Kish, P. Pakarha, F. Piastra, and J. Wulf, "A Dual-phase Xenon TPC for Scintillation and Ionisation Yield Measurements in Liquid Xenon," 2017.

[78] F. Piastra, *Materials Radioassay for the XENON1T Dark Matter Experiment, and Development of a Time Projection Chamber for the Study of Low-energy Nuclear Recoils in Liquid Xenon.* PhD thesis, University of Zurich, 2017.

[79] H. Dujmovic, "Characterization and calibration of a liquid xenon time projection chamber," Master's thesis, University of Zurich, 2014.

[80] J. Haefner *et al.*, "Reflectance dependence of polytetrafluoroethylene on thickness for xenon scintillation light," *Nucl. Instrum. Meth.*, vol. A856, pp. 86–91, 2017.

[81] Y. Wei, Q. Lin, X. Xiao, and K. Ni, "Study of light detection and sensitivity for a ton-scale liquid xenon dark matter detector," *JINST*, vol. 8, p. T06002, 2013.